Optical Spectroscopy of Dusty Early-Type Galaxies using the Southern African Large Telescope

by

Ron W Savage

A thesis submitted in partial fulfilment for the requirements for the degree of MSc (by Research) at the University of Central Lancashire

January 2022

Declaration

I declare that while registered as a candidate for the research degree, I have not been a registered candidate or enrolled student for another award of the University or other academic or professional institution.

I declare that no material contained in the thesis has been used in any other submission for an academic award and is solely my own work.

No proof-reading service was used in the compilation of this thesis.

Signed:

Ron W Savage
January 2022.

Abstract

Our understanding of evolutionary differences between the general population of local early type galaxies (ETGs) and those with high dust content may be improved through a comparison of their stellar kinematics and populations. Sub-structures in the stellar kinematics and/or young stellar population components can indicate merger activity which may be the source of the dust. This thesis investigates the presence of these features in a sample of 16 nearby, dusty ETGs.

Long-slit optical spectra taken along the galaxies' major axis using the Robert Stobie Spectrograph on the Southern African Large Telescope, have been reduced to spatially binned 1D spectra. The pPXF package has been used to perform full spectral fitting of these 1D spectra with template spectra from the MILES library, using the penalised-pixel method. Spatial kinematic profiles are presented for 15 of the 16 target galaxies and spatial stellar population profiles for four of the 16. Mass weighted age and metallicity results have been obtained from the central region of 15 of the 16 and show that all contain intermediate to old stellar populations, with mass weighted average population ages greater than $\sim 4\times10^9$ yr. A plot of maximum rotational velocity/velocity dispersion versus ellipticity confirmed that these galaxies are mostly rotationally supported and a plot of stellar mass versus metallicity shows increasing metallicity with increasing mass. Ten of the dusty ETGs analysed gave similar kinematic and stellar populations results to the general population of nearby ETGs analysed in the SAURON and ATLAS^{3D} surveys. Five targets show possible sub-structures in their stellar kinematics, and four have a young stellar population component. While these young stellar population components point to a possible merger origin for some of the dust in those targets, there is no evidence that mergers contributed to the high dust content in all targets in this sample of dusty ETGs. Therefore, these results suggest that there may also be internal origins for the dust.

Table of Contents

Acknowledgments

I would like firstly to thank my supervisor Dr Anne Sansom for her excellent advice, support and guidance throughout this project. I would also like to thank my second supervisor Dr Mark Norris for his input and guidance.

I would also gratefully acknowledge my fellow postgraduate students David Glass and Tom Davison for their help and sound advice and Rudi Ganss who assisted in unravelling some of the mysteries of IRAF.

The observations reported in this thesis were obtained using the Southern African Large Telescope (SALT).

The following software packages were used for the data reduction and visualisation –

- Data reduction of fits images used the Image Reduction and Analysis Facility (IRAF) package (Tody, 1993).
- SAOImage DS9 (Joye and Mandel, 2003) was used for imaging and data visualisation.
- Correction for scattered light in the SALT 2D spectra followed the method of Katkov *et al.*, (2019), using their scatlight Python script.
- Full spectrum fitting for the analysis of stellar kinematics and populations made use of the pPXF package (Cappellari, 2017) and the MILES SSP library (Vazdekis *et al.*, 2010).

Supporting data were drawn from the GAMA Survey (Driver *et al.*, 2009; Baldry *et al.*, 2018).

List of Figures

List of Tables

Glossary of Terms, Abbreviations and Symbols

α-element – an element containing an integer number of helium-4 nuclei. The α-elements are C, O, Ne, Mg, Si, S, Ar, Ca and Ti

Å – Angstrom = 0.1 nm

ε – Ellipticity. The values for the target ETGs are taken from the GAMA Catalogue GALELLIP_r parameter

ΛCDM – the Lambda Cold Dark Matter cosmological model

χ^2 – the chi squared measure of goodness of fit

χ^2/DOF – the reduced chi squared statistic = chi squared divided by the degrees of freedom

BaSTI – Bag of Stellar Tracks and Isochrones. Available at: http://basti.oa-teramo.inaf.it/

CR – Cosmic Ray

CTIO – Cerro Toledo Inter-American Observatory

DOF – Degrees of Freedom

ETG – Early Type Galaxy

[Fe/H] – metallicity expressed as a ratio to Solar metallicity on a log scale

FITS – Flexible Image Transport System

FWHM – Full Width at Half Maximum of a spectral peak

GAMA – Galaxy and Mass Assembly survey

HLR – Half-Light Radius

IMF – Initial Mass Function

IRAF – Image Reduction and Analysis Facility software package

KPNO – Kitt Peak National Observatory

LOSVD – Line of Sight Velocity Dispersion

$M_\star$ – Stellar mass

$M_\odot$ – Solar mass

[M/H] – metallicity as defined by MILES ≡ [Fe/H] = $\log(Fe/H)_{galaxy} - \log(Fe/H)_\odot$ see http://research.iac.es/proyecto/miles/pages/ssp-models/name-convention.php

MEF – Multiple Extension Format for fits files

MILES – Medium resolution INT Library of Empirical Spectra

PC – personal computer

PI – principal investigator

PIPT – Principal Investigator Proposal Tool for SALT

pPXF – the penalised pixel fitting method and software (Cappellari, 2017)

PSF – Point Spread Function

R – Resolving power

R_e – half light radius

RSS – the Robert Stobie Spectrograph

SALT – the Southern African Large Telescope

SD – Standard Deviation

S/N – Signal to Noise ratio

SSP – Simple Stellar Population

V_{max} –maximum rotational velocity derived for each target from the spatial profile of velocities

V_{Rot} – rotational velocity

VPH – Volume Phase Holographic

Z – elements heavier than hydrogen and helium

1 INTRODUCTION

1.1 Overview and Aims

Early-type galaxies (ETGs) in general, with their low star formation rates and older stellar populations, are considered end points of galaxy evolution, but their evolutionary paths are not yet fully understood. The majority of ETGs have low dust content, but sub-mm observations, e.g. with the Herschel Space Observatory, have shown that some ETGs contain large amounts of dust (Agius *et al.*, 2013). This high dust content is a possible indicator of past events e.g. mergers, which have affected the galaxies' evolutionary path (Kokusho *et al.*, 2019). This project uses full spectral fitting of spatially binned, longslit optical spectra to obtain data on the stellar kinematic and population properties of a sample of the dustiest local ETGs. Differences between the dusty ETG sample and the overall ETG population can then be identified by comparison of these data with results from published surveys.

1.2 Scientific Background

1.2.1 Classification of ETGs

In 1936 Edwin Hubble developed the classic 'tuning fork' scheme (Hubble Sequence), for classification of galaxies based solely on their visual morphology, and in which Elliptical (E) and Lenticular (S0) galaxies are classified as ETGs. ETGs were thought typically to contain older stellar populations, to have little interstellar gas or dust and to have low rates of star formation. As shown in Figure 1-1, when plotted on a colour vs. mass diagram, ETGs tend towards redder (higher) *u-r* colours and late type galaxies (LTGs) tend towards bluer (lower) *u-r* colours. This leads to grouping of galaxies into a 'Red Sequence' of ETGs, a 'Blue Cloud' of star forming LTGs and a 'Green Valley', which is the intersection between the Blue Cloud and Red Sequence, as shown in Figure 1-2. The red, green, blue colour coding on the plot is for illustrative purposes only as the population has smoothly changing properties without sharp demarcations, as shown in Figure 1-1. The smooth transition is reinforced in the right panel of Figure 1-2 which shows –

1. overlap in the ETG and LTG populations, and,
2. the Green Valley being a sparsely populated zone relative to the Red Sequence and Blue Cloud.

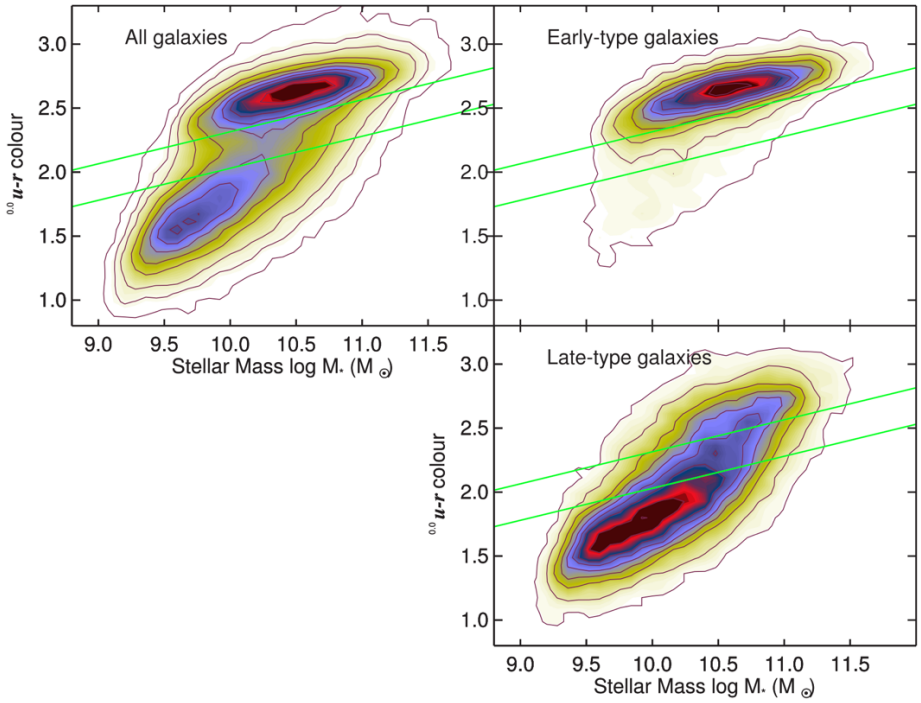

Figure 1-1: Plots of colour (*u-r*) vs. log galaxy mass (in solar mass ($M_\odot$) units) for a sample of Sloan Digital Sky Survey (SDSS) galaxies at $0.02 < z < 0.05$, from Schawinski *et al.* (2014). These illustrate the population overlap between galaxies morphologically classified as ETGs and LTGs. The contours represent number density and are scaled to the highest value in each panel. Green lines show boundaries of the Green Valley using the definition of Schawinski *et al.* (2014).

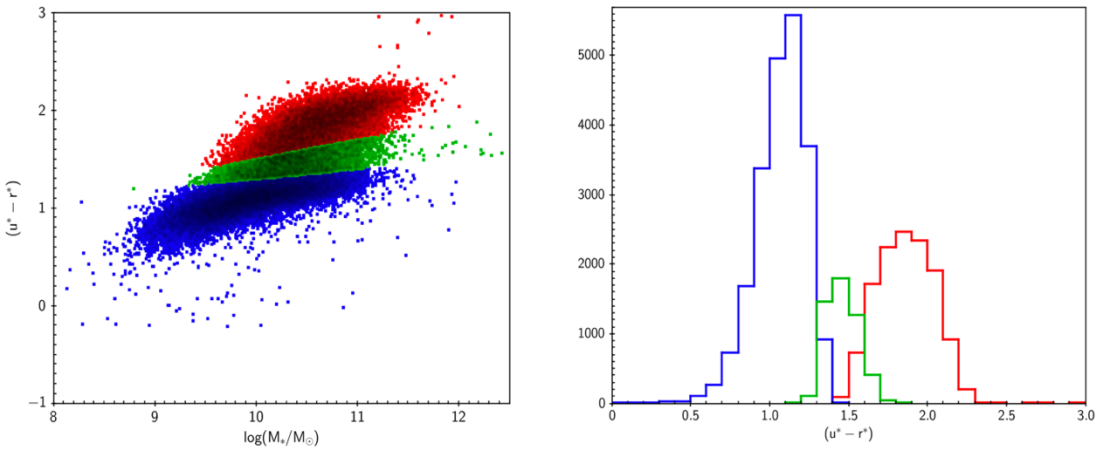

Figure 1-2: The left plot shows colour (*u-r*) vs log galaxy mass (relative to $M_\odot$), illustrating approximate locations of the Red Sequence, Blue Cloud and Green Valley, as defined by Phillipps et al. (2019). The right plot shows number of galaxies in this sample vs colour, with an overall bimodal shape and a lower number of galaxies in the Green Valley. Both plots from Phillipps et al. (2019).

Work during the first decade of this century using data from the SAURON survey, well summarised by Davies (2011), provided evidence to support an alternative classification of galaxies based on their angular momentum as well as their visual morphology. SAURON was followed up by the more detailed ATLAS^{3D} survey (Cappellari *et al.* 2011), which further developed the concept of fast and slow rotating ETGs, see Cappellari (2016) for a review, leading to an alternative classification scheme

to the Hubble Sequence. This new classification can be represented on a 'comb morphology diagram', see Figure 1-3, which categorises ETGs as either slow rotators or fast rotators along the horizontal axis based on their morphological and kinematic properties. Along the vertical axis galaxies are classified by the presence of spiral arms, including a category of 'anaemic' spirals (Aa - Ac) which sit morphologically between lenticulars and true spirals.

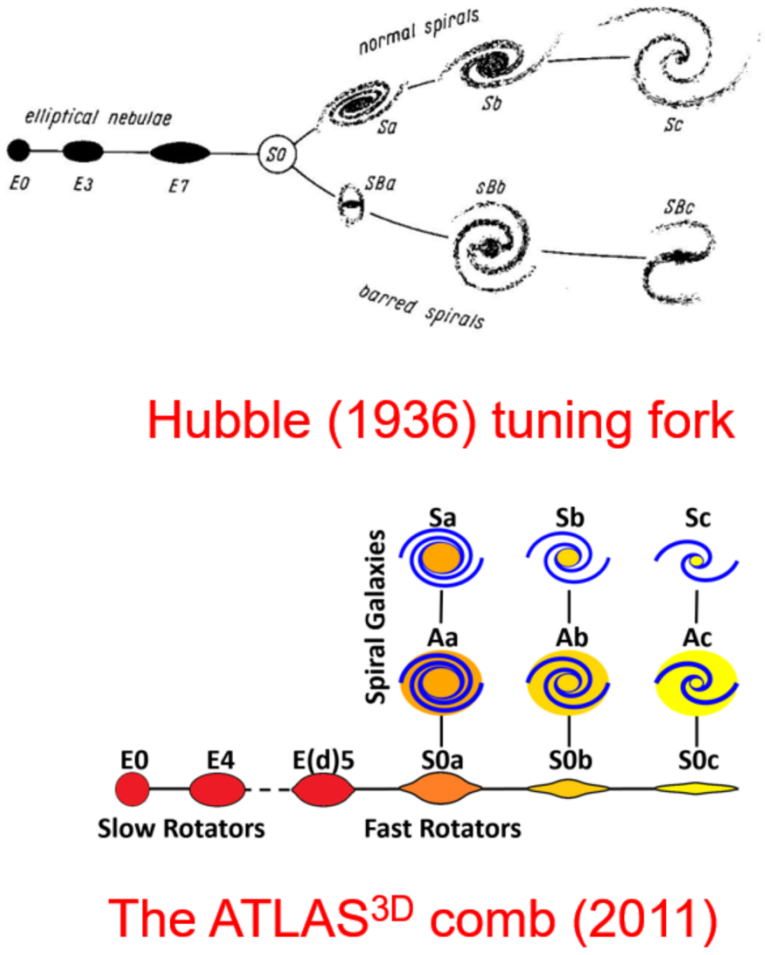

Figure 1-3: The upper panel illustrates the Hubble 'tuning fork'. The lower panel shows the comb morphology classification scheme with ETGs along the bottom and LTGs in rows above. ETGs are categorised into slow rotators (left side) and fast rotators (right side) based on their kinematics. Figure from the ATLAS^{3D} Survey at https://www-astro.physics.ox.ac.uk/atlas3d/

The following categorisation, from Cappellari (2016) and based on ATLAS^{3D} survey data, is adopted in this thesis –

- fast rotators form a sequence parallel to the spiral galaxies, typically have $M_\star$ between ~2×10^9 and ~2×10^{11} $M_\odot$, form the majority of the ETG population and have kinematics described by a combination of regular rotation and velocity dispersion. There is a significant overlap between the properties of fast rotator

ETGs and early-type morphology LTGs e.g. Sa type. Within this mass range, ETGs reach maximum stellar density at ~3×10^{10} $M_{\odot}$.

- slow rotators typically have $M_{\star}$ greater than ~2×10^{11} $M_{\odot}$, form about 15% of the overall population of ETGs, and display complex kinematics leading to four sub-groupings – 1. no rotation, 2. complex, 3. kinematically de-coupled cores and 4. counter rotating discs (Krajnović *et al.*, 2011, 2020).

1.2.2 Evolution of ETGs

The assembly and evolution of galaxies is described by the Lambda Cold Dark Matter (ΛCDM) cosmological model, where dark matter (DM) haloes formed in the early Universe around gravitational non-uniformities and became the seeds of galaxies when matter was attracted by gravity towards their centres. These zones of overdensity merged hierarchically and evolved to create the large-scale structure that we see in the Universe today, with galaxies present in dense clusters or in less dense groups and the field. Under this model of hierarchical merging the most massive galaxies, i.e. slow rotator ETGs, would sit at the centre of regions with highest density, i.e. the centre of clusters, and lower mass galaxies would sit in the outskirts of clusters, in groups and in the field. The Galaxy and Mass Assembly (GAMA) survey[1], from which the sample to be used in this project is taken, covers field and group environments (Driver *et al.*, 2011; Baldry *et al.*, 2018), and therefore, we can expect that the majority of ETGs in the sample will be lower mass i.e. fast rotators.

Current thinking suggests that with their low star formation rates and older, evolved stellar populations, ETGs are the end points of galaxy evolution, see for example Eales *et al.*, (2015) or Rizzo, Fraternali and Iorio, (2018). While not yet fully understood, the evolutionary path to ETGs outside cluster environments is thought to proceed through hierarchal merging of smaller, star forming, disc galaxies, resulting in ETG morphology and quenching of star formation (Angthopo, Ferreras and Silk, 2020). Green Valley ETGs have a bluer colour than Red Sequence ETGs, suggesting the presence of a young stellar population component. If galactic evolution proceeds from actively star forming to quenched, the presence of younger stars suggests that the Green Valley is a transition region of reducing star formation (Eales *et al.*, 2018). A review is presented by Salim (2014) and more recent work is covered in Phillipps *et al.* (2019), Rowlands *et al.* (2018) and Jian *et al.* (2020). Alternatively, some Green Valley galaxies may be quenched galaxies in which star formation is re-commencing through rejuvenation processes

[1] Available at: http://www.gama-survey.org/dr3/

(Lacerna *et al.*, 2016; Angthopo, Ferreras and Silk, 2019) e.g. by accretion of additional cold gas through minor mergers. The effects of the physical properties of ETGs and their environments on quenching of star formation, and hence on their transition into and through the Green Valley, remains an open question, however, the relative underpopulation in the Green Valley seen in Figure 1-1, implies that either –

1. a low fraction of star forming galaxies are quenching star formation, or
2. the process(es) which are quenching star formation happen relatively quickly in the timescale of ETG evolution (Phillipps *et al.*, 2019), or
3. the numbers are being underestimated because optical light is not a sensitive indicator of star formation rates e.g. Schawinski *et al.* (2014).

Current thinking suggests that the processes used to explain quenching of star formation can be divided into secular, referring to processes internal to the galaxy, and disruptive, referring to the impact of the external environment. Secular evolution is suggested by recent work on the development of structures in some lenticular type ETGs which would be contra-indicative to evolution through disruptive events (Kelvin *et al.*, 2018; Das, Pandey and Sarkar, 2021). However, the presence of younger, bluer stars in the stellar population of some ETGs (Kuntschner *et al.*, 2010; Werle *et al.*, 2020) might suggest a disruptive event or an accretion of material which has triggered a burst of star formation. Therefore, an understanding of the stellar kinematics and stellar population components of ETGs can provide information on events which influenced their evolution.

1.2.3 Interstellar Medium of ETGs

Traditionally ETG have been described as ‘red and dead’ due to their low levels of star formation and sparse interstellar medium (ISM), however, since the 1980s there have been hints that some ETGs contain higher levels of gas and dust in their ISM, see the Introduction of Kokusho *et al.* (2019) for a brief review of this early work. Over the last decade it has been confirmed that the ISM of many ETGs is relatively rich in cold gas and dust, see for example Agius *et al.* (2013), Davis *et al.* (2015), Sansom *et al.* (2019) and Yıldız *et al.* (2020), and ongoing low levels of star formation are not unusual (Kaviraj, 2008; Kokusho *et al.*, 2017). While ETGs with larger than expected quantities of dust were detected in the mid-2000s the origin of dust in ETGs in general, and especially in particularly dusty ETGs, is not fully understood leading to questions on the evolutionary path of these dusty ETGs vs. non-dusty ETGs.

Interstellar dust in ETGs is thought to be composed of small particles (<1μm) of inorganic carbon compounds, carbonates, silicates, oxygen and poly-aromatic hydrocarbons. It is thought to originate either from mechanisms internal to a galaxy such

as mass loss from AGB stars and supernova and/or through external mechanisms such as accretion, interactions and mergers, with the balance between internal and external sources an open question (Patil *et al.*, 2007; Smith *et al.*, 2012; Martini, Dicken and Storchi-Bergmann, 2013; Bassett *et al.*, 2017). Dust in the ISM of galaxies is also destroyed through mechanisms such as collision between dust particles and ions (sputtering) and disruption by shock fronts from supernova and therefore the quantity of dust present is determined by the relative rates of production and destruction, see Galliano, Galametz and Jones (2018) for a review. Recent measurements indicate that, without replenishment, dust declines exponentially in ETGs with a half-life of ~1.75 Gyr (Michałowski *et al.*, 2019).

1.3 Investigation of Dusty ETGs

This project investigates a sample of particularly dusty ETGs, making the sample different from the general ETG population, see Agius *et al.* (2015) for a description of the methodologies. The sample was chosen from the overall GAMA population based on data from an ongoing UCLan PhD. project (Glass, D. in preparation) using the following selection criteria –

- Redshift ~0.002 < z < ~0.06
- Brightness M_r < -17.4 mag
- Morphologically classified as early-type from GAMA and Galaxy-Zoo analysis
- Without an active galactic nucleus (AGN).

These criteria provided a sample of 1069 ETGs, with 201 having sub-mm emission associated with dust. From this population, 15 particularly dusty ETGs were selected for this project, shown in Figure 1-4, based on –

1. detection of dust at ⩾4σ in the 250μm band of the H-ATLAS survey (Glass D. in preparation). H-ATLAS[2] is a survey of galaxies at wavelengths of 100, 160, 250, 350, and 500μm using data from the Herschel Space Observatory, covering areas previously observed by the GAMA survey.
2. being candidates for molecular gas (CO), based on observations in the millimetre-wavelength using the IRAM 30m telescope (Glass D. in preparation). Dust mass was used as a proxy for molecular gas mass in observation planning.

[2] https://www.h-atlas.org/survey

The selected ETGs have log dust mass (M_{dust}) from 6.7 to 7.8 ($M_{\odot}$) and log $M_{\star}$ from 9.9 to 11.4 ($M_{\odot}$), see Table 2-2, giving M_{dust}:$M_{\star}$ ratios of 7×10^{-5} to 4×10^{-3}. They are particularly dusty when compared to a sample of 62 ETGs from Smith *et al.* (2012), who detected dust in 15 of the 62 with a mean M_{dust}:$M_{\star}$ ratio of 5×10^{-5}.

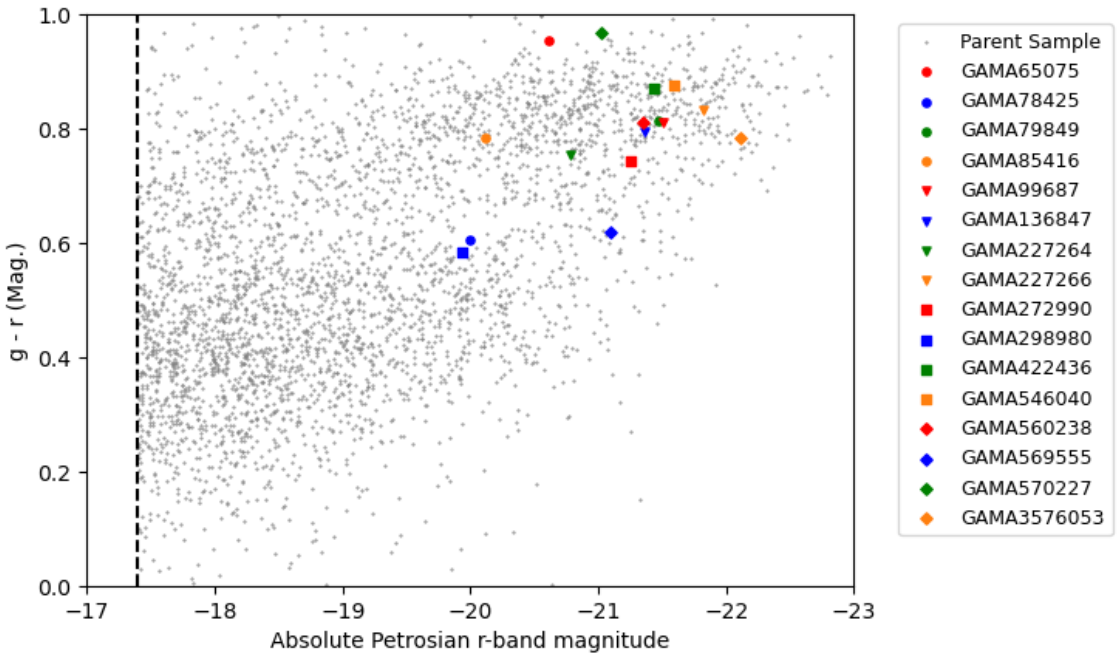

Figure 1-4: Location of the selected particularly dusty ETGs (plus GAMA65075 from Vaghmare *et al.* (2018)) on an optical *g-r* colour vs. magnitude diagram. Grey dots are the parent sample from the GAMA catalogue. The target galaxies are generally located around the Green Valley region.

Questions around secular vs. event driven evolution and the origin of high levels of dust can be informed by looking for irregularities, such as sub-structures, in the stellar kinematic and population profiles of the dusty ETGs, as these would suggest a recent disruptive event. Optical spectra of ETGs are dominated by light from evolved stars and have strong absorption features due to atoms and molecules in the cooler atmospheres of these stars. The spectra may also contain emission features, indicating recent star formation or the presence of an AGN. Information on stellar kinematics and populations of galaxies can be extracted from their optical spectra, for example –

- line of sight velocity can be estimated from Doppler redshift of spectral features
- line of sight stellar velocity dispersion (LOSVD) can be estimated from broadening of absorption features beyond instrumental broadening
- information on stellar populations such as age, metallicity and alpha element abundance can be inferred from the shape of the spectral continuum and absorption line strengths
- emission lines contain information on gas kinematics and gas metallicity.

Galaxies are comprised of populations of stars formed over time. These stellar populations can be modelled as combinations of individual simple stellar populations (SSPs). A SSP is a population of coeval stars with a known initial mass function (IMF) and evolution of a SSPs over time can be represented by a sequence of isochrones (Conroy, 2013). As a SSP evolves its spectrum changes as its component stars age and turn off the Main Sequence, see Figure 1-5. Unfortunately, determination of the age of a stellar population from optical spectra is made difficult by the age-metallicity degeneracy, where increasing age reddens the population through stars evolving off the Main Sequence on to the Red Giant Branch and increasing metallicity reddens the population through changing the opacity of stellar atmospheres. Determination of stellar population age is further complicated by reddening of the optical spectrum through dust extinction. Traditionally, the age-metallicity degeneracy was partially broken by using indices of specific spectral features that are more sensitive to either age or metallicity, e.g. the Lick/IDS system developed by Worthey *et al.* (1994). A more recent method is fitting a library of SSP template spectra to the optical spectrum of a target galaxy. This project will adopt the well documented method of full spectrum fitting using the Penalised Pixel Fitting Algorithm (pPXF) algorithm (Cappellari and Emsellem, 2004; Cappellari, 2017), to perform a chi-squared (χ^2) minimisation fitting of a library of SSP template spectra to the optical spectrum of the galaxy under investigation. Template SSP spectra will be drawn from the Medium resolution INT Library of Empirical Spectra (MILES)[3] library (Vazdekis *et al.*, 2010; Falcón-Barroso *et al.*, 2011). pPXF will be used to calculate recession velocity and LOSVD, to enable investigation of stellar kinematics, and stellar age and metallicity to enable investigation of stellar populations.

[3] Version 11 of the MILES library is available from: ftp://ftp.iac.es/MILES

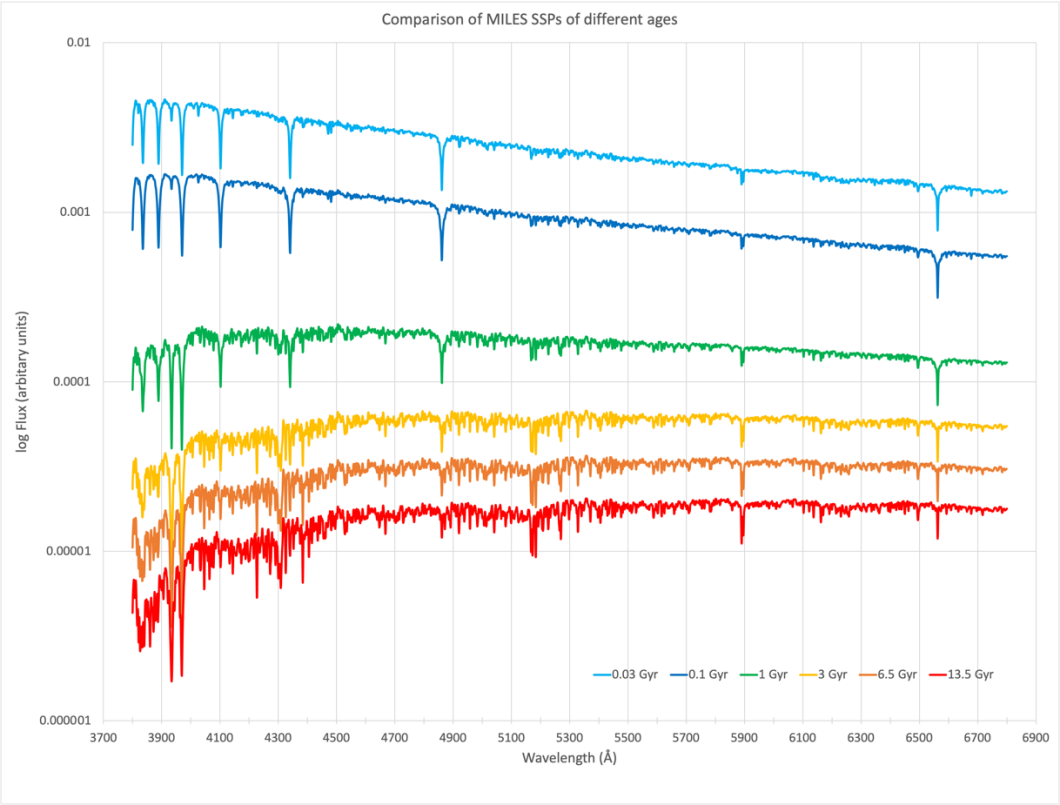

Figure 1-5: Plot of flux vs. wavelength for MILES SSPs of increasing age and fixed metallicity [Z/H] = +0.06, showing reduction in overall flux and change in continuum shape as age increases. The plot also illustrates the development of absorption features in intermediate to old age stellar populations.

1.4 Review of Previous and Related Work

ETGs have been widely studied but within the last approximately 15 years there have been major leaps in understanding of their kinematics and star formation histories, assisted in large part by the development and refinement of integral-field spectroscopy and associated data reduction and modelling techniques. The ability of integral-field spectroscopy to capture simultaneously multiple spectra covering the extent of a spatially extended target, has enabled production of spatially resolved maps of stellar kinematics and stellar population components for ETGs. The following two large-scale surveys, which provide a comprehensive baseline of the properties of ETGs, will be used as a control sample for this project –

- SAURON – an integral-field survey of a luminosity based sample of ~72 nearby ETGs aiming to improve understanding of ETG kinematics (Bacon *et al.*, 2001).
- ATLAS^{3D} survey – a volume limited, multi-wavelength, integral-field survey of 260 local ETGs, i.e. within a radius of 42 Mpc ($z < \sim 0.01$), with complementary modelling and simulation aimed to address open questions on their kinematics and star formation histories (Cappellari *et al.*, 2011). Figure 1-6 shows the ATLAS^{3D} parent sample on a *u-r* colour vs. magnitude diagram. The ATLAS^{3D}

survey data have been extensively researched, see footnote[4] for access to the list of ATLAS^{3D} papers, and published results.

Other relevant surveys are –

- SAMI – this was a general spectroscopic survey of galaxies to provide kinematic and structural information for a wide range of galaxy masses and environments (Croom *et al.*, 2012).
- MaNGA – this was a general integral-field spectroscopic survey of ~10000 nearby galaxies with mass >10^9 M_{Sun}, aimed at investigating their kinematics and composition Bundy *et al.* (2014).

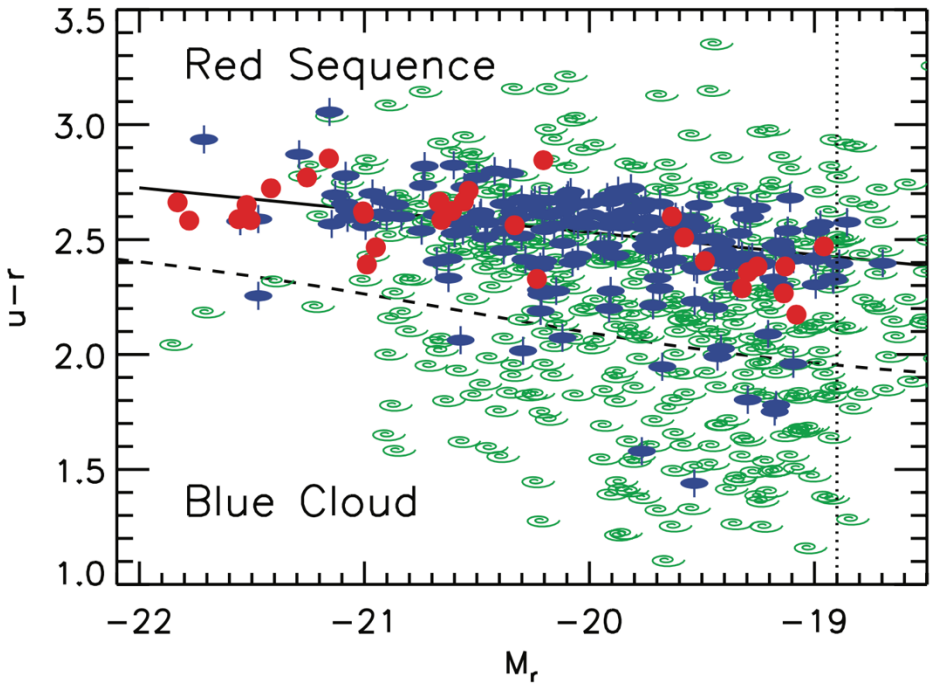

Figure 1-6: The ATLAS^{3D} parent sample on a *u-r* colour vs. magnitude diagram. Blue ellipses (fast rotator ETGs) and red circles (slow rotator ETGs) form the ATLAS^{3D} ETG sample and green spirals (LTGs) complete the ATLAS^{3D} parent sample. The dashed line represents a demarcation between red sequence and blue cloud. Figure from Cappellari, (2011).

This thesis, while stand alone, contributes to a study of the evolution of ETGs in optical, sub-mm and radio being undertaken at the Jeremiah Horrocks Institute at the University of Central Lancashire (UCLan).

1.5 Objectives and Thesis Structure

This project investigates the present-day stellar kinematic and stellar population properties of nearby dusty ETGs. Sub-structures in the stellar kinematics and/or young

[4]A list of ATLAS^{3D} papers is available at http://www-astro.physics.ox.ac.uk/atlas3d/publications.html

stellar population components will be used to infer if events in their evolutionary history, such as mergers, could have resulted in their high dust content. The project has the following objectives –

- to obtain and reduce major axis, long-slit, optical spectra for a sample of particularly dusty ETGs.
- to bin the 2D spectra based on S/N ratio to give 1D visible light spectra suitable for analysis of stellar kinematics and populations.
- to generate stellar kinematic profiles along the major axis, to compare these with the control sample and to identify any kinematic anomalies.
- to perform a preliminary analysis of stellar populations where S/N ratio allows

This Thesis is organised as follows. Section 1 introduces the subject, presents relevant scientific background, sets this work in context with published work and describes the sample of dusty ETGs. Section 2 describes the instrumentation and observations taken. Section 3 covers the methodology for data reduction of 2D longslit spectra from the Southern African Large Telescope (SALT), including use of IRAF and extraction of 1D spectra based on S/N ratio binning. Section 4 describes the use of pPXF to extract stellar kinematics results and Section 5 describes the use of pPXF to extract stellar populations results. Results are presented in Section 6 with discussion and conclusions presented in Section 7.

2 INSTRUMENTATION AND OBSERVATIONS

2.1 The Southern African Large Telescope

SALT is a 10m class telescope based in Sutherland, South Africa, with a design based on the Hobby-Ebberly telescope (*HET Overview*, 2017). It has a spherical primary mirror, made up of 91×1m hexagonal mirror segments, with a fixed angle of 37° to the zenith (SALT Ast Ops, 2020) and the ability to rotate in azimuth, see Figure 2-1. Instruments, or instrument heads, are mounted on a tracker, enabling the telescope to observe objects between $-75° < \delta < +10°$ declination. This telescope design creates a moving pupil with the target being tracked by movement of the instrument payload as shown in Figure 2-2. The two instruments used to gather data for this project are the Robert Stobie Spectrograph (RSS) and the SALTICAM camera (Burgh and Nordsieck, 2009; SALT Ast Ops, 2020).

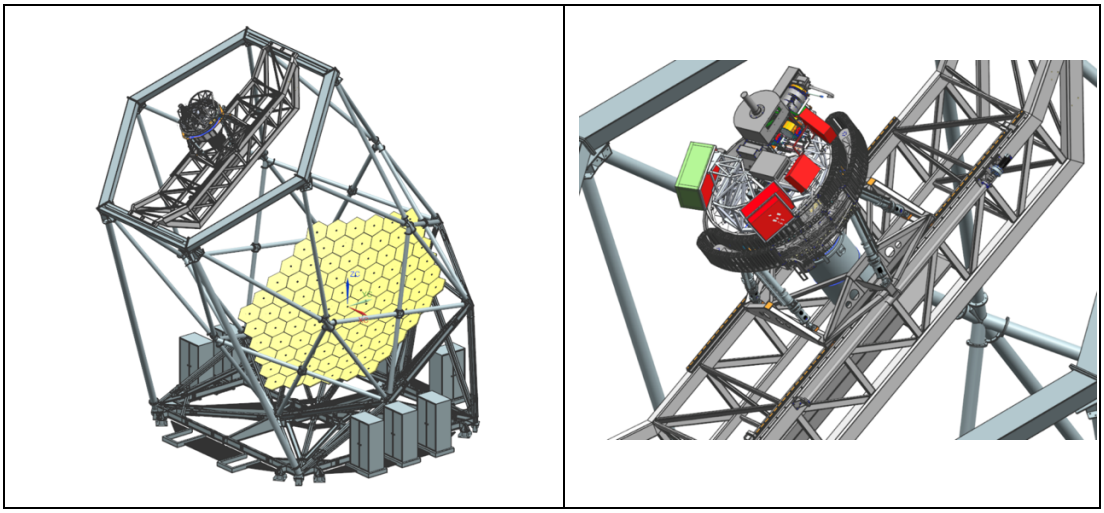

Figure 2-1: The left panel shows the SALT fixed zenith angle mirror and instrument payload location. The right panel shows a closer view of the instrument payload tracker. Image credit: SALT Ast Ops (2020).

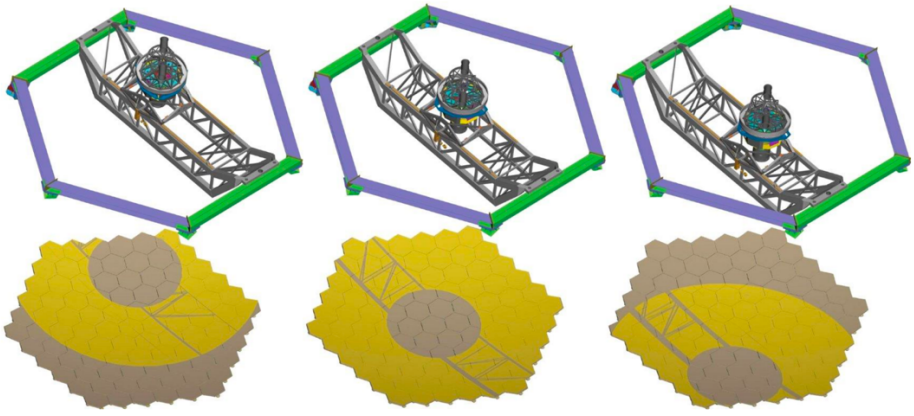

Figure 2-2: Illustration of the moving pupil of SALT. With the tracker centred (central image) SALT is equivalent to a 9m telescope, with the tracker at its travel limits (left and right images) SALT is equivalent to a 7m telescope. Image Credit: SALT Ast Ops (2020).

RSS is the SALT prime focus spectrograph, see Figure 2-3, and is the principal instrument for this project, where it is used for medium resolution spectroscopy in long slit mode. The detector is cryogenically cooled and has three 2048×4096 15 micron pixel CCDs covering an 8 arcmin field of view with a focal ratio of f4.2, giving a resolution of 0.1267 arcsec/pixel (unbinned), see Figure 2-4. The CCD chips are separated by 1.5mm which results in two gaps in the spectra.

SALTICAM is the prime focus imaging camera with two 2048x4096 15 micron CCDs giving a full field of view of 10 arcmin, a science field of 8 arcmin, and a resolution of 0.138 arcsec/pixel (unbinned). For this work SALTICAM is used to obtain images of the field and RSS slit, to facilitate location of the target galaxy in the RSS 2D spectra.

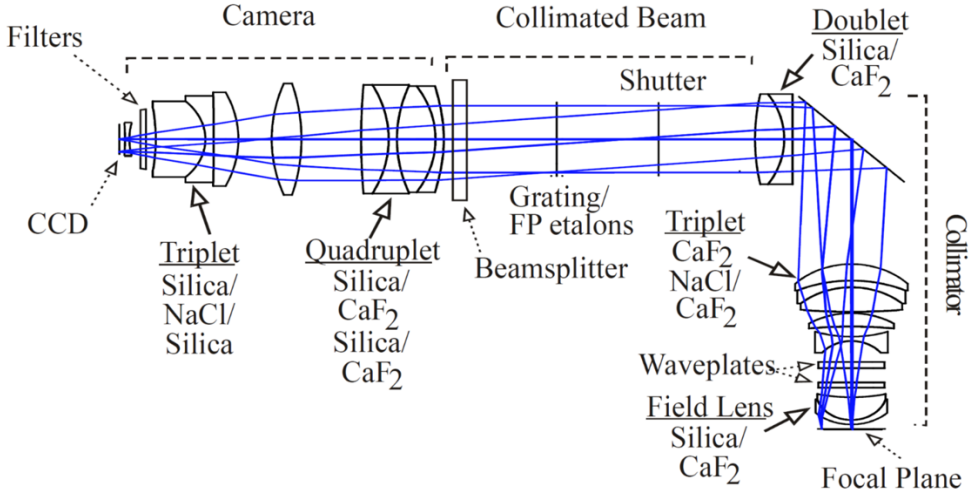

Figure 2-3: Position of key components, e.g. collimator, grating, camera and CCD detector, in the light path of the RSS. Image Credit: SALT Ast Ops (2020).

SALT is operated a queue mode by SALT astronomers on behalf of principal investigators (PIs) who have submitted proposals for observing time through the Principal Investigator Proposal Tool (PIPT)[5]. This is an on-line system with functionality for submitting information on a proposed observational programme, including targets, scientific justification, observational requirements and constraints and also the telescope/instrument configurations required for the observations. SALT astronomers schedule observations to meet the observational requirements and constraints, while making efficient use of telescope time.

[5] Available from: https://astronomers.salt.ac.za/software/pipt/

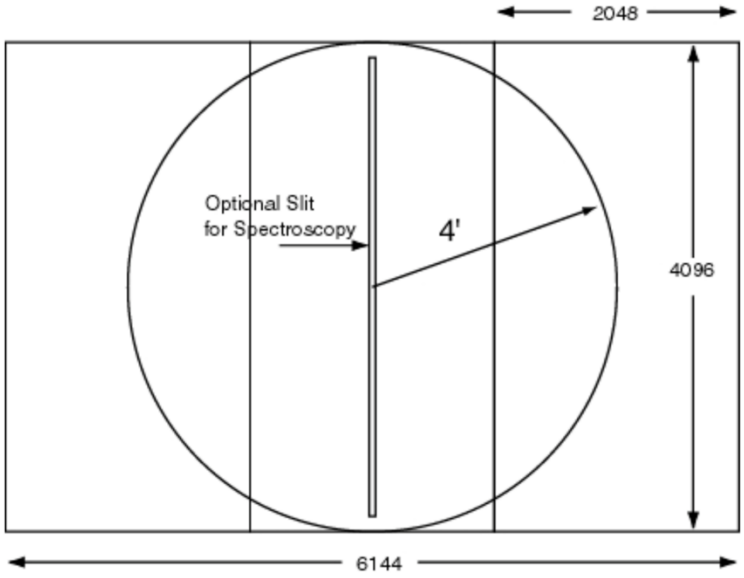

Figure 2-4: Detector layout for the RSS showing pixel dimensions of the CCD panels. Image Credit: SALT Ast Ops (2020).

2.2 Project Specific Instrument Parameters

Details of observational parameters and telescope/instrument set-up can be found in the SALT Proposal document (Sansom, A. E., 2019), and are summarised in Table 2-1. The instrument setup was determined using the RSS Simulator[6] (SALT, 2017), to provide spectra tailored for stellar kinematics and populations analysis e.g. with key spectral absorption features outside the detector chip gaps.

Spectral resolution, wavelength and resolving power are linked by –

$$R = \frac{\lambda}{\Delta\lambda} = \frac{c}{\Delta v} \qquad \text{Equation 2-1}$$

Where –

R = resolving power
$\Delta\lambda$ = spectral resolution = FWHM (Å)
λ = wavelength (Å)
v = velocity (km s^{-1})
c = speed of light = 299792 km s^{-1}

The RSS simulator calculated a mid-spectrum resolving power of 1399 at 5341Å, giving $\Delta\lambda$ = 3.8Å and instrument dispersion = $\frac{299792}{1399} = 214$ km s^{-1}, giving a FWHM instrument dispersion of $\frac{214}{2.355} = 90.9$ km s^{-1}.

2.3 Raw Data Processing by the SALT Pipeline

Raw data collected by SALT is automatically processed through the SALT Data Pipeline (Crawford, 2010) which performs an initial data reduction including gain,

[6] Available from: https://astronomers.salt.ac.za/software/#RSS. Version 4.4.1 was in use throughout this project.

crosstalk, bias correction and mosaicking the output from each CCD amplifier. The detectors are cryogenically cooled to ~158K, resulting in negligible dark current, therefore dark frames are not required (SALT Ast Ops, 2020). The SALT Data Pipeline packages relevant SALTICAM images, science spectra, flat and arc frames as Multi-Extension Format (MEF) Flexible Image Transport System (FITS) files into Product folders, sorted by night of observation. These are available for download by the PI, together with associated observatory and pipeline log files. FITS 'product' images require onward processing, also called data reduction, to enable extraction of useful scientific data (Kniazev, 2008; Hainline, 2015).

Table 2-1: Key SALT/RSS instrument parameters used for the observations.

Parameter	Value
Grating[1]	GR900 - 900 lines/mm Volume Phase Holographic transmission grating
Slit[1]	1 arcsec
Camera articulation angle[1]	28°
2nd order blocking filter[1]	PC03400
CCD well depth[2]	170,000 counts
Gain – Readout – ADU[2]	Faint – Slow → 1 electron/ADU
Dark current[2]	Negligible
Wavelength calibrator	Argon arc lamp
Image dimensions[2]	spectral = 3 × 2048 pixels, on-chip bin 2 = 3072 binned pixels spatial = 4096 pixels, on-chip bin 4 = 1024 binned pixels
Field (slit length)[2]	8 arcmin
Spatial sampling[2]	0.1267 arcsec/pixel (unbinned) 0.5068 arcsec/pixel (binned × 4)
Nominal spectral range[1]	3777 – 6850Å
Spectral sampling	0.48Å/pixel (unbinned) 0.96Å/pixel (binned × 2)
Nominal spectral resolution[3]	3.9Å
FWHM instrument dispersion[4]	90.9 km s^{-1}

Table 2-1 Sources –
1. SALT PIPT
2. SALT Proposal Call (SALT Ast Ops, 2020)
3. SALT RSS Simulator. The actual spectral resolution achieved was measured from arc images obtained during each observing session
4. from the nominal spectral resolution using Equation 2-1.

2.4 Targets and Observations

Information on physical parameters of the target ETGs for this study is presented in Table 2-2 and associated observational information is presented in Table 2-3. Spectra for an additional target, GAMA65075 (NGC5750), have been produced using data downloaded from the SALT Data Archive[7]. 4 × 900s observations for this target were

[7] Available at: https://ssda.saao.ac.za

taken with the instrument setup listed in Table 2-1 during May and June 2014 by Vaghmare *et al.* (2018).

Table 2-2: Summary of physical parameters for the target ETGs.

GAMA Galaxy [1]	Redshift Z_HELIO	Half-light Radius (R_e) GALRE_r arcsec	Half-light Radius (R_e) binned pixels	Ellipticity GALELLIP_r	Surface Brightness (V) mag/sq arcsec	Mass of stars logmstar log(Msun)	Mass of dust [2] log(Msun)	Visual Morphology HUBBLE_TYPE	Galactic Extinction EBV E(B-V) mag	Position Angle [3] deg
65075	0.0055	30.8	60.9	0.336	11.7	10.5	6.7	SB0-SBa	0.0445	69.8
78425	0.0531	2.1	4.2	0.367	20.4	10.0	7.6	S0 - Sa	0.0380	176.8
79849	0.0452	4.7	9.4	0.423	20.2	10.6	7.5	S0 - Sa	0.0494	4.7
85416	0.0194	5.9	11.6	0.665	19.8	10.2	7.1	E	0.0284	80.1
99687	0.0480	6.6	13.0	0.624	20.7	10.8	7.5	S0 - Sa	0.0258	124.6
136847	0.0277	8.1	16.0	0.298	19.9	10.7	7.0	S0 - Sa	0.0168	44.9
227264	0.0249	6.8	13.4	0.449	20.2	10.5	6.8	S0 - Sa	0.0370	83.0
227266	0.0249	9.6	19.0	0.112	20.5	11.0	6.8	E	0.0384	58.2
272990	0.0411	3.8	7.5	0.254	19.8	10.6	7.3	E	0.0291	2.9
298980	0.0271	3.8	7.6	0.322	20.4	9.9	7.0	E	0.0445	153.8
422436	0.0259	8.3	16.4	0.584	20.0	10.8	7.0	S0 - Sa	0.0392	141.7
546040	0.0266	11.8	23.3	0.086	21.0	10.9	7.0	S0 - Sa	0.0462	117.5
560238	0.0213	8.6	17.0	0.295	21.0	10.6	7.0	S0 - Sa	0.0280	24.7
569555	0.0569	2.7	5.3	0.392	19.9	10.4	7.8	S0 - Sa	0.0357	77.0
570227	0.0433	5.6	11.1	0.578	20.5	10.7	7.4	S0 - Sa	0.0525	7.3
3576053	0.0520	6.1	12.0	0.179	20.4	11.4	7.8	E	0.0306	8.0

Table 2-2 Notes –
[1] This line gives the parameter name from the GAMA catalogue.
[2] Quantified using data from H-ATLAS (Glass, D. in preparation).
[3] Measured from North through East as used in the SALT finder charts.

Table 2-3: Summary of key observational parameters for the galaxies.

Galaxy GAMA	**SALT Semester**	**Night Observed YYYYMMDD** [1]	**Exposure (s)** [2]	**Airmass** [2] [4]	**Sky Position Angle (o)** [2] [5]	**External Seeing (")** [3] [4]	**Comments**
65075	2014-1	20140511 20140613	900 x 2 900 x 2	1.21 1.19	70.6 70.6	Not recorded Not recorded	Observed by Vaghmare et al. (2018). Downloaded from the SALT Data Archive. No flats or arcs avaialble
78425	2019-1	20190624	800 x 3	1.25	176.8	1.6	No flats taken Significant cloud cover
79849	2019-1	20190426	600 x 4	1.22	4.7	0.87 - 1.39	No flats taken
85416	2020-1	20200510	648 x 3	1.20	80.1	Not recorded	RSS shutter failure. Sci and arc unaffected but no flats taken.
99687	2020-1	20200514 20200514	844 x 3 843 x 3	1.22 1.28	124.6 124.6	Not recorded	
136847	2019-2	20200124	500 x 4	1.27	44.9	Not recorded	
227264	2020-1	20200524	646 x 4	1.33	83.0	1.33 - 1.65	
227266	2020-1	20200622 20200724	801 x 3 802 x 3	1.27 1.30	58.2 58.2	1.8 1.5	RSS atmospheric dispersion corrector off-line on 20200622.
272990	2019-2	20200324	500 x 3	1.27	2.9	Not recorded	
298980	2019-1	20190426 20190426	698 x 3 698 x 3	1.22 1.30	153.8 153.8	0.87 1.17	No flats taken No flats taken
422436	2019-2	20191201	468 x 4	1.28	141.7	1.17 - 1.96	
546040	2020-2	20210222 20210324 20210410	924 x 2 924 x 2 924 x 2	1.18 1.34 1.26	117.5 117.5 117.5	Not recorded 1.1 1.1	
560238	2020-2	20210222	671 x 3	1.20	24.7	Not recorded	
569555	2019-1	20190511	501 x 4	1.19	77.0	1.4	No flats taken
570227	2019-1	20190512 20190522	586 x 3 586 x 3	1.19 1.20	7.3 7.3	1.1 1.5	No flats taken
3576053	2019-2	20191122 20191206 20200114	538 x 2 450 x 3 678 x 2	1.29 1.29 1.27	8.0 8.0 8.0	1.4 1.0 1.8	

Table 2-3 Notes –
[1] date format used throughout this thesis is YYYYMMDD, to match the format used in SALT product files
[2] from the FITS image headers

[3] from the SALT Astronomer's Log
[4] average value for images in the observing block
[5] sky position angle - measured east from the positive y axis

2.5 Data Consistency Checks

An inventory check was performed between the telescope log, SALT Pipeline Log, files provided in the SALT Product directories and the expected inventory of files. Each SALT Product directory should contain –

- flat frames taken in the same observing block as the science images
- science frames for each target
- two Argon arc images, one taken before, and one taken after each group of science images
- one image of the field and one image of the slit taken using SALTICAM.

The inventory of SALT Product folders showed the expected complement of image, arc, flat and science files for all observed targets, with the following exceptions –

- SALT Product folders for 2019 Semester 1 showed the expected complement of image, arc and science files for all observed targets, however none contained the expected flat files. Flat files were not specifically requested via the PIPT, based on previous experience of SALT astronomers delivering a single master flat file for each binning level using exposures taken at the end of a night's observing run. Discussions between Sansom and SALT astronomer A. Kniazev (personal communication) indicated that it was no longer practice for SALT astronomers to produce a single master flat file and that the current recommendation was for flat files to be taken at the time of the observations as part of the PI's charged telescope time (SALT Science Wiki, 2014). This recommendation was adopted for 2019 Semester 2 and later observations. The reduction process for Semester 1 files was adapted by creating a single flat file from flat files taken for the 2019 Semester 2 targets. This was used to correct all 2019 Semester 1 science images, as described in Section 3.1.
- for 2020 Semester 1, flat files were taken as requested except for GAMA85416 on 20200510, where a failure of the RSS shutter stopped the observing run before flats could be taken. A flat from observations of GAMA99687 on 20200514 was used for correction of the GAMA85416 observations. The GAMA85416 arc and science files were unaffected by the RSS shutter failure.
- due to a mechanical failure the RSS atmospheric dispersion corrector was off-line for observations of GAMA227266 on 20200622.

- for GAMA65075 the inventory of images downloaded from the SALT Data Archive showed the expected complement of image, and science files, however the SALT Data Archive does not provide arc or flat files.

Following the above inventory check SALTICAM images were opened in DS9 –

- to confirm visually that the correct target galaxy had been selected by comparing the position of the target on the field image with a finder chart. Charts were downloaded from the SALT PIPT and if needed additional charts were downloaded from the SDSS DR7 Finding Chart Tool[8] and scaled to the 8 arcmin field of SALTICAM.
- to confirm visually the spatial position of the target in the slit. This to allow later selection of the correct trace from the RSS longslit spectrum.
- to confirm dimensionality of the images and orientation of the slit along the target galaxy long axis using position angle information from the image headers.

Inspection of the SALTICAM images showed that all targets were correctly positioned and aligned. An example of SALTICAM field and slit images are shown in Figure 2-5.

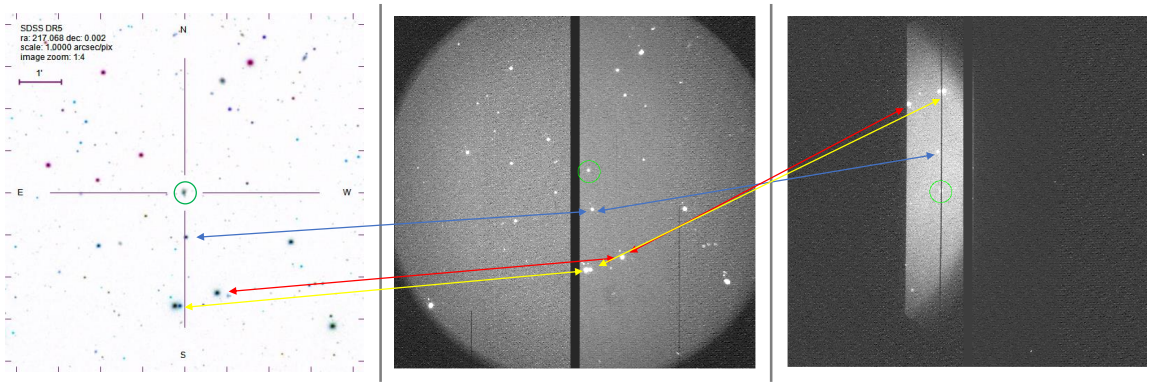

Figure 2-5: The left panel shows a finder chart centred on the coordinates of galaxy GAMA78425. The centre panel shows the equivalent SALTICAM field image, and the right panel shows the SALTICAM image of the location of the target galaxy in the slit. The target galaxy is marked with a green circle. Equivalent stars in the three panels are marked with coloured arrows confirming correct target selection and positioning in the slit.

2.6 Preparation for Data Reduction

MEF FITS files for an observing block were converted to single header FITS format, more convenient for processing with IRAF, using IRAF command *imcopy[SCI,1,inherit]*, to copy the files to a specific observing block folder. Initial visual examination showed that the arc and science images contained overscan areas on the y-axis between pixels 1 - 40 and 1000 - 1024, and columns on the x-axis with no useful data between pixels

[8] Available at: http://cas.sdss.org/dr7/en/tools/chart/chart.asp

3168 - 3172. Science, arc and flat images were trimmed using *imcopy[1:3160,40:990]* to ensure that the overscan areas would not create edge effects during data reduction. These preparation steps delivered a set of single-header, trimmed FITS files for each observation block suitable for further data reduction. DS9 was used to perform an examination of the science files to confirm that there were no visual abnormalities in the images. This revealed the expected large numbers of cosmic ray artefacts and a column of bad pixels in the left-hand CCD of the RSS detector at x-pixel 462. An example science file is shown in Figure 2-6.

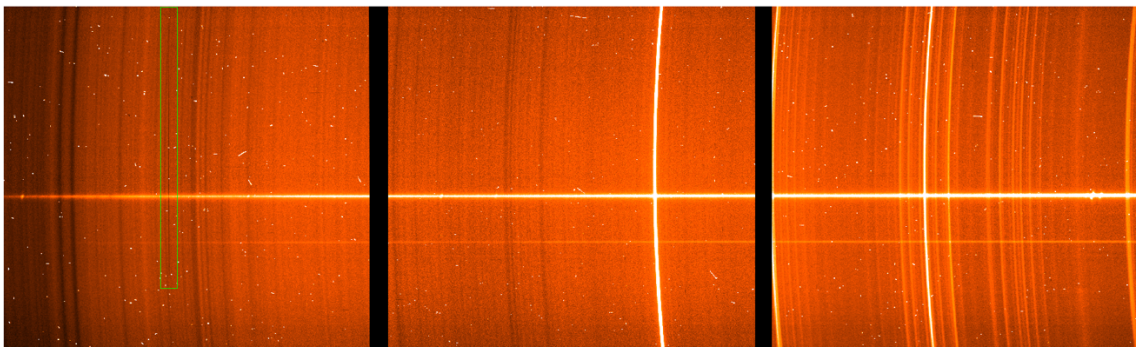

Figure 2-6: Example of a trimmed raw science file for GAMA298980 showing the target trace as a horizontal line across the image centre. A trace from a fainter object in the slit can be seen below the target trace. Black vertical bars are CCD chip gaps. Sky emission lines show as vertical curved lines and sky background as the overall orange colouration. Cosmic ray artefacts show as white points. The left CCD panel has a bad pixel column at x pixel 462, visible as a black column and marked with a green box.

3 REDUCTION OF THE 2D LONGSLIT SPECTRA

The objective of data reduction is to extract high signal to noise (S/N) ratio 1D spectra for apertures of the target galaxies from the science files. The principal tools used for data reduction were the Image Reduction and Analysis Facility (IRAF) package (Tody, 1986) for FITS file manipulation and DS9 (Joye and Mandel, 2003) for image visualisation. Wherever possible, to ensure consistency in image processing, lists of IRAF commands and their parameters were executed as scripts at the IRAF command prompt (Anderson and Seaman, 1989). The IRAF parameters used for each task were determined by experimentation based on parameters suitable for SALT RSS longslit data in the SALT Data Reduction Guidelines[9]. A copy of the IRAF scripts, lists of tasks and text files listing the parameters used is held on the UCLan server in sub-folders of san/galactic/rsavage. Figure 3-1 shows a summary of the sequence of steps in data reduction. Data reduction initially takes place in folders used to group all files from an observing block, with observation date used as the folder name e.g. 20190512. To facilitate tracking of images through the data reduction steps a file naming structure was developed as shown in Appendix A.

3.1 Flat Field Correction

The purpose of flat fielding is to correct for variations in response of individual pixels across the detector. This is achieved by dividing the science images by a normalised flat image ('illumination flat') from which the illumination pattern of the light source used to create the flat image has been removed, as illustrated in Figure 3-2. An illumination flat was created for each observing block containing the expected five flat files. Individual flat images were combined using IRAF task *imcombine* with combine=median and scale=mean. To maintain pixel-to-pixel mapping the combined flat file was trimmed to the same dimensions as the science files using IRAF task *imcopy*. This combined, trimmed flat was then converted to an illumination flat using IRAF task *response*, to fit a polynomial function to the illumination pattern in the dispersion and spatial directions and to divide the image by that function to remove the illumination pattern of the light source. Polynomials of order 9 in the dispersion direction and order 7 in the spatial direction were used. An example is presented in Figure 3-3.

[9] Available at - https://sciencewiki.salt.ac.za/index.php/Data_Reduction_Guidelines and https://sciencewiki.salt.ac.za/index.php/Long_Slit_Reduction_Recipe

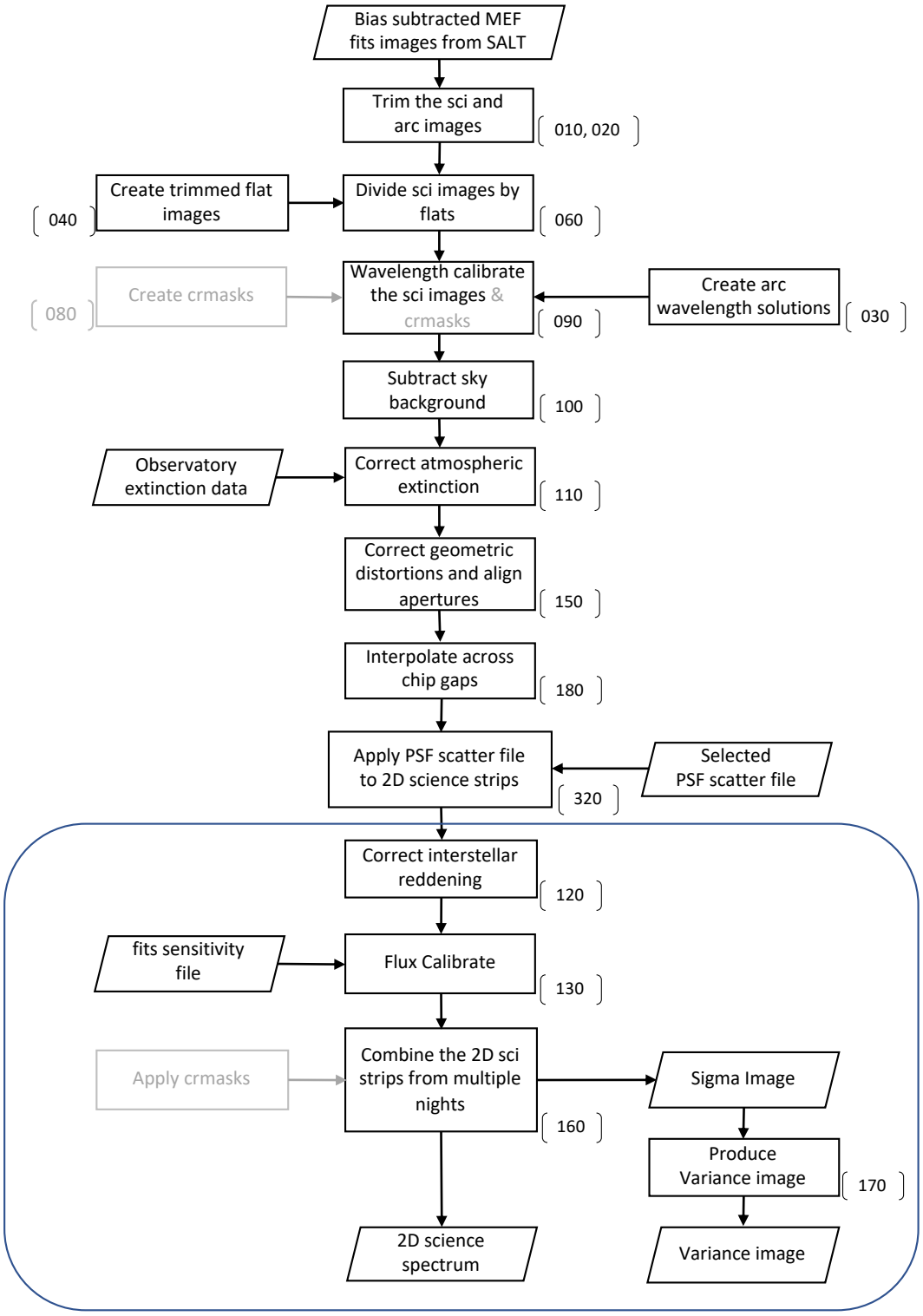

Figure 3-1: Summary of steps for reduction of SALT Product images to 2D spectra and variance files, ready for binning and 1D spectra extraction. References to crmasks are shown in grey for completeness as these were developed but not used in the final image processing sequence. Numbers in brackets identify script(s) used at that step. The blue rectangle surrounds steps that were performed on both science spectra and scattered light corrected science spectra. The file naming convention is presented in Appendix A.

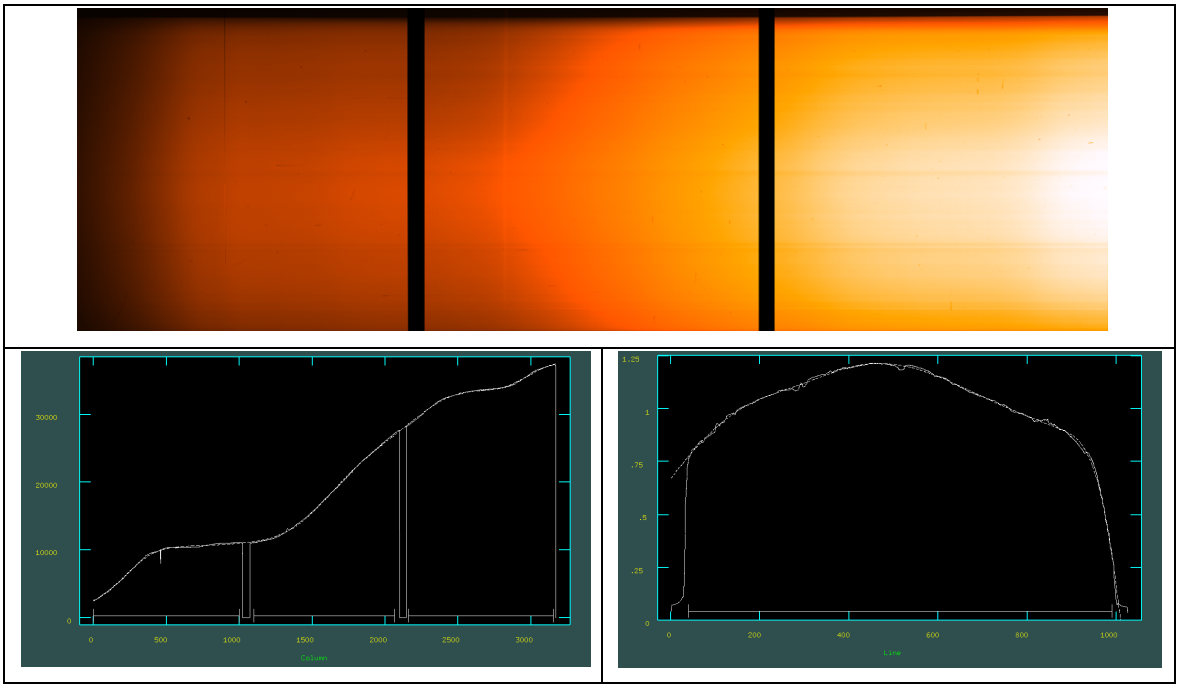

Figure 3-2: The top panel is an example of a typical untrimmed, combined flat file, showing variations in illumination pattern along both spectral and spatial axes. The lower left panel is a cut in the spectral direction and the lower right panel a cut in the spectral direction. The observed illumination function is shown as a solid white line and the polynomial fitted by IRAF *response* as a dashed white line. Lower panels illustrate non-uniform illumination in both the spectral and spatial directions, and the presence of overscan regions.

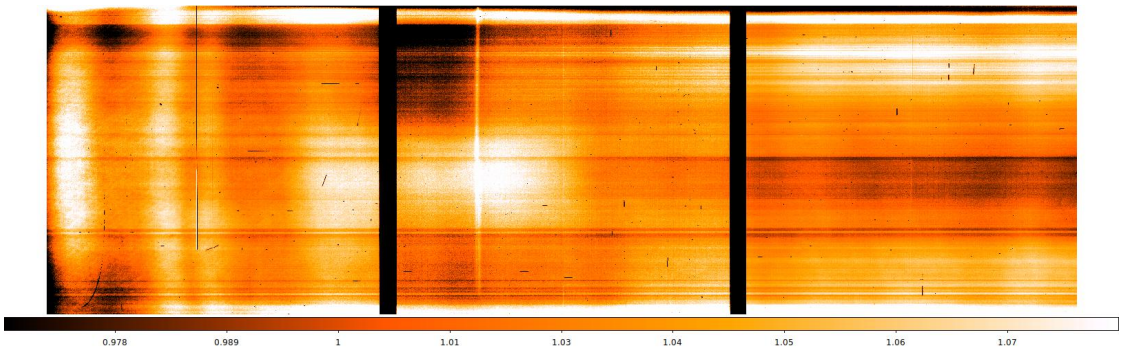

Figure 3-3: Example illumination flat with pixel scale bar. This high contrast view reveals uneven pixel responses across the three CCD chips and bad pixel areas.

All science images in an observing block were then divided by the illumination flat using IRAF task *imarith* to give flat corrected science files. Given the unavailability of flat images for 2019 Semester 1 and stability of the pixel-to-pixel variations (SALT Ast Ops, 2020), a 'master' illumination flat was developed from 15 flat images from the SALT Product folders for nights 20191122, 20191201 and 20191206. All science images from 2019 Semester 1 were divided by this 'master' illumination flat to give flat corrected science files. As the SALT Data Archive does not provide flat files, this 'master' illumination flat was also used in reduction of GAMA65075 science images. The illumination flat from GAMA99687 observations on 20200514 was used to correct GAMA85416 science files observed on 20200510.

3.2 Developing the Arc File Wavelength Solutions

To fit a wavelength calibration from arc images to science images a wavelength must be assigned to each pixel in the arc images, in a three-step process using IRAF tasks *identify*, *reidentify* and *fitcoords*. Parameters initially used were the defaults specified by Hainline (2015), with these being modified only if required to improve the fit to the arc file data.

IRAF *identify* enables manual identification of peaks of known wavelength in the Argon arc file, using a wavelength atlas downloaded from SALT[10], followed by a one-dimensional interpolation of wavelengths between known peaks. Residuals (RMS) from this fitting were then reduced by manually removing outlying points. The one-dimensional wavelength solution was then applied across the y-axis by using IRAF *reidentify*, to give a two-dimensional mapping of wavelengths across the arc image. This was followed by IRAF *fitcoords* which fits the mapping from *reidentify* to the arc image and enables manual removal of any outlying points. Each arc file was individually calibrated using this process.

3.2.1 Optimisation of the Fitting

An example of the use of *identify* is shown in Figure 3-4, with manually removed outliers shown as × and fitted points shown as +. Two outlying line groupings, seen in Figure 3-4 (top panel), were present in all arc images. Firstly, a line of high residual points at x pixel ~2100 and secondly a grouping of higher-than-normal residual points at x pixel ~1075. As shown in Figure 3-4 (middle panel), some arc lines intersect the chip gaps at these pixel values creating fitting artefacts. The artefacts were removed during fitting of all arc files using *identify*, as illustrated in Figure 3-4 (bottom panel).

Application of *reidentify* and *fitcoords* generated 2D wavelength fitted solutions. Testing of the polynomial fitting parameters for *fitcoords* showed that using higher orders did not give a significant improvement in fitting. As recommended by Hainline (2015) an order 5 polynomial was used for fitting the dispersion direction and an order 3 polynomial for the spatial direction. As shown in Table 3-1, RMS values from *fitcoords* were in the range 0.15 to 0.26Å with a mean of 0.18Å, significantly less than the nominal spectral resolution of 3.9Å, indicating that these wavelength solutions are suitable for calibration of the science spectra.

[10] Available at: https://astronomers.salt.ac.za/data/salt-longslit-line-atlas/

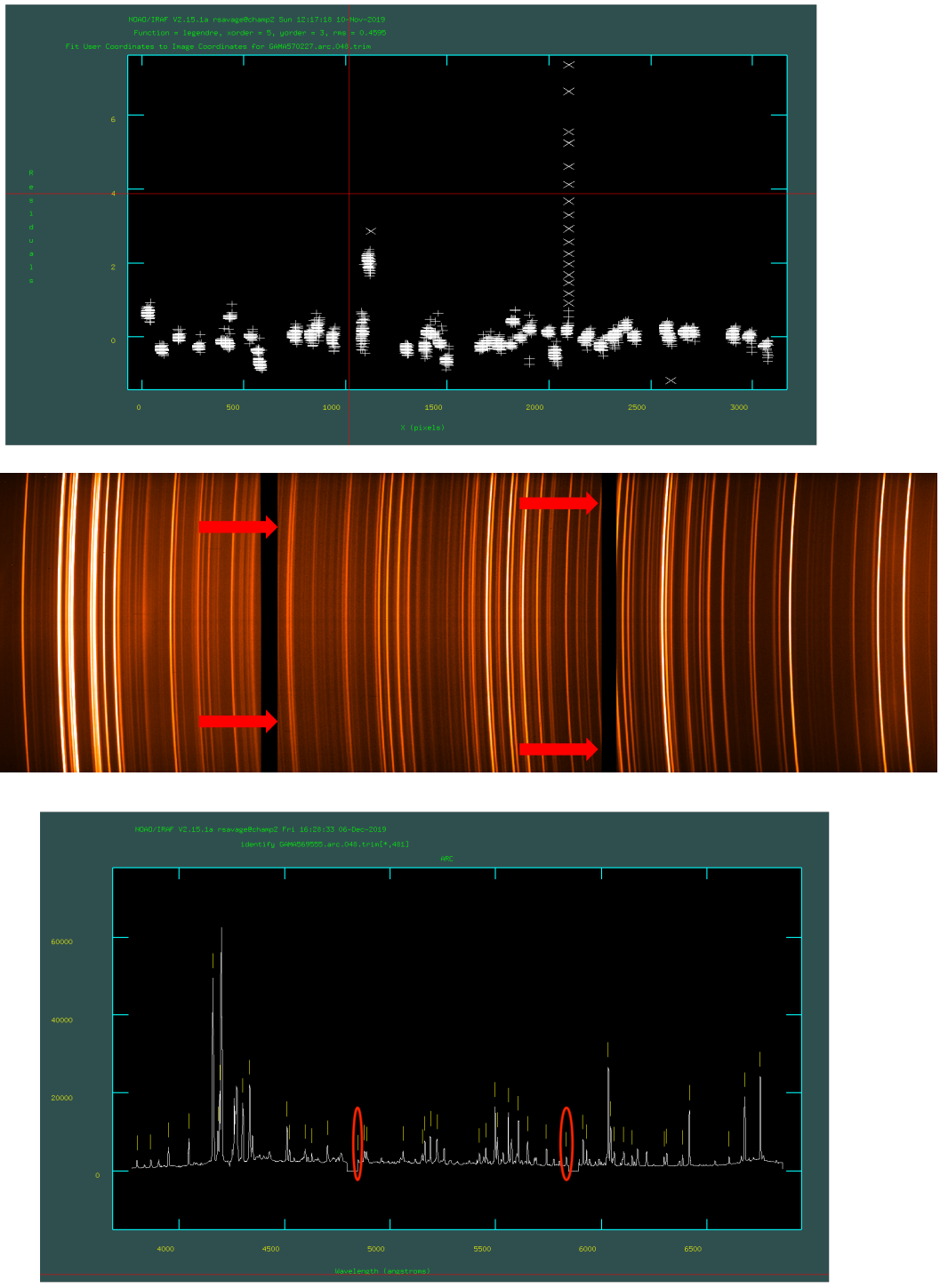

Figure 3-4: Fitting of an example arc file. The top panel shows residuals from fitting arc lines, including the two abnormal sets of points. The middle panel shows an example arc image with positions of the poorly fitting lines at chip gaps marked with red arrows. The lower panel shows alignment of arc file wavelengths with the SALT wavelength atlas, with lines to be removed highlighted in red.

Table 3-1: Diagnostic information from wavelength calibration of arc files. Column 4 lists RMS values from *fitcoords* for all arc files. Columns 5 to 9 list results from comparison of sky-lines at 5577.34Å, 6330.3Å and 6363.78Å with the wavelength of equivalent lines from wavelength calibrated science files.

DATE yyyymmdd	TARGET	ARC	Fitcoords RMS (Å)	Measured Å for 5577.34Å line	Delta from 5577.34Å	Measured Å for 6300.3Å line	Delta from 6300.3Å	Measured Å for 6363.78Å line	Delta from 6363.78Å
20190426	GAMA79849	075	0.17	5577.21	-0.13	6300.19	-0.11	6363.70	-0.08
		080	0.19	5578.00	0.66	6300.97	0.67	6364.46	0.68
	GAMA298980	084	0.18	5577.14	-0.20	6300.16	-0.14	6363.51	-0.27
		088	0.19	5577.82	0.48	6300.88	0.58	6364.25	0.47
		089	0.17	5577.24	-0.10	6300.27	-0.03	6363.73	-0.05
		093	0.17	5578.14	0.80	6301.25	0.95	6364.56	0.78
20190511	GAMA569555	048	0.17	5576.95	-0.39	6299.92	-0.38	6363.43	-0.35
		053	0.18	5576.86	-0.48	6299.79	-0.51	6363.31	-0.47
20190512	GAMA570227	049	0.18	5577.24	-0.10	6300.21	-0.09	6363.95	0.17
		053	0.17	5577.71	0.37	6300.73	0.43	6364.37	0.59
20190522	GAMA570227	048	0.16	5577.18	-0.16	6300.24	-0.06	6363.54	-0.24
		052	0.17	5577.73	0.39	6300.88	0.58	6364.16	0.38
20190624	GAMA78425	062	0.17	5577.16	-0.18	6300.14	-0.16	6363.52	-0.26
		066	0.19	5577.85	0.51	6300.93	0.63	6364.27	0.49
20191122	GAMA3576053	064	0.17	5577.13	-0.21	6300.02	-0.28	6363.46	-0.32
		067	0.15	5577.60	0.26	6300.45	0.15	6363.91	0.13
20191201	GAMA422436	058	0.15	5577.29	-0.05	6300.33	0.03	6363.92	0.14
		063	0.17	5577.46	0.12	6300.47	0.17	6364.09	0.31
20191206	GAMA3576053	059	0.17	5577.18	-0.16	6300.18	-0.12	6363.71	-0.07
		063	0.15	5577.57	0.23	6300.56	0.26	6364.03	0.25
20200114	GAMA3576053	066	0.16	5577.17	-0.17	6300.08	-0.22	6363.60	-0.18
		069	0.16	5577.48	0.14	6300.35	0.05	6363.90	0.12
20200124	GAMA136847	056	0.16	5576.99	-0.35	6300.08	-0.22	6363.56	-0.22
		061	0.19	5577.36	0.02	6300.50	0.20	6363.95	0.17
20200324	GAMA272990	093	0.14	5577.16	-0.18	6300.27	-0.03	6364.10	0.32
		097	0.16	5577.86	0.52	6300.97	0.67	6364.65	0.87
20200510	GAMA85416	054	0.18	5576.48	-0.86	6299.93	-0.37	6363.25	-0.53
		058	0.19	5577.03	-0.31	6300.07	-0.23	6363.41	-0.37
20200514	GAMA99687	041	0.15	5577.17	-0.17	6300.32	0.02	6363.58	-0.20
		045	0.16	5577.79	0.45	6301.05	0.75	6364.39	0.61
		065	0.15	5577.34	0.00	6300.39	0.09	6363.88	0.10
		069	0.18	5578.27	0.93	6301.35	1.05	6364.84	1.06
20200524	GAMA227264	088	0.18	5577.90	0.56	6300.34	0.04	6363.84	0.06
		093	0.17	5578.03	0.69	6300.55	0.25	6364.02	0.24
20200622	GAMA227266	078	0.19	5577.05	-0.29	6299.95	-0.35	6363.36	-0.42
		082	0.26	5577.46	0.12	6300.31	0.01	6363.67	-0.11
20200724	GAMA227266	102	0.19	5577.15	-0.19	6300.06	-0.24	6363.49	-0.29
		106	0.20	5577.21	-0.13	6300.19	-0.11	6363.62	-0.16
20210222	GAMA546040	248	0.21	5576.89	-0.45	6299.89	-0.41	6363.20	-0.58
		251	0.19	5577.49	0.15	6300.47	0.17	6363.58	-0.20
20210222	GAMA560238	084	0.16	5576.73	-0.61	6299.79	-0.51	6362.99	-0.79
		088	0.19	5577.58	0.24	6300.51	0.21	6363.82	0.04
20210324	GAMA546040	079	0.16	5577.29	-0.05	6300.42	0.12	6363.87	0.09
		082	0.19	5577.93	0.59	6300.93	0.63	6364.41	0.63
20210410	GAMA546040	130	0.19	5577.20	-0.14	6300.53	0.23	6363.45	-0.33
		133	0.20	5577.88	0.54	6300.98	0.68	6363.95	0.17
		MEAN	**0.18**						

3.2.2 Accuracy of the Wavelength Solution

Each observing block contains two arc files per target, one taken before and one after the science observations. As spectral line positions can shift slightly during an observing run due to small variations in the light path, each science image was individually allocated one of the arc file solutions. A comparison was performed between the two arc images by using *transform* to apply the wavelength solution from each to a science image selected from within the same observing block. Positions of three prominent [OI] sky lines at 5577.34, 6300.30 and 6363.78Å in the two resulting wavelength calibrated science images were then determined using the gaussian fitting function in *splot,* to determine the peak wavelengths of the lines, as illustrated in Figure 3-5.

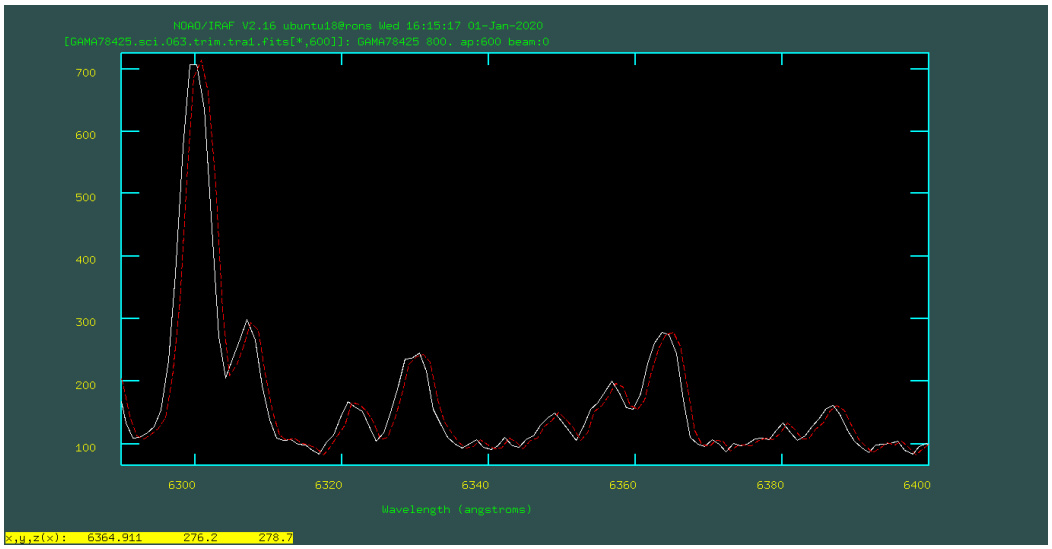

Figure 3-5: Illustration of the use of *splot* to overplot spectra, showing a counts vs wavelength plot of a wavelength calibrated spectrum from GAMA78425. The white trace shows calibration using the first arc solution and the overplotted red trace shows calibration using the second arc solution. The difference in wavelength calibration is ~0.7Å.

The fitted wavelengths were compared with published wavelengths of sky-lines (Osterbrock *et al.*, 1996) to give an estimate of accuracy of the wavelength solution. Results from this comparison are given in Table 3-1 and show that differences between fitted and published wavelengths of the sky lines are typically ~0.3Å, confirming suitability of the wavelength solutions for calibrating the science files. Results also show that normally the first arc underestimates and the second arc overestimates wavelength, therefore each science image was wavelength calibrated using the arc taken closest to the time of the science image observation.

3.3 Creation of Cosmic Ray/Bad Pixel Masks

Raw science images contain cosmic ray (CR) artefacts which must be removed before useful science data can be extracted. While CR artefacts can normally be removed by a median combine of at least three individual images, it is good practice to produce a CR/bad pixel mask for each science image. Masks were generated using IRAF *xzap* (Farage and Pimbblet, 2005) from the *xdimsum* package. This task produces a CR mask with naming convention crmask_*.fits.pl and a CR cleaned science file. The parameters for *xzap* were tested to confirm that flux from the spectrum of the target galaxy was not included in the crmask file. Parameters specified by Hainline (2015) successfully created crmask files which included CR artefacts but not the target spectrum. Images of crmasks suitable for visualisation using DS9 were created using IRAF *imcopy* crmask*.pl maskimage*[type=mask]. An example of a science image and its matching crmask is shown in Figure 3-6.

The key output from this step is the crmask file which can be used during *imcombine* of the science images. CR cleaned science files are a by-product and are not used further in the image reduction. This description of CR masking is included for completeness only, as *imcombine* removed CR artefacts effectively and crmask files were not used, see Section 3.13.

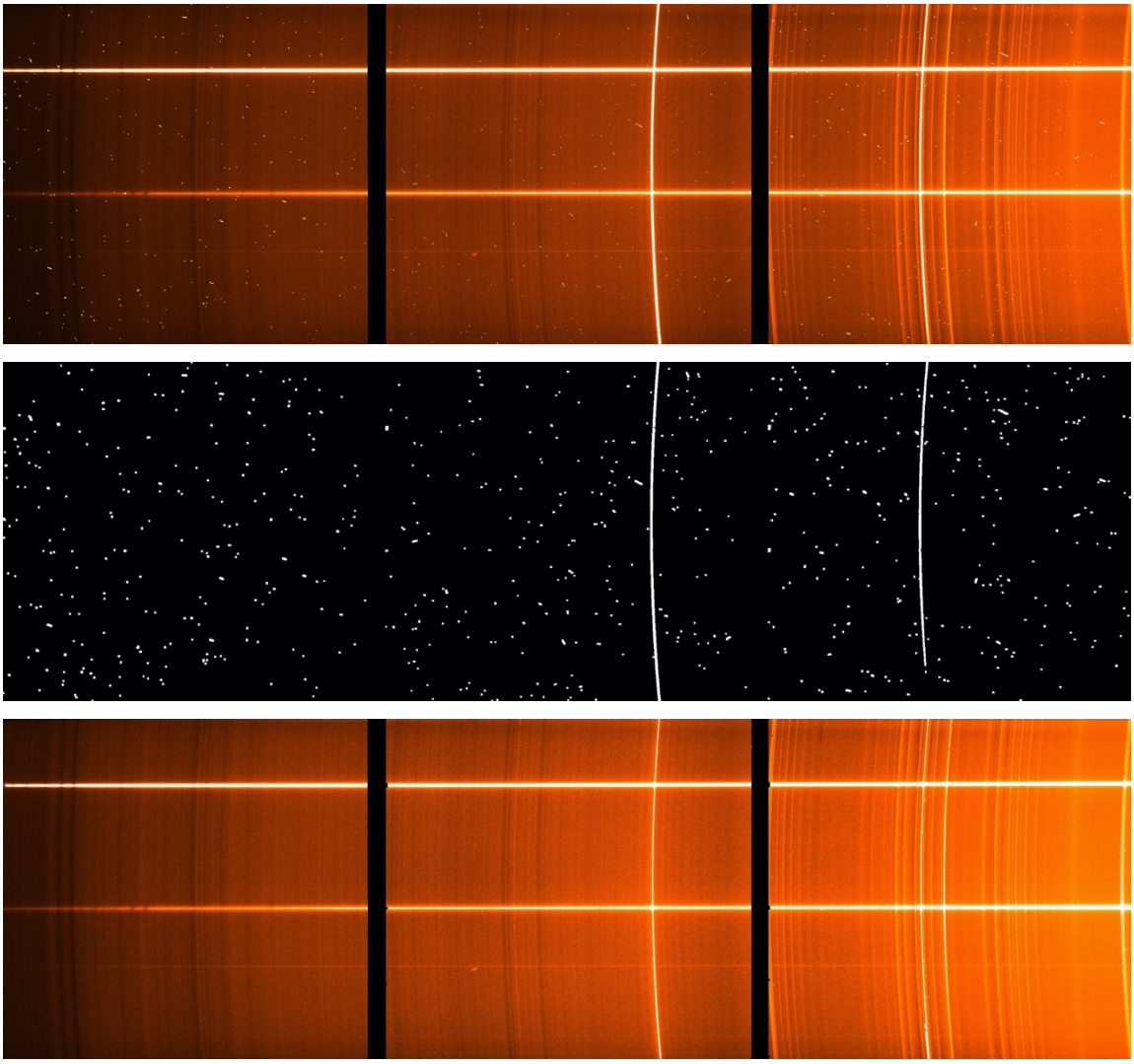

Figure 3-6: Example of a crmask for a science image from GAMA3576053. The top panel shows the input image with visible CR artefacts, middle panel shows the crmask and bottom panel the masked output science image. Importantly the masking process has identified CR artefacts, hot pixels and some brighter sky lines but has not masked any of the main spectral trace.

3.4 Wavelength Calibration of the Science Images

3.4.1 Determination of the transform task parameters

IRAF *transform* was used to convert science images from a pixel-based dispersion axis to a binned, wavelength calibrated dispersion axis in Å. *transform* accesses the pixel/wavelength solution from arc file calibration and applies it to the science images. The wavelength calibration was also used to –

1. linearize the dispersion axis – required for spectra to be fitted using pPXF.
2. adjust dispersion axis parameters to give a uniform start wavelength (x1), wavelength increment (dx) and number of increments (nx) for all science images.
3. apply these calibration and dispersion changes to the crmask files to ensure pixel to pixel mapping between science images and their masks.

transform allows specification of the start wavelength (*x1*), end wavelength (*x2*), wavelength increment (*dx*) and number of increments (*nx*) on the dispersion axis, where specification of any three of these parameters determines the fourth. Values of *x1*, *dx* and *nx* were specified, based on the dispersion (Å/pixel) and spectral resolution (Å) achieved by SALT/RSS. The spectral resolution was calculated from a sample of wavelength calibrated arc images using the gaussian fitting functionality in *splot* to determine the full width at half maximum (FWHM) of non-saturated arc lamp lines at 3949, 4045, 4511, 5559, 6032 and 6677Å. Results showed a range of spectral resolutions from ~5.5Å at the blue end of the spectrum to ~4.5Å at the red end. Therefore, from Equation 2-1, for a mid-spectrum wavelength of 5341Å, R = 1068 and the measured instrument dispersion = 119 km s^{-1} FWHM.

Given the nominal dispersion of 0.96Å per binned pixel (Table 2-1), a *dx* value of 1.25Å was chosen to be greater than the dispersion and approximately 1/3 of the spectral resolution. A *x1* value of 3770Å, chosen to be just longer than the shortest blue edge wavelength measured in the input science images, and a *nx* value of 2440 fixes the red end of the spectrum at 6820Å.

3.4.2 Science Image Wavelength Calibration

All science images were wavelength calibrated using parameters from Section 3.4.1 by calling *transform* using an IRAF script which produced and processed lists of input files. The parameter *interptype* was set to linear, to force a linear interpolation between bins and the parameter *flux* was set to yes to perform a weighted averaging of flux during linear interpolation. The outputs are science files with a linearised and wavelength calibrated dispersion axis with known parameters. An example of a transformed science file is shown in Figure 3-7.

A wavelength calibrator was required for GAMA65075, as the SALT Data Archive did not provide accompanying arc files. Testing showed that the wavelength solution from GAMA99686_arc_065 gave an acceptable wavelength transformation based on the wavelengths of major sky-lines in calibrated images. Minor discrepancies in the wavelengths between the two GAMA65075 observation nights were corrected by using the parameter *offsets* during GAMA65075 *imcombine* step, see Section 3.13.

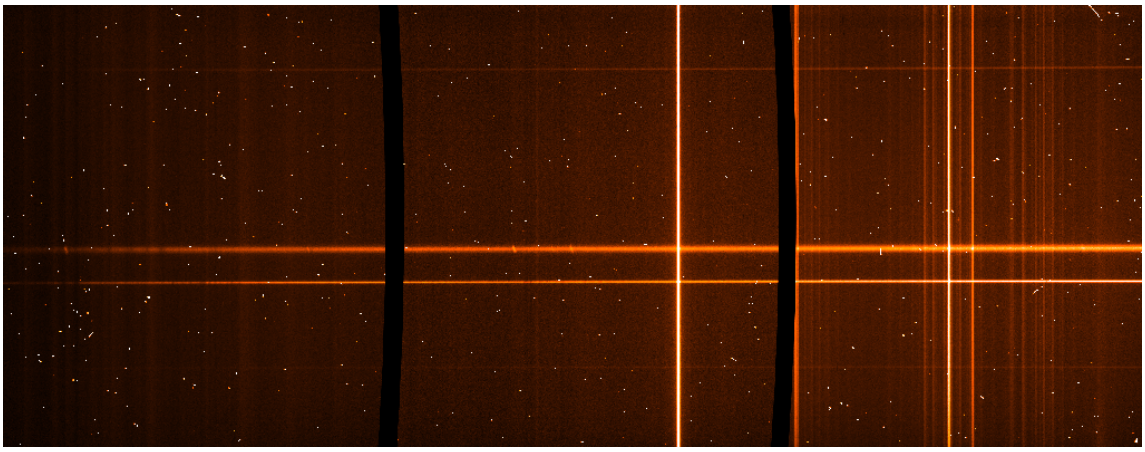

Figure 3-7: The image shows an example science file from GAMA569555 after wavelength calibration. Spectra appear as horizontal lines, skylines are now vertical and straight, and CCD gaps are curved. Note that cosmic ray artefacts are still present.

3.5 Sky Background Subtraction

The night sky is a source of low-level light due to scattered sunlight, e.g. from the Moon, and scattered artificial light, which produces a background continuum light level varying from place to place and night by night. In addition, there are emission lines produced in the upper atmosphere by recombination of atoms/molecules that were ionised/photodissociated by sunlight during the day e.g. prominent [OI] sky lines at 5577.34, 6300.30 and 6363.78Å. IRAF *background* was used to subtract this sky background light from the science images. *background* begins by fitting a low order polynomial to the spatial shape of the image, it then uses this polynomial to scale a user selected sample of sky background (statsec) and finally it subtracts the scaled background sample from the image. The order and function of the polynomial used and the statsec were chosen to optimise background removal.

Chebyshev and spline3 fitting functions at orders of 3, 5 and 9, were tested and the effectiveness of the fitting was assessed using the RMS calculated by *background*. Higher orders overfitted the spatial shape leading to edge effects, without significantly reducing the RMS. An order 3 spline3 function gave satisfactory fitting of the spatial shape without overfitting.

The target galaxies occupy <1 arcmin at the spatial centre of the 8 arcmin slit. This allowed the statsec to be chosen from clear sky, avoiding the spatial edges of the science images, residual light from the wings of the target galaxy and additional light sources in the slit e.g. stars. An example of a science image before and after sky background subtraction is shown in Figure 3-8, illustrating removal of diffuse background light and weaker sky lines. Traces of the strongest sky lines at 5377 and 6300Å remain in

background subtracted images for some targets and these, together with artefacts associated with chip gaps were removed later in data reduction.

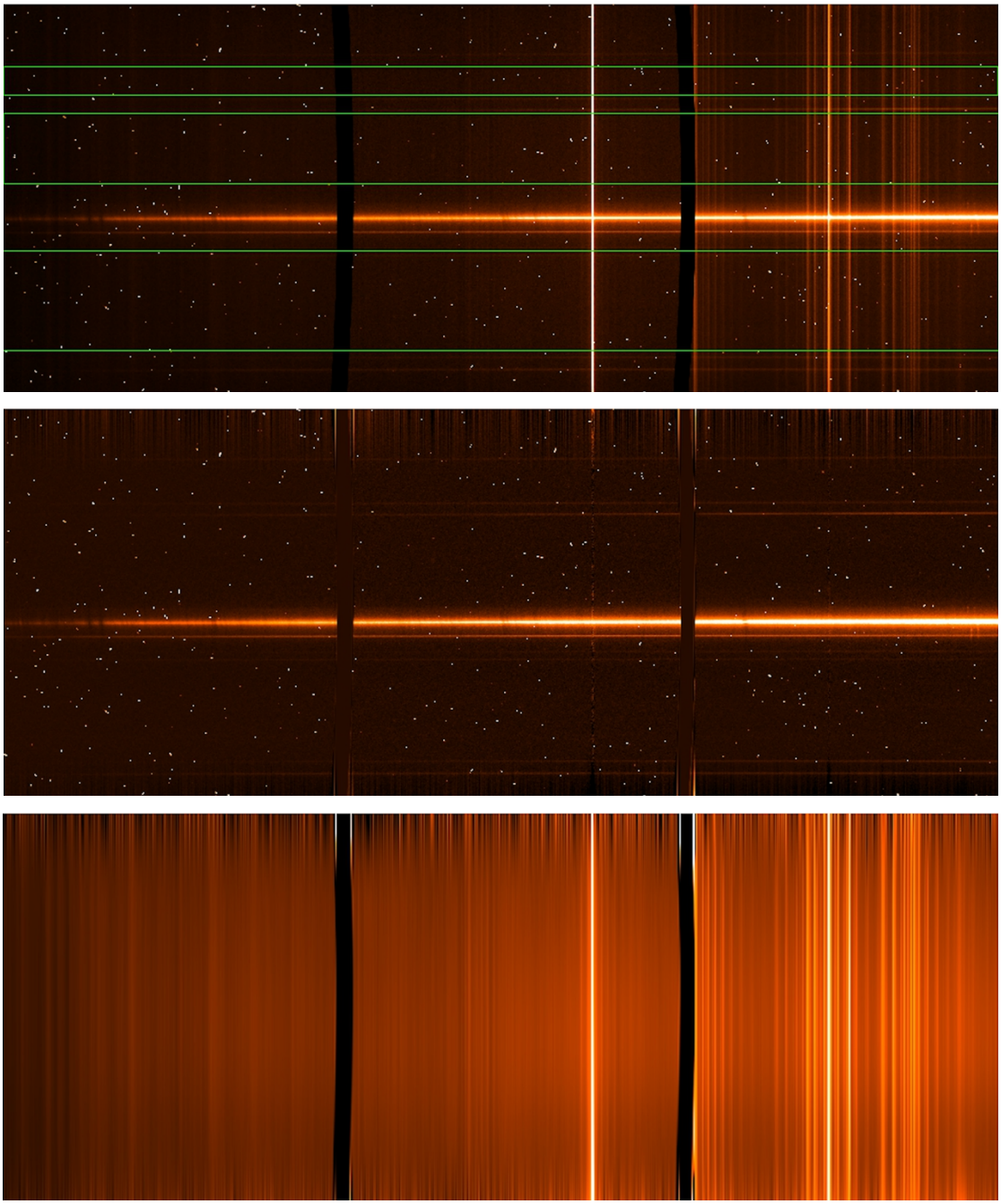

Figure 3-8: An example background subtraction for GAMA422436. The top panel shows the science image before background subtraction, with sky background and atmospheric emission lines clearly visible and statsec zones outlined in green. The middle panel is after background subtraction, showing CR artefacts, chip gap artefacts and remaining sky-line traces. The bottom panel is a diagnostic image generated by subtracting the middle panel from the top panel to show light removed by background subtraction.

To determine the optimum order of steps, two options for background subtraction were tested –

1. combine individual science images, then subtract background from the combined image.
2. subtract background from individual science images, then combine.

Option 2 gave a better background subtraction based on the standard deviation (SD) of the background, determined for a small sample area using *imstat*. Option 2 was adopted as the standard process, as shown in Figure 3-1.

3.6 Correction for Atmospheric Extinction

Atmospheric extinction is absorption and scattering of photons in Earth's atmosphere, by Rayleigh scattering by molecules, aerosol scattering by particulates and absorption by atmospheric O_2 and N_2, resulting in a reduction in flux available for astronomical observations. The amount of extinction is dependent on –

- wavelength. In optical bands blue wavelengths suffer from higher extinction than red wavelengths
- airmass, which in turn depends on location, altitude and zenith angle of the target object.

In general, absorption from atmospheric O_2 and N_2 happens mostly in UV and IR bands (Appenzeller, 2013), i.e. outside the wavelength range selected for this project. However, as airmass may vary with time atmospheric extinction correction was performed on all background corrected science images using IRAF *extinction*. This applies a wavelength dependent correction factor to the image, calculated from –

1. airmass, which is accessed from the AIRMASS keyword in the FITS image header, and
2. the value of extinction vs. wavelength specific to SALT, tabulated in the suth_extinct.dat file[11]. The SALT extinction curve was checked by comparison with extinction curves for Kitt Peak National Observatory (KPNO) and Cerro Toledo Inter-American Observatory (CTIO), see Figure 3-9.

3.7 Geometric Distortion Correction

Due to small misalignments in the optics and aberrations from components in the light path, the trace of a longslit spectrum will have geometric distortions, which alter the trace from a straight line aligned parallel to the dispersion axis. An example is given in Figure 3-10, which shows a monotonic increase in spatial position of the centre of the trace of approximately 4 pixels from the blue to red end of the spectrum. Geometric

[11] Available from: http://pysalt.salt.ac.za/data/site/suth_extinct.dat

distortion correction was performed on all science images using IRAF *apall* with format=strip, to produce 2D science images with the centre of the science trace aligned to the dispersion axis along y-pixel row 201.

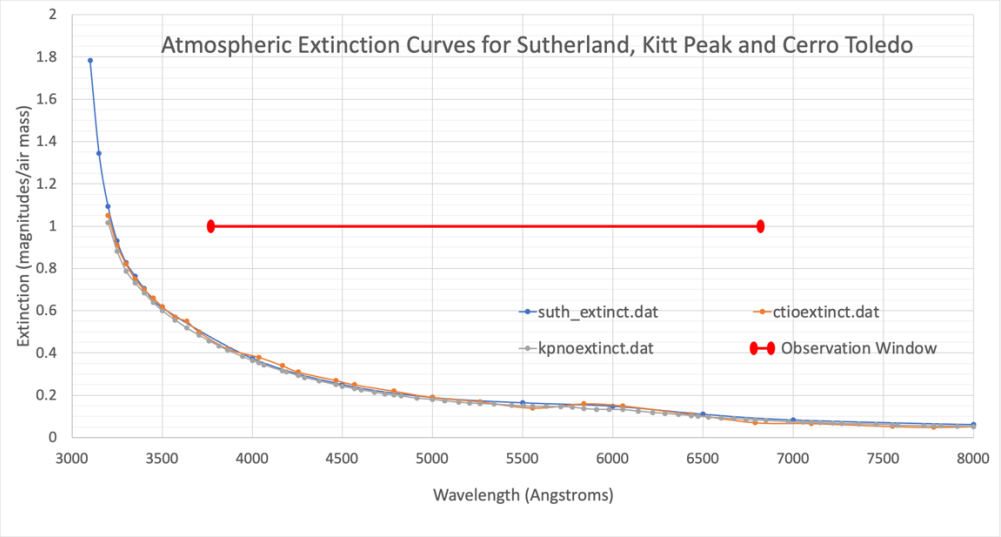

Figure 3-9: Comparison of extinction curves for SALT, KPNO and CTIO. SALT shows marginally higher extinction due to its lower altitude. The red line represents the wavelength range used in data reduction. Data for this plot was taken from suth_extinct.dat, kpnoextinct.dat and ctioextinct.dat files.

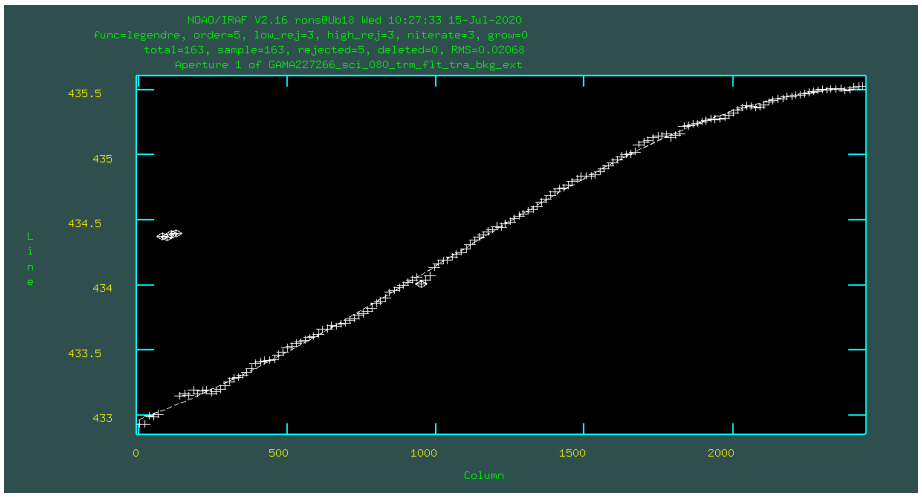

Figure 3-10: A typical trace of the peak of a 2D science spectrum using IRAF *aptrace*. The spatial centre of each column is marked with + and the polynomial fitted to the spatial centre by *aptrace* is shown as a dotted line. Outliers are excluded by the fitting algorithm and are marked with ◇. Geometric distortion in the spatial direction is clearly visible from the polynomial shape and its deviation from parallel to the dispersion axis.

Galaxies are diffuse targets, therefore it was important to select a spatial strip size that includes all light from the target as *apall* strip reduces the number of spatial pixels. The spatial extent of the trace was assessed using *implot*, which showed that a strip of ±200 spatial pixels around the centre of the trace, would capture diffuse light from all targets. This was equivalent to 10 × the half-light radius (R_e) of GAMA227266, the galaxy with

the largest R_e in the sample. In addition, there is strong vignetting along the 8 arcmin slit, and selection of a 401 pixel width spatial strip (equivalent to ±1.7 arcmins) around the centre line limited vignetting to ~5%, as illustrated in Figure 3-11. GAMA79849, 227264, 227266, 298980, 422436, 560238 and 569555 had other light sources in the RSS slit within ±200 pixels of the centre of the science trace. During aperture tracing for these targets the science trace was manually selected in IRAF *aptrace*.

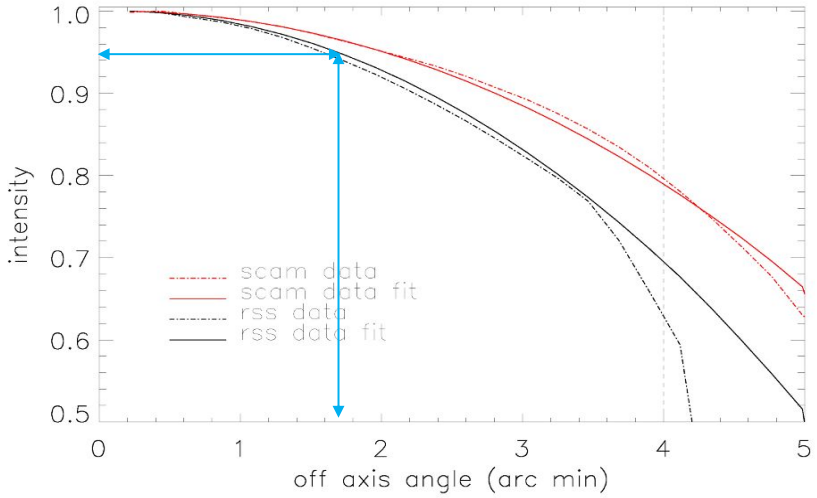

Figure 3-11: Plot of intensity vs. angular position along the slit for the RSS, showing reduction in signal intensity with increasing off-axis angle. A strip width of ±200 binned spatial pixels, at 0.5068 arcsec/pixel is shown by the vertical blue arrow. Image adapted from SALT Ast Ops (2020).

3.8 Interpolation of the Chip Gaps

The science spectra contain spikes caused by edge effects at the chip gaps. IRAF *fixpix* was used to perform linear interpolation across these artefacts, see Figure 3-12 for an example, with the width of the interpolated zone determined individually for each target. Interpolated areas do not contain useful information and were masked before spectral fitting.

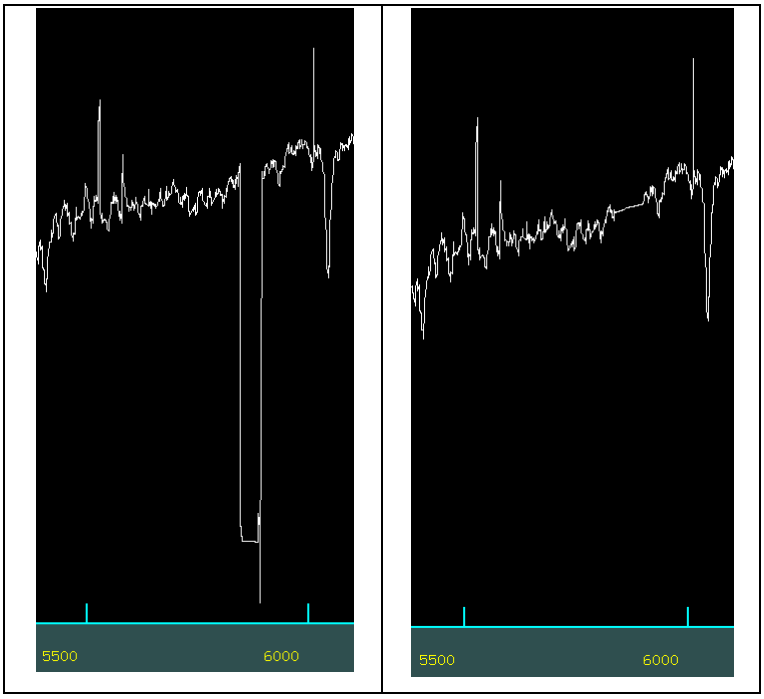

Figure 3-12: Illustration of linear interpolation across the gap between central and right-side chips. The left panel shows the gap before interpolation, where flux drops to zero and there are artefacts at the chip edges. The right panel shows interpolation which has removed the zero flux zone and chip edge artefacts. Both panels also show spikes caused by remaining flux from [OI] sky-lines at 5577Å.

3.9 Reduction of Photometric Standards

Spectra for photometric standard stars, observed using the same instrument setup as the science images except with a slit width of 4 arcsec, were downloaded using the SALT Web Manager[12]. The 4 arcsec slit width vs. 1 arcsec for science observations affects spectral resolution but not the wavelength solution and is required to ensure that sufficient light is received from standard stars. The primary use of standard stars is for correction of the science spectra shape, as absolute flux calibration is impractical due to the variable pupil of SALT, see Figure 2-2. Arc files used for wavelength calibration of standard stars were selected from arc files taken during science observations as close as possible in time to the standard star observations. Table 3-2 presents an analysis of the wavelength calibration and spectral resolution of a sample of standard star spectra observed on dates close to the science observations. The data reduction process for raw standard star spectra is shown in Figure 3-13.

[12] Available at - https://www.salt.ac.za/wm/

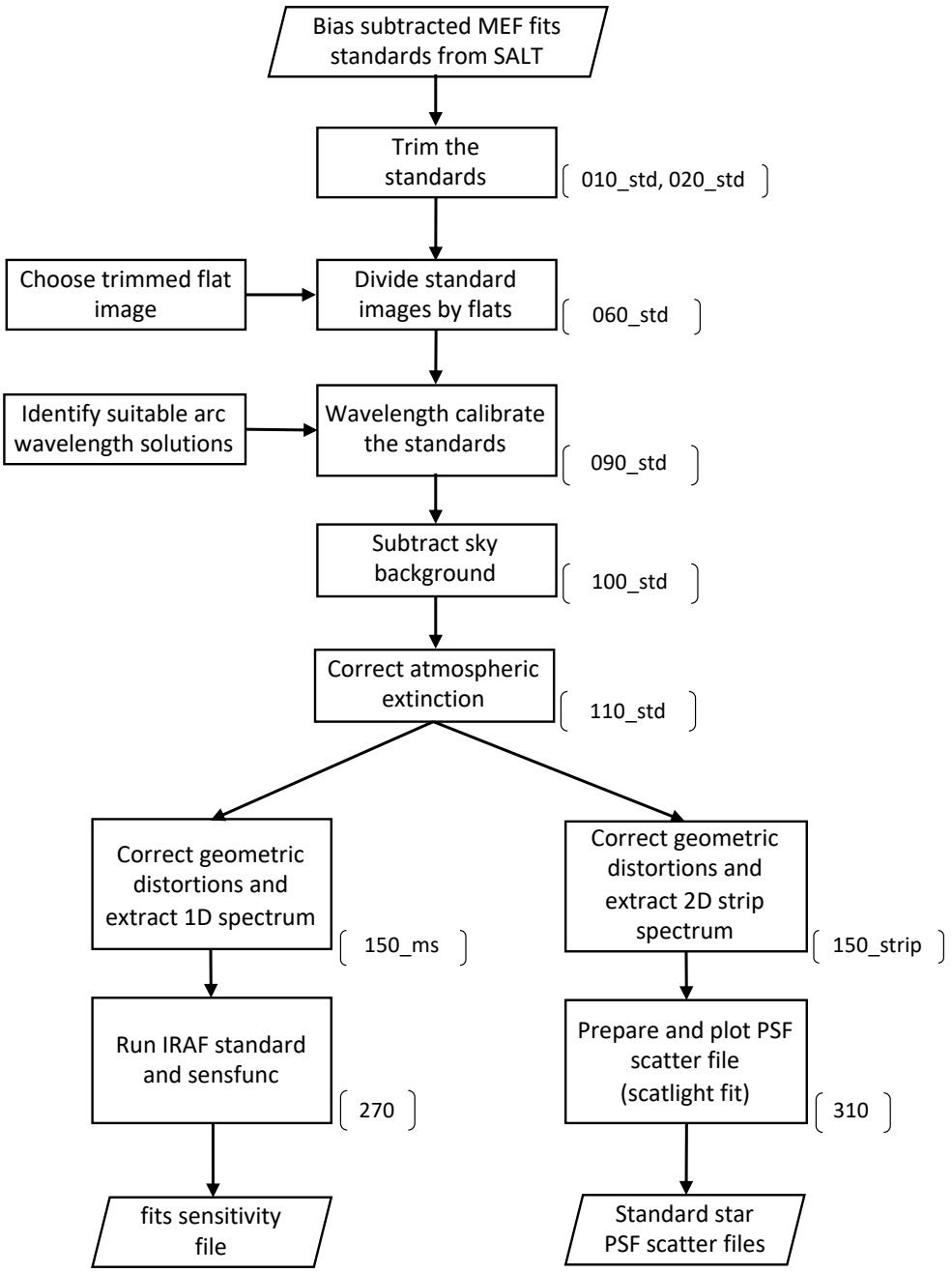

Figure 3-13: Summary of steps in the data reduction of standard stars. The left branch generates sensitivity functions for flux calibration from 1D spectra. The right branch generates PSF files for scattered light removal see Section 3.10. Numbers in brackets identify script(s) used at that step.

Reduction started with IRAF tasks and parameters similar to reduction of science images, up to production of wavelength calibrated, distortion corrected standard star images. Removal of CR artefacts was not required for the standard star spectra because of their relatively short exposure times. IRAF *apall* with 'multispec' format was used to create 1D geometric distortion corrected standard star spectra in addition to 2D strip spectra. The 1D spectra were further reduced to produce a sensitivity function, using a two-step process. Firstly, IRAF *standard* was used to create a data file associating an extinction curve (Hamui *et al.*, 1994) from IRAF 'onedstds' library, to each standard star

spectrum. Secondly, this data file was processed by IRAF *sensfunc* to produce a sensitivity function, characteristic of the observing setup, for each standard star. These sensitivity functions were later used to correct the shape of science spectra using IRAF *calibrate* (Hainline, 2015). The 2D geometric distortion corrected standard star spectra were further reduced to point spread function (PSF) scatter files as described in Section 3.10.

Wavelength calibration was checked for a sample of standard stars covering the time period of science observations by measuring the FWHM and peak wavelength of the 5577.34Å sky-line after wavelength calibration. This gave an indicative spectral resolution of 14 to 16Å and a peak wavelength from 5570 to 5576Å, see Table 3-2. These results are in close agreement with the theoretical spectral resolution of 15.3Å at 5341Å calculated by the RSS Simulator, and the expected peak wavelength of 5577.34Å. Standard star spectra are used for flux calibration and scattered light removal, neither of which are highly wavelength critical processes, therefore, the arc files gave a satisfactory wavelength calibration.

Table 3-2: Key information for SALT photometric standards used in data reduction.

Standard Star	Observation	Flat	Arc	5577.34Å sky-line		Comment
				FWHM Å	Peak λ Å	
EG21	P201309240114.fits	2014	GAMA79849_arc_079	14.2	5569.9	for GAMA65075 scattered light
LTT4816	P201408030004.fits	2014	GAMA79849_arc_080	14.4	5573.6	for GAMA65075 flux
LTT4364	P201905240037.fits	2019 Semester 1	GAMA570227.arc.048	14.8	5575.9	for SALT Semester 2019-1 flux
LTT1020	P202001270036.fits	20191206	GAMA3576053.arc.063	14.0	5573.5	for SALT Semester 2019-2 flux
LTT4364	P202005300038.fits	20200514	GAMA227264_arc_088	15.1	5576.8	for SALT Semester 2020-1 flux
LTT4364	P202007170040.fits	20200622	GAMA227266.arc.078	16.1	5570.1	for SALT Semesters 2019-1, 2019-2 & 2020-1 scattered light
EG21	P202101090036.fits	20210222_1	GAMA546040_arc_079	16.4	5575.7	for SALT Semester 2020-2 flux & 2020-2 scattered light

As photometric standard stars were not observed on the same nights as science observations the following criteria were used to match a standard star to a science observation –

1. aim for a standard star observation made reasonably close in time to the science observation. Advice from SALT (personal communication from P. Vaisannen 09/07/2020) indicates that an acceptable correction of spectral shape can be achieved using a standard observed within months of the science observation
2. use one standard for all observations of a target, even if the target was observed across multiple nights
3. avoid mixing science observations/standards across the major RSS optics service in Feb 2020.

To confirm stability of the sensitivity function with time, all observations for standard stars LTT4364 and LTT1020 were reduced to sensitivity function files using the process shown in Figure 3-13. An order 3 spline3 function was chosen for fitting all standard star spectra, as this gave RMS values of ~0.02 mag for all the fittings. Higher order fittings did not significantly improve the RMS but did cause significant overfitting at ends of the wavelength range. An example output from IRAF *standard* and *sensfunc* is shown in Figure 3-14.

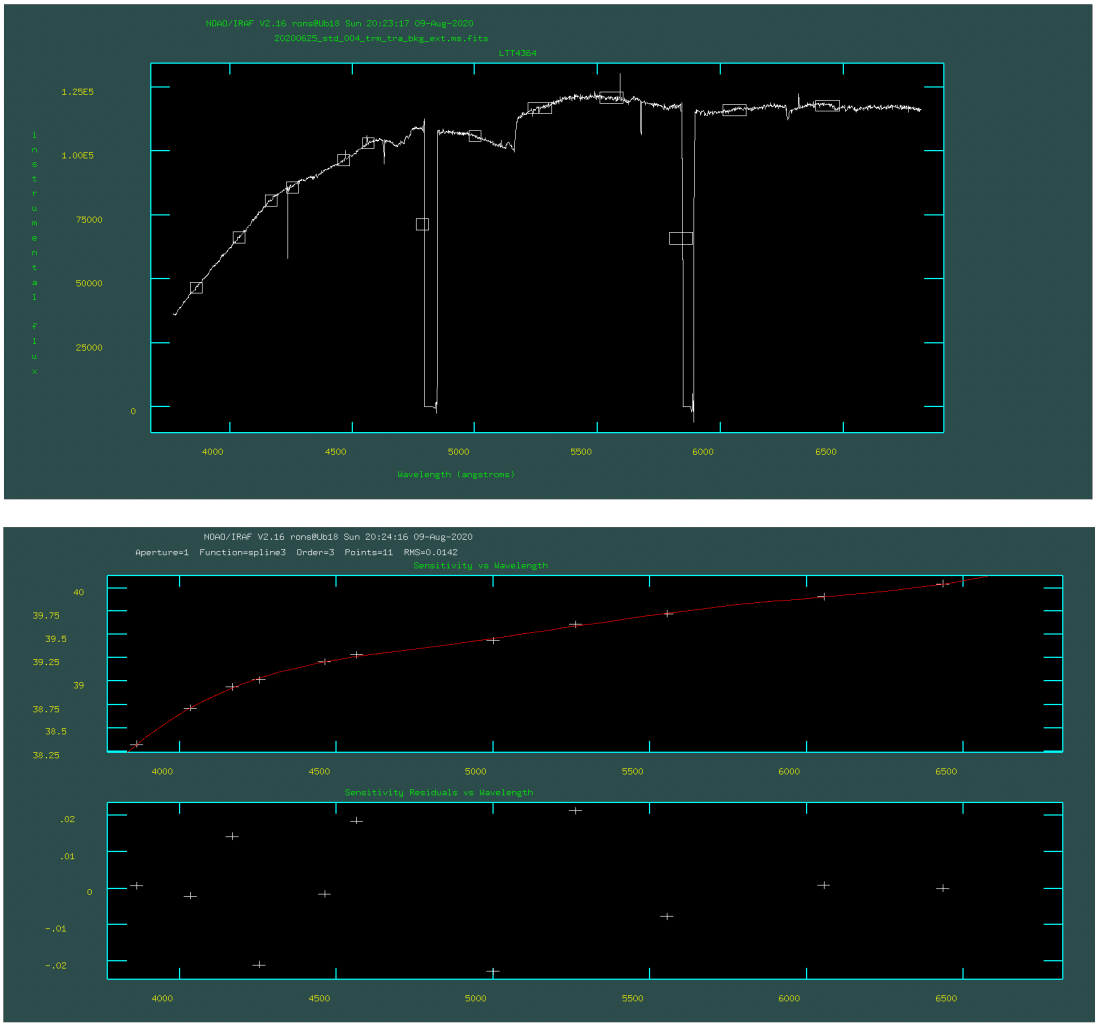

Figure 3-14: The upper panel shows an example output from IRAF *standard*. White rectangles show points in the spectrum where the internal flux standard file is being associated with the observed standard star spectrum. Two of these points are in chip gaps and were removed. The lower panel shows an example output from *sensfunc*. The upper plot shows the sensitivity function, with wavelength on the x-axis and magnitudes on the y-axis, and the bottom plot shows fit residuals.

Sensitivity functions generated by this process were normalised and plotted, confirming that sensitivity curves vary by only ~0.1 mag, i.e. ~ ±5% flux, over the time period. Based on the above criteria the following standard star observations were selected for flux calibration. Sensitivity curves for these stars are presented in Figure 3-15 –

- SALT Semester 2019-1 – LTT4364 observation from 20190524

- SALT Semester 2019-2 – LTT1020 observation from 20200127
- SALT Semester 2020-1 – LTT4364 observation from 20200530
- SALT Semester 2020-2 – EG21 observation from 20210109
- GAMA65075 – LTT4816 observation from 20140803

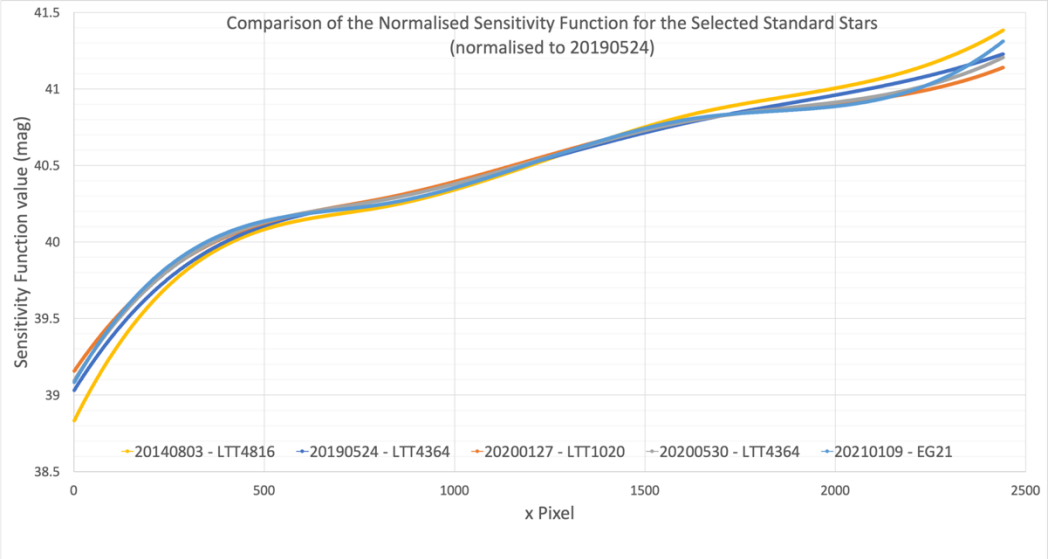

Figure 3-15: Normalised sensitivity functions for standard stars selected for flux calibrations. These observations confirm the stability of the standard star sensitivity functions over an extended time-period.

3.10 Compensating for Scattered Light

Recent work has shown that spectra obtained from the RSS are affected by light from the astronomical target being partially scattered within the instrumentation light path, for example by a build-up of dust. This results in redistribution of light, in both spatial and spectral directions, in sufficient quantities to broaden and reduce the contrast of spectral absorption features (Katkov *et al.*, 2019). When using full spectral fitting for analysis of stellar kinematics and populations, broadening of absorption features will cause an overestimate of the calculated velocity dispersions and reduction in contrast of the absorption features will give a systemic bias towards younger stellar populations. Therefore, the method of Katkov *et al.* (2019), and its accompanying 'scatlight.py'[13] Python script, was adopted for this project to compensate for scattered light.

The method for calculating the spatial profile of scattered light is summarised in Figure 3-16 in which the blue line represents scattered light vs. spatial position. The scattered light profile is determined from a longslit spectrum of a point source, e.g. a standard star, and is then applied to spectra of the target galaxies to remove their scattered

[13] Available at - https://github.com/ivan-katkov/scatlight/blob/master/scatlight.py

light component. To assess the effects of scattered light, data reduction steps following scattered light subtraction were performed in parallel on the original geometric distortion corrected 2D spectra and the geometric distortion corrected 2D spectra from which scattered light had been removed, see Figure 3-1.

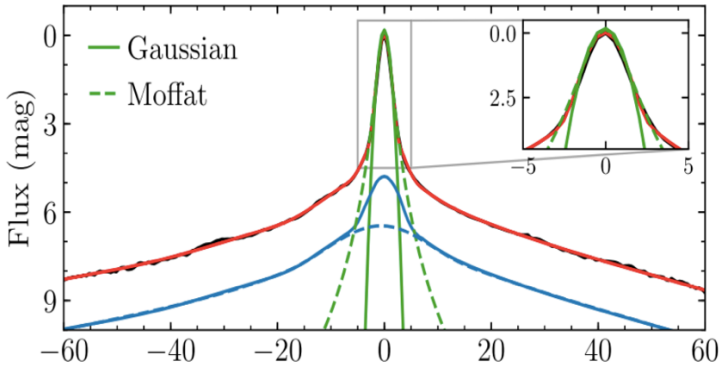

Figure 3-16: This diagram, from Katkov et al., (2019), shows flux vs. spatial position (arcsec). The black line represents the spatial light profile of the standard star. The solid green line is a Gaussian (or dashed green Moffat) function fitted to the peak of the black line, representing the point spread function of atmosphere and instrument (PSF_{atm}). The blue line shows a scatter function (PSF_{scat}), created from fitting a combination of Gaussian and exponential functions, such that convolution of the scatter function and the point spread function i.e. PSF_{scat} * PSF_{atm}, is shown by the red line. The Gaussian and exponential functions are chosen to optimise the fit of the red line to the black spatial light profile.

3.10.1 Determination of Scattered Light Profiles

A scattered light profile, i.e. a binary fits table with file name *_psfscat.fits, was generated from 2D strip spectra of selected standard stars, using scatlight.py with command line option 'fit', see Figure 3-13. Other command line options were used to determine the fitting parameters, and experimentation showed –

1. *ngaus* <3 and *nexp* <3 resulted in underfitting of the calculated scattered light component giving a poor fit to the spatial light profile, while *ngaus* >3 and *nexp* >3 resulted in overfitting, causing spurious peaks to appear in the scattered light profile
2. a Gaussian function with a *maxfrac* value of 0.1 fits the top 90% of the central peak of the standard star 2D strip spectrum
3. a window size of 100 pixels on each side of the spatial centre of the trace was sufficient to cover the spatial extent of the scattered light profile
4. selection of the *cocentered* parameter was needed to force the fitted curves to have the same spatial centre.

The scatlight.py default sampling bins at red and yellow wavelengths were modified to one red bin at 6020-6100 Å and one blue bin at 4300-4400Å, to ensure coverage of the spectral range for this project. Testing indicated that sampling at these wavelengths

prevented overestimation of mid-spectra scattered light. To determine variation of the scattered light profile with time and with standard star sampled, scattered light profiles were developed for a range of selected SALT standard stars. Examples are shown in Figure 3-17 where the top panel shows a symmetrical scattered light profile, calculated from standard star LTT4364 observation on 20200717, and the lower panel shows an off-centre scattered light profile, calculated from standard LTT1020 observation on 20190920. The latter is typical of many scattered light profiles generated by scatlight.py. Scattered light is due principally to a build-up of dust in the optical path (Kniazev, 2020 personal communication), and should be spatially symmetrical about the centre of the trace. Therefore, asymmetric profiles were rejected as not physically feasible, and were not used for data reduction.

3.10.2 Selection of the Scattered Light Profile

To assess if there were any trends with time in the shape of scattered light profiles, scattered light in the science spectrum of an example galaxy (GAMA272990) was calculated using profiles from five SALT standard stars observed between February 2019 and January 2021, see Figure 3-18. Profile shapes are similar in both the red and blue sample bins, indicating that scattered light profiles do not vary significantly with wavelength. The grouping of lines shows reproducibility across all scattered light profiles over this two-year period, confirming that the scattered light performance of SALT changes slowly with time as indicated by Kniazev (personal communication). Therefore, the scattered light profile from SALT standard star LTT4364 observed on 20200717 was selected as representative and was used for scattered light correction of all science spectra from the 2019 and 2020 SALT Semesters. Observations of GAMA65075 from 2014 were scattered light corrected using the scattered light profile from SALT standard star EG21 observed on 20130325. Figure 3-18 illustrates reproducibility of scattered light profiles including the 2013 observation, especially within ±10 spatial pixels of the centre of the trace.

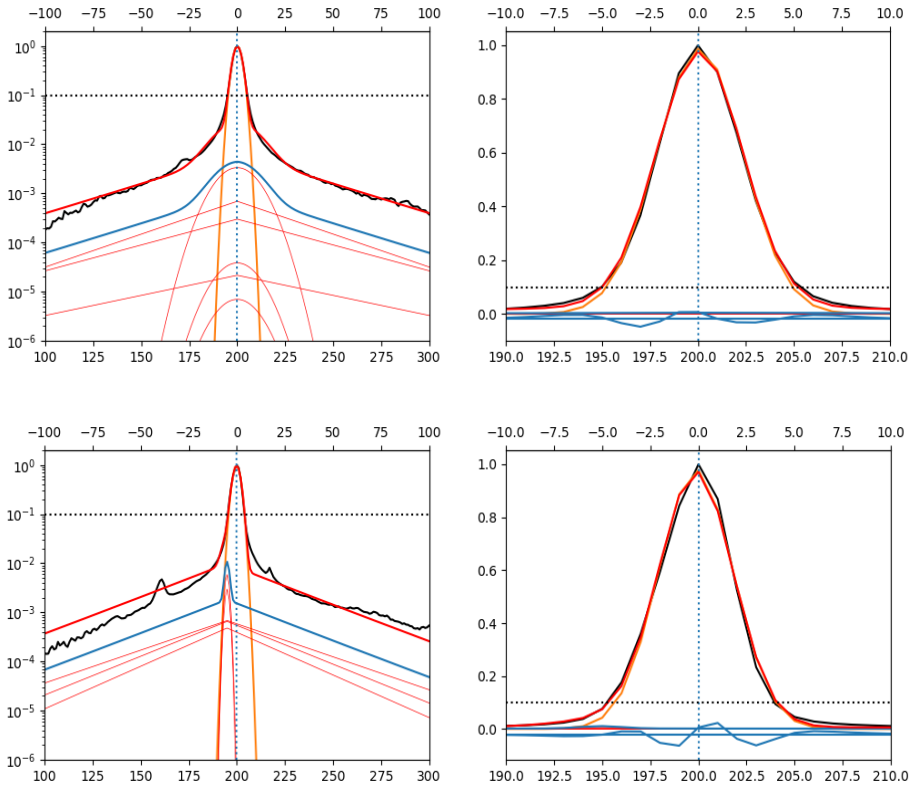

Figure 3-17: Examples of scattered light profiles produced using scatlight.py 'fit' functionality. The x axis is binned pixels, shown as actual x pixel row across bottom of the plot and relative to the peak of the trace across top of the plot. The y axis is light intensity, normalised to peak of the science trace. Left panels show scattered light on a log scale and right panels on a linear scale, focussing on peak of the trace. The line colour key is as described in Figure 3-16, with addition of an orange line which represents the Gaussian used to model the peak and pink lines representing Gaussian and exponential functions used for fitting.

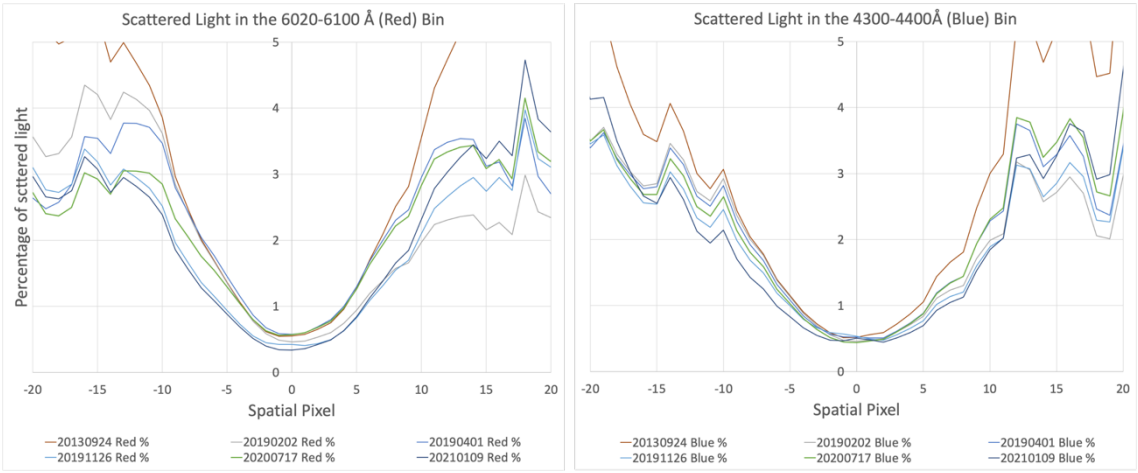

Figure 3-18: Amount of scattered light vs. spatial position in the science spectrum of an example galaxy (GAMA272990), calculated using profiles of five SALT standard stars observed between February 2019 and January 2021. The left plot shows the red scatlight.py bin and right plot the blue bin. The profile selected for scattered light removal from the 2019 and 2020 SALT Semesters science spectra is shown in green. The profile used for correction of observations of GAMA65075 from 2014 is shown in dark red.

3.10.3 Scattered Light Correction of 2D Science Spectra

Scattered light correction of the science spectra was performed before interstellar extinction correction and flux calibration as scattered light profiles were generated from standard star spectra which had not been interstellar extinction corrected or flux calibrated. The selected scattered light profile was applied to the 2D strip science spectra using the scatlight.py script with command line option *jopa* to generate two outputs –

- individual 2D strip science spectra with a filename containing _scat_substr.fits, from which scattered light had been removed. These are inputs to the next step in data reduction.
- 2D strip spectra with a filename containing _scatlight.fits, as diagnostic images showing the scattered light that had been removed.

2D strip science spectra, with and without scattered light removed, were taken through the remaining steps of data reduction in parallel, as shown in Figure 3-1. Measurement of FWHM of the Na D doublet absorption feature for a sample of the target galaxies showed that removal of scattered light had narrowed the features marginally, i.e. of order ~0.1Å. The downstream effect on the 1D spectra is discussed further in Section 3.14.3.

3.11 Correction for Interstellar Extinction

The interstellar medium of our Galaxy, particularly interstellar dust with particles of 0.01-0.1 μm, absorbs and scatters photons resulting in interstellar (Galactic) extinction, with shorter wavelengths experiencing greater scattering. IRAF *deredden* was used to correct for Galactic extinction using the absolute extinction value for each target, which IRAF calculates from –

$$A(V) = R(V) \times E_{(B-V)} \qquad \text{Equation 3-1}$$

Where –

$A(V)$ = absolute extinction value

$R(V)$ = ratio of absolute extinction to colour excess

$E_{(B-V)}$ = colour excess, specified through the *value* keyword

The value $E_{(B-V)}$ of was obtained from the GAMA Catalogue, see Table 2-2, and R(V) was set to 3.1, the default value adopted as typical by IRAF.

3.12 Flux Calibration

Flux calibration was performed on dereddened 2D strip spectra using IRAF *calibrate*, which applies the sensitivity functions from Section 3.9. The variable pupil of SALT makes absolute flux calibration impractical therefore, for this project, flux calibration serves to correct the spectral continuum shape rather than provide an absolute

measurement of flux. An example of the effect of flux calibration on the shape of a 1D science spectrum is shown in Figure 3-19.

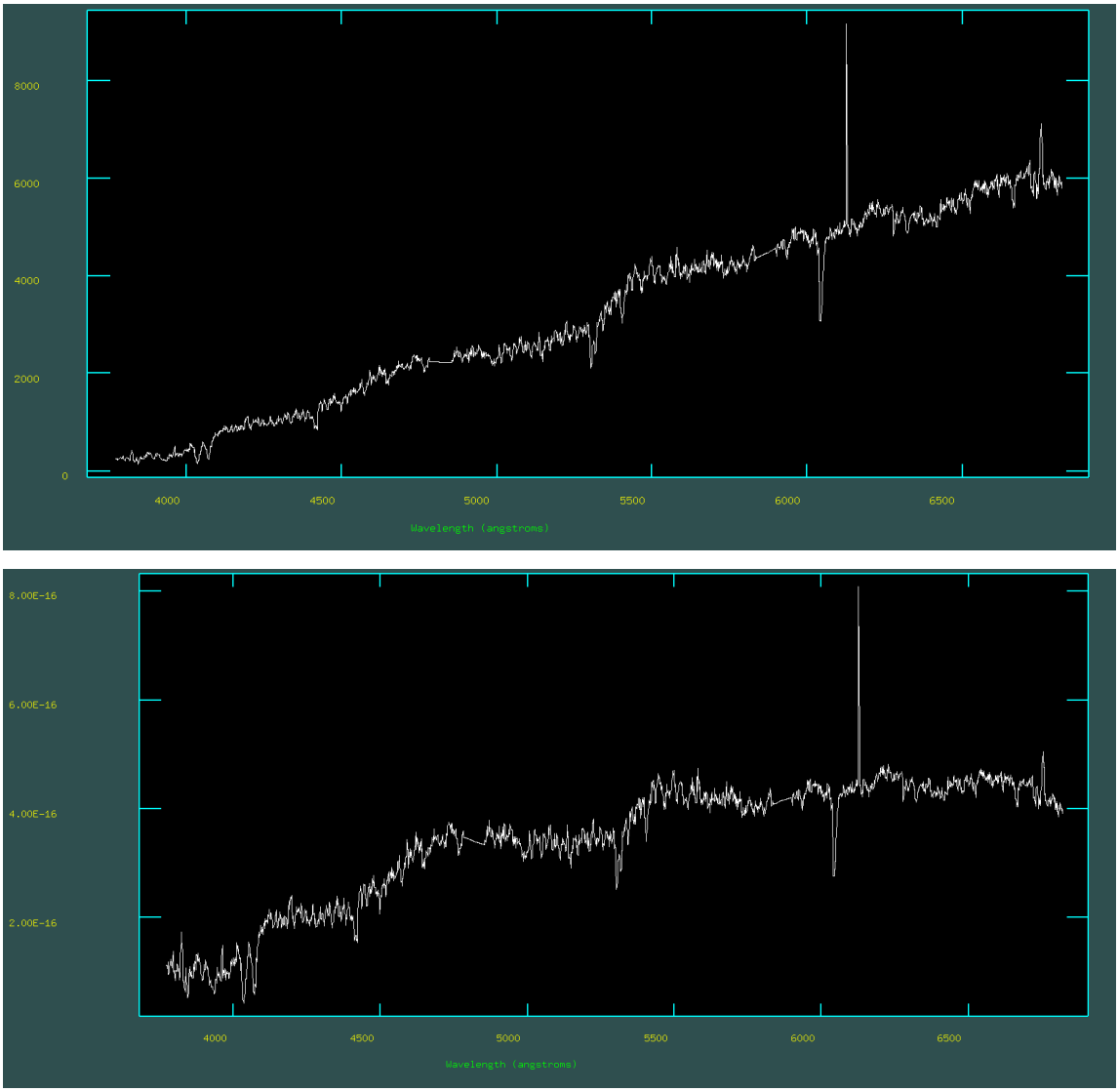

Figure 3-19: Examples of aperture 201 of a 2D strip science spectrum from GAMA422436. The upper panel shows the spectrum before flux calibration with the y-axis in counts and the lower panel after flux calibration with the y-axis in ergs/s/cm^2/Å. Comparison of upper and lower panels shows the change in shape of the spectrum with enhancement of blue wavelengths. Note the presence of a CR artefact at 6120Å.

3.13 Creation of Combined Images

The main purposes of creating a combined image are to improve S/N ratio and to remove CR artefacts. Individual 2D strip science spectra were combined into a single 2D strip spectrum for each target using IRAF *imcombine*. Testing of the process showed –

1. there were variations in overall light content between science images of a target galaxy, e.g. within six science images taken for GAMA3576053 there is a variation of ~×2 between the brightest and faintest image. Setting *scale*=mean

forced normalisation during image combination by adjusting each image intensity by the reciprocal of its mean pixel value

2. as all targets had at least three input images a median combine could be used to remove CR artefacts
3. inclusion of crmasks in the *imcombine* step generated dark artefacts within the bright emission features of some targets, without significantly improving the removal of CR artefacts. Therefore, as the median combine effectively removed CR artefacts, crmasks were not used.

The combined 2D science spectra were examined using DS9 to identify if there were any residual CR artefacts around the science trace and none were found. IRAF *imcombine* also generated a sigma image for each combined science image, which provides a quantification of noise in the science image.

3.13.1 Analysis of noise using the sigma image

Light from an astronomical object arrives at a detector as a random stream of individual photons, therefore noise associated with the resulting signal, known as 'shot noise', can be described by Poisson statistics (Bolte, 2006; Littlefair, no date). The Poisson distribution has a standard deviation $\sigma = \sqrt{N}$, where N is the number of photons detected. Therefore, for astronomical signals, e.g. the arrival of photons at a detector, the noise can be estimated as square root of the signal.

Other sources of noise in the science images include read noise from the detector electronics, dark current noise and shot noise from the sky, all of which add in quadrature to give the overall noise. At the *imcombine* step values of pixels in a sigma image give a good indication of noise in each pixel of the combined science image. The sigma image for each target galaxy generated by *imcombine* was converted into a variance image by squaring using IRAF *imfunction* and then dividing by the number of science images that contributed to the combined science image using IRAF *imarith*. The variance images are used at a later step in data reduction to assess noise and to determine the position of S/N ratio based spatial bins for extraction of 1D spectra.

3.14 Extraction of 1D Binned Spectra

Flux reduces along the slit with increasing spatial distance from the galaxy centre, causing light from the target galaxy to blend gradually into the background and the S/N ratio to decrease as distance from the centre of the galaxy increases. To enable investigation of stellar kinematics and populations along the major axis of the target galaxies, 2D spectra were binned into a series of 1D spectra of approximately equal S/N

ratio at increasing spatial distance from the centre of each target. Figure 3-20 shows a summary of steps in data reduction of the 1D spectra.

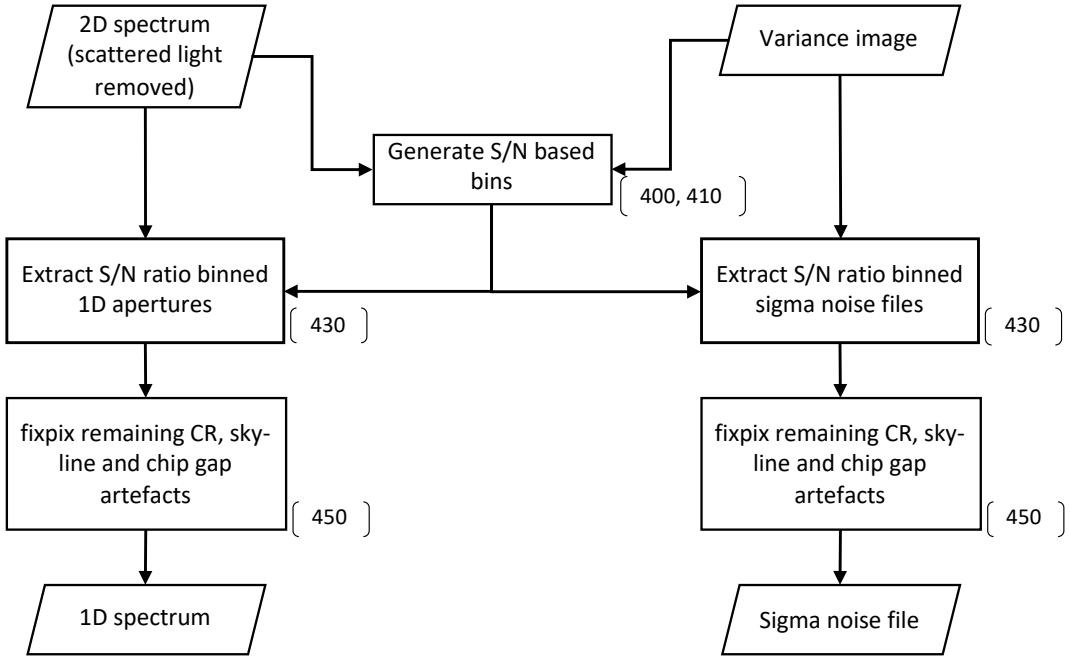

Figure 3-20: Summary of the sequence of steps in the data reduction of 1D spectra. Numbers in brackets identify script(s) used at that step.

3.14.1 Calculation of S/N Ratio Based Spatial Bins

The binning process took place in two steps –

- IRAF *transform* was used to extract spatial samples from 5000-5100Å from the combined 2D science strip spectra and their variance files. These FITS files were then converted to text files using IRAF *wtextimage*.
- the text files were processed using the BINBATCH[14] Fortran program which calculated the y-pixel location and spatial width of bins for S/N ratios of 20, 25, and 30.

Table 3-3 shows the numbers of spatial bins calculated for each target galaxy for each S/N ratio. This confirmed that scattered light removal reduced the S/N ratio, resulting in scattered light subtracted spectra having a lower number of bins at each S/N ratio. To enable identification of trends in the stellar kinematics and populations, ideally at least 5 bins would be used for each galaxy, however, at the target S/N ratio of 30, only 6 of the 16 target galaxies had ≥5 spatial bins. Therefore, where ≥5 bins were not available at a

[14] The BINBATCH code was provided by Dr A E Sansom and was compiled using Intel iFort version 2019.5.281

S/N ratio of 30 a lower S/N ratio was picked to deliver ≥5 spatial bins. The effects of using lower S/N ratio spectra are discussed in Section 7.

Table 3-3: Number of S/N ratio based spatial bins for each target galaxy. Cells highlighted in yellow show the number of bins at the highest S/N ratio with ≥5 bins.

Target Galaxy GAMA	Number of bins for each S/N ratio					
	Science spectra			Scattered light subtracted spectra		
	S/N = 20	S/N = 25	S/N = 30	S/N = 20	S/N = 25	S/N = 30
65075	19	14	9	13	10	9
78425	5	1	0	1	0	0
79849	12	7	5	9	5	4
85416	15	11	8	13	9	7
99687	9	6	4	9	5	4
136847	12	8	5	8	5	3
227264	11	7	4	8	5	3
227266	13	8	5	11	7	3
272990	13	10	7	11	7	6
298980	11	8	5	10	6	4
422436	30	23	15	25	16	11
546040	24	18	12	18	12	8
560238	37	28	25	30	26	25
569555	8	6	4	7	4	3
570227	7	4	3	5	3	1
3576053	8	5	3	6	4	3

3.14.2 Extraction of 1D Spectra from Spatial Bins

1D spectra were extracted from the 2D strip science spectra and scattered light subtracted spectra using IRAF *scopy*, with aperture parameters determined from the out_2profile_data.txt file from BINBATCH. To enable direct comparison of kinematic results obtained from spectra with and without scattered light subtraction, spatial bin parameters for the scattered light subtracted spectra were used for extraction of all 1D spectra.

3.14.3 Effect of Scattered Light Subtraction on 1D Spectra

As discussed in Section 3.10.3, scatlight.py removes scattered light from 2D spectra along both spatial and dispersion axes. The upper panel of Figure 3-21 illustrates the reduction in flux in a subsequent 1D spectrum and the lower panel confirms that scattered light removal did not cause any significant changes to the shape of the spectrum. The increase in relative flux at extreme ends of the spectrum, seen in the lower panel of Figure 3-21, indicates a fitting issue at the boundaries and these wavelengths were excluded from analysis of stellar kinematics and populations.

3.15 Removal of the Remaining Artefacts from the 1D Spectra

This step removes remaining residual sky-line artefacts from the 1D spectra, as these could affect fitting of library spectra by pPXF. As discussed in Section 3.8, the method chosen for removing artefacts was linear interpolation using IRAF *fixpix,* with a mask file

containing pixel locations of the sky-lines, shown in Table 3-4. After interpolation the 1D spectra were visually checked and any remaining chip-gap or CR artefacts were removed using *fixpix*, giving 1D spectra suitable for fitting using pPXF.

Figure 3-21: Example 1D spectrum from GAMA272990. The green line is extracted from the combined science file and the orange line is the equivalent after subtraction of scattered light. The upper panel shows flux calibrated spectra, and the lower panel shows the same spectra normalised to the spectrum before scattered light subtraction, i.e. to the upper panel green line. The vertical offset clearly shows the effect of removal of scattered light flux.

Table 3-4: Pixel locations for interpolation of sky-line residues

Artefact	Lower pixel number	Upper pixel number
Sky-line at 5577Å	1440	1455
Sky-line at 6300Å	2020	2030
Sky-line at 6363Å	2070	2080

4 ANALYSIS OF STELLAR KINEMATICS

This section describes the processes and tools used to analyse stellar kinematics along the major axis of the target galaxies from reduced 1D spectra. It should be noted that no attempt has been made to investigate gas phase kinematics.

4.1 Kinematics Theory

Individual stars in the target ETGs cannot be resolved, so the longslit optical spectra represent a luminosity weighted composite of light from stars in the slit. Typically, ETGs have intermediate to old age stellar populations. The old populations are dominated by red giant branch evolved stars supplemented by lower mass main sequence stars, giving spectra that are rich in molecular and metal absorption features. The spectra of intermediate age populations show Balmer series absorption features whose strength is strongly affected by the main sequence turn-off of A and F stars. Some emission features can also appear in the spectra where star formation has added young blue stars to the population. See Peletier (2012) for a review of the characteristics of stellar populations.

ETGs, particularly elliptical galaxies, are pressure supported systems, meaning that their structure is maintained by random orbits of stars around a common centre of gravity. Without these motions the spectrum of an ETG would simply be the (luminosity weighted) sum of the spectra of its stellar population. However, the motions of the stars superimposes an individual Doppler shift on each of their spectra resulting in broadening of absorption features in the galaxy's spectrum (Cappellari and Emsellem, 2004; Cappellari, 2017). In addition, for many ETGs rotation can be superimposed on the random orbits of the stars. Visualised against the plane of the sky the combination of random and rotational motions results in a line-of-sight velocity dispersion (LOSVD). The galaxies' optical spectra can therefore be treated as a convolution of their luminosity weighted spectra and the LOSVD (Cappellari and Emsellem, 2004).

The method adopted to extract velocity (V) and LOSVD uses the pPXF software package to fit pre-existing SSP templates to absorption features in the observed optical spectra using the Penalized Pixel Fitting method (Cappellari and Emsellem, 2004; Cappellari, 2017). pPXF enables the template spectra resolution to be matched to the science spectra resolution, convolution with a function representing LOSVD and adjustment for redshift, as described by Equation 11 from Cappellari (2017). The V and LOSVD components are then determined by iterative fitting of template spectra to the science spectrum in pixel space using constrained non-linear χ^2 minimization.

4.2 Implementation of pPXF for Kinematics Analysis

This project used version 7.4.0 (Cappellari, 2020) of the pPXF package[15] running on Python version 3.8.3. pPXF consists of two components –

- a core pPXF Python script which performs the fitting and produces results. This script is run as provided. Installation of the core pPXF package was tested by successfully running the 'ppxf_example_kinematics_sauron.py' script.
- a user editable Python script which creates input files, defines fitting parameters and calls the core Python script.

The SAURON usage example was chosen from the example input scripts available from Cappellari (2020), as it was closest to the requirements for this project. Major modifications to the SAURON usage example are listed below –

- implementation of a loop to process all apertures for a target galaxy in one run
- sending results to a report which could be parsed to a data table and plotted
- implementation of a pixel-based noise estimate, rather than using a single, average noise value across the entire spectrum. A noise spectrum was created for each aperture by taking the square root of its variance file, see Section 3.13.1
- implementation of time and date stamps for reporting and plotting
- enhancing the goodpixels vector to suppress fitting in the chip gaps between pixels 800 to 880 and 1640 to 1720.

SSP templates used for fitting were sourced from the Medium resolution INT Library of Empirical Spectra (MILES)[16] library (Vazdekis *et al.*, 2010; Falcón-Barroso *et al.*, 2011) which contains optical spectra at a resolution of 2.50Å (FWHM). Template spectra are convolved with a Gaussian function within pPXF to match the spectral resolution of the SALT science spectra, which was measured as 4-6Å (Section 3.4).

LOSVD is well represented by a Gaussian function due to the random movements of the stars, however particularly for higher S/N ratio spectra, pPXF can expand the fitting to include higher moments of a Gauss-Hermite series to provide additional information on the shape of absorption features. By default, pPXF describes stellar kinematics using four parameters –

- V is velocity (km s^{-1})
- σ is a Gaussian standard deviation representing the LOSVD (km s^{-1}),
- h_3 is skew, which measures deviation from symmetry i.e. the lean of the function

[15] Available at: https://www-astro.physics.ox.ac.uk/~mxc/software/#ppxf
[16] Version 11 of the MILES library is available from: ftp://ftp.iac.es/MILES

- h_4 is kurtosis which measures symmetric departure from Gaussian i.e. the flatness of the function

Each run of pPXF produces a report of these four parameters, their systematic uncertainties and a visual representation of the fit between the observed spectrum and the template library. An example is given in Figure 4-1.

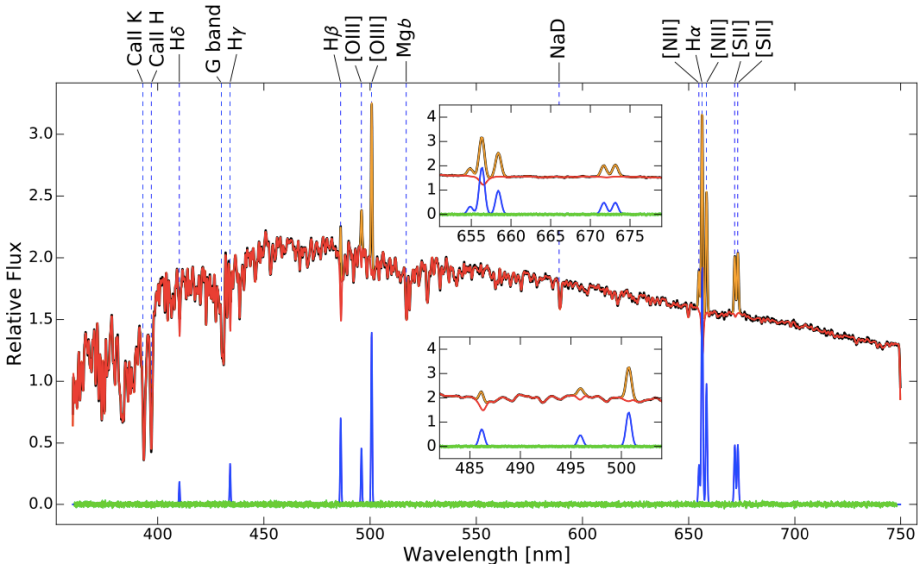

Figure 4-1: Example output from pPXF. The black line shows the observed spectrum. The red line, which closely overlays the black line, shows the pPXF fit of the observed spectrum with the template library. The orange line is the fit to emission lines. The green line shows residuals and the blue line the fit to emission features. Image credit: Cappellari, (2017).

4.2.1 Selection of SSP Library

The SSP libraries were downloaded from version 11.0 of the MILES stellar population synthesis model predictions[17], and were based on either BASTI or Padova isochrones and either Bimodal (Vazdekis *et al.*, 1996, 2015) or Chabrier (Chabrier, 2003) IMFs. The libraries were compared by calling pPXF using each library in turn to determine V and LOSVD of a set of 1D spectra from GAMA422436 and plotting these vs. spatial position as shown in Figure 4-2. The plots indicate that similar results for V and LOSVD were obtained from all SSP libraries tested. This result aligns with the results of Baldwin *et al.* (2018) who showed that, for optical spectra, there is agreement in stellar population fitting results from the MILES and ELODIE[18] stellar libraries.

All SSP libraries tested are suitable for use across the optical wavelength range, with metallicities and ages expected in ETGs. Because of its wide ranges for age and metallicity ([M/H]), see Table 4-1, the MILES SSP library of BASTI isochrones and

[17] Available at: http://research.iac.es/proyecto/miles/pages/ssp-models.php
[18] Available at – ftp://cdsarc.u-strasbg.fr/pub/cats/J/A+A/369/1048/ll/

Chabrier IMF with baseFe was selected (baseFe indicates that the library follows the abundance pattern of the Galaxy). Investigation of the effects of α-element enhancement was not within the scope of this MSc project and is an item for future work.

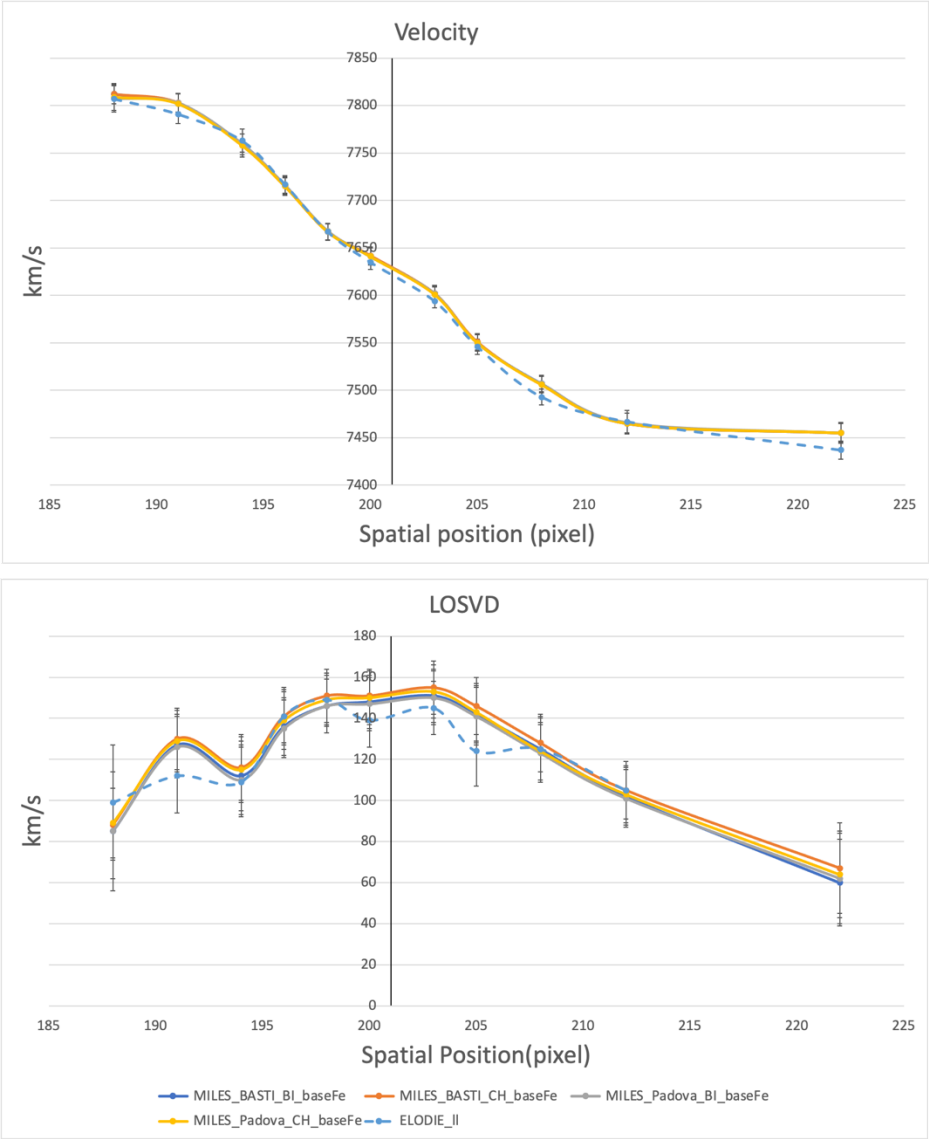

Figure 4-2: Plots of V and LOSVD determined using pPXF fitting for GAMA422436 1D spectra using different SSPs (solid lines). The fit was also tested using the ELODIE library (dashed line) for comparison. The plots show that all MILES and ELODIE libraries give similar results within their sigma errors.

Table 4-1: Age and metallicity ranges for the selected MILES SSP library.

	Number	**Range**	**log Range**
Age	53	0.03 to 14 Gyr	7.477 to 10.146
Metallicity [Z/H]	12	-2.27 to 0.40 dex	

4.3 Determination of Stellar Kinematics

pPXF was used with the tested input script and selected MILES SSP library to determine V, LOSVD, h_3 and h_4 and their formal errors for each binned 1D spectrum, both including scattered light and with scattered light removed. pPXF requires an initial estimate of LOSVD and experimentation showed that a value of 140 km s^{-1} was a good initial estimate for all target galaxies. For all kinematic determinations, emission line features in the science spectra were masked using the pPXF *goodpixels* keyword, which accesses a list of emission line wavelengths within the ppxf_util.py script. Edge effects at extreme ends of the science spectra, as shown in Figure 3-21, were excluded by setting the lower wavelength limit (lmin) to 3800Å and upper wavelength limit (lmax) to 6800Å.

pPXF produces a plot of the fit for each aperture, with a typical example shown in Figure 4-3. When compared with Figure 4-1, the left panel of Figure 4-3 shows a poorer overall fit, seen in deviations of the red line from the black line and a wave-like pattern in the green residuals, rather than the expected gaussian distribution of residuals around the zero line. Poorer fitting and the pattern in the residuals can be seen in plots for all apertures of all target galaxies and for both science spectra and science spectra from which scattered light had been removed.

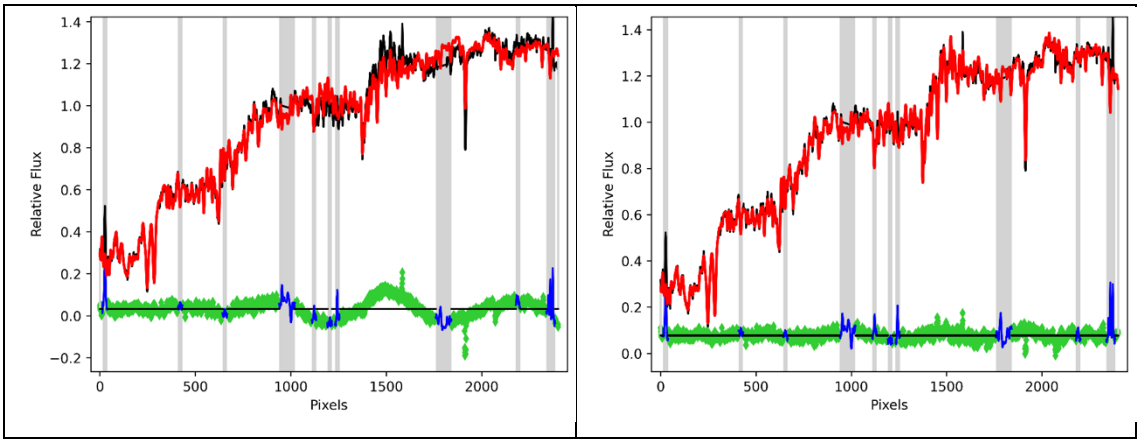

Figure 4-3: Examples of typical pPXF output plots of relative flux vs dispersion in log rebinned pixels. The colour key is as described in Figure 4-1. The left panel shows fitting with degree = 4 which results in the wave structure in the residuals. The right panel shows fitting with degree = 4 and mdegree = 12, giving a much closer correspondence between observed and fitted spectra. See below for definition of degree and mdegree.

To confirm if the pattern in the residuals was linked to the library, observed spectra or data reduction, test fittings were performed using GAMA422436 apertures with MILES SSPs at different isochrones, IMFs and α-element enhancements. These showed that the pattern is present whichever MILES SSP library is used for the fitting. Additionally, to confirm if the pattern was specific to MILES library spectra the fitting was repeated for

the GAMA422436 apertures using the ELODIE library. Residuals for all apertures fitted using the ELODIE library show a similar pattern to that in Figure 4-3, and results for V, LOSVD, h_3 and h_4 were similar using MILES and ELODIE libraries, as expected from Figure 4-2. This indicates that the artefact originates in the continuum shape of the observed spectra and not the template library. The continuum shape is affected by some data reduction steps e.g. flat fielding and flux calibration. Investigation of the illumination flats, produced in Section 3.1, showed that all flats had a variation of ~5% in their continuum shape in the dispersion direction on the blue and central CCD panels. This could produce the mismatch between flat corrected science spectra and library SSP templates leading to the pattern in pPXF fitting residuals seen in the left panel of Figure 4-3. This is addressed by using higher order polynomials for pPXF fitting, as discussed below.

pPXF fitting parameters were tested as follows –

- moments – this parameter sets the order of Hermite moments used for fitting. For all apertures of all target galaxies, with and without scattered light removal, values of h3 and h4 were approaching zero, whichever library was used for the fitting. This indicates that the shape of absorption features in the science spectra was a good approximation to Gaussian. Therefore, test fittings were performed with moments = 2 to fit only V and LOSVD, and not the higher order Hermite moments. These tests showed no significant change to V or LOSVD, no significant change to the shape of the V and LOSVD plots, and a negligible reduction in formal error values for V and LOSVD. As moments = 2 gave only a minimal reduction in fitting time the default of moments = 4 was adopted to provide ongoing confirmation of the Gaussian shape of the spectral features.
- bias – this parameter biases the fit towards Gaussian i.e. biases values of the higher order Hermite moments towards 0. A bias level can be calculated using the method of (Vudragović, Samurović and Jovanović, 2016), which suggests a bias of 0.3 for a S/N ratio of 30. Testing at bias values of between 0 and 1 showed no significant impact on fitting results or reduced χ^2 values, as expected given that values of h_3 and h_4 were already approaching zero. The default value of bias=None was adopted for kinematics analysis.
- degree – this is the order of additive polynomial used in fitting, with a default value of 4. Testing at values of 2, 4 and 8 showed no significant impact on fitting results or artefact in the residuals, however a value of 16 flattened the artefact to

give a visually improved fit, similar to that shown in the plot in the right panel of Figure 4-3.

- mdegree – this is the order of an optional multiplicative polynomial which can be added to improve fitting of library SSPs to the continuum shape of the target spectrum. Testing at values of 2, 4 and 8 showed no significant impact on the artefact in the residuals, however values of 12 and 16 provided a visually improved fit, as seen in the right panel of Figure 4-3. Cappellari (2017) indicates that additive polynomials are used to change the strength of individual absorption lines to minimise mismatches between the templates and spectrum under test and to correct for imperfect sky background subtraction, while multiplicative polynomials correct for inaccuracies in flux calibration of the spectrum under test. Based on the visual improvements to fitting, shown in Figure 4-4 and the recommendations from Cappellari (2017), both the recommended additive polynomial and the optional multiplicative polynomial are required in kinematics analysis for this project.

The quality of fitting was tested using the reduced χ^2 statistic[19] as a measure of goodness of fit, where–

$$\chi^2_R = \frac{\chi^2}{DOF} \qquad \text{Equation 4-1}$$

Where –

χ^2_R = reduced chi squared
DOF = degrees of freedom = sample size - number of parameters to be fitted
χ^2 = chi squared = variance weighted sum of the squared deviations –

$$\chi^2 = \sum_i \frac{(O_i - C_i)^2}{{s_i}^2} \qquad \text{Equation 4-2}$$

Where –

O_i = values of observations
C_i = values of library spectra being fitted
s_i^2 = variance of observations
i = sequential counter from 1 to maximum number of observations

Reduced χ^2 should be close to 1 for the model to be valid i.e. for the fit of library spectra to the observed spectrum to be considered good. Reduced χ^2 values >>1 indicate a poor fit and values <<1 indicate that library spectra are over-fitting the observed spectrum, usually because noise has been over estimated. Values for reduced χ^2 calculated by pPXF were tested by extracting the pPXF pp.bestfit vector and performing the calculation manually. Table 4-2 gives reduced χ^2 values obtained using different

[19] See, https://ned.ipac.caltech.edu/level5/Wall2/Wal3_4.html

orders of pPXF fitting polynomials. The reduced χ^2 is significantly improved by including a multiplicative polynomial, confirming the conclusions from visual examination, shown in Figure 4-4. Cappellari (2017) recommends always including an additive polynomial in kinematics analysis and therefore values of degree = 4 with an optional mdegree = 12 were adopted.

Figure 4-4: The top panel shows a plot of normalised flux vs wavelength for an example spectrum (black) overlayed with the pPXF fit obtained using different polynomial orders. The lower panel shows the residuals from the fit, i.e. example spectrum - fitted spectrum. The plots show the improvement in fit obtained by including a multiplicative polynomial order = 12.

Table 4-2: Example of reduced χ^2 values obtained using different orders of pPXF fitting polynomials when fitting a spectrum from GAMA422436.

Fitting parameters	Reduced χ2
degree 4, mdegree 0	2.36
degree 4, mdegree 12	1.35
degree 4, mdegree 16	1.31
degree 4, mdegree 0	2.36
degree 12, mdegree 0	1.72
degree 16, mdegree 0	1.51

The pPXF input script was configured to report results for V, LOSVD, h_3 and h_4, and their formal errors. V and LOSVD were plotted vs. spatial position to provide an indication of behaviour of the major-axis kinematics of the target galaxy and plots for each target galaxy are presented in Section 6.2. Results show physically realistic values for V and LOSVD, and the plots show physically realistic shapes for profiles of V and LOSVD vs. spatial position, when compared with published results for ETGs e.g. Katkov, Kniazev and Sil'chenko (2015) and Kuntschner *et al.* (2010). The plots also show a reduction in LOSVD after removal of scattered light as predicted by Katkov *et al.* (2019).

5 ANALYSIS OF STELLAR POPULATIONS

This section describes the processes and tools used to extract data on stellar populations along the major axis of the target galaxies from spatially binned 1D spectra by full spectral fitting (Cappellari, 2017). The strategy adopted was to use a high-order multiplicative polynomial to fit the continuum, allowing the fit to be based on strengths of the absorption features. The alternative strategy of including information from the continuum shape was not practical given the relative flux calibration of spectra from SALT and the dusty nature of the target galaxies.

The analysis used the same pPXF implementation, and library of MILES SSP templates, previously used for determination of stellar kinematics. For analysis of stellar populations pPXF fits a combination of SSP templates, covering the range of ages and metallicities in the template library, to the spectrum under test and generates a solution containing a mass weighted age and metallicity. Each run of pPXF also generates values for kinematic parameters V, LOSVD, h_3 and h_4, which allows comparison with V and LOSVD results from kinematics analysis. Analysis of stellar kinematics showed the effects of scattered light, therefore, analysis of stellar populations was performed only on 1D spectra from which scattered light had been removed.

For each target galaxy analysis of stellar populations took place in two phases –

1. Using the method described in Section 3.14 a single central aperture extending to $R_e/8$, (see Table 2-2), was extracted from each target galaxy. This aperture was analysed using the pPXF stellar population script to produce values for mass weighted average central age and metallicity.
2. For targets with a sufficiently high S/N ratio the binned apertures previously used for analysis of kinematics were re-analysed using the pPXF stellar population script. This produced profiles for age and metallicity and profiles for V and LOSVD which could be compared with the kinematics results, see Figure 6-7.

pPXF output plots and spatial profiles are presented and discussed in Section 6.

5.1 Implementation of pPXF for Analysis of Stellar Populations

As for analysis of stellar kinematics, use of pPXF for analysis of stellar populations requires a tailored input script and the ‘population_gas_SDSS.py’ usage example was chosen as a starting point from the selection of input script examples available from Cappellari (2020). This script was closest to the requirements for this project, but required the following major modifications –

- implementation of fixed noise per pixel, based on a S/N ratio generated for each aperture by BINBATCH, see Section 3.14.1.
- implementation of log binning for the input SALT science spectra, as SDSS spectra on which the example is based are already log binned.
- implementation of a loop to process all apertures for a target galaxy in one run.
- sending results to a file which could be parsed to a data table and plotted.
- implementation of time and date stamps for reporting and plotting.

The input script was configured to report fitting results for V, LOSVD, h_3 and h_4, together with a mass weighted average age and metallicity for the stellar population. The V and LOSVD results from stellar populations fittings were very similar to the previous results from fitting only the stellar kinematics, see Section 4.3. Therefore, any future analysis could use the stellar populations script for determination of V and LOSVD, however, for this project both scripts were used to provide an ongoing check.

pPXF also generated a plot of best fit of templates to the science spectrum, similar to the plot from kinematics fitting shown in Figure 4-1, and an accompanying grid of metallicity vs. log age, with mass fraction shown by colour intensity, see Figure 5-1 for an example.

5.2 Optimisation of the Fitting Parameters

pPXF determines stellar population age and metallicity by fitting a weighted combination of template spectra to the science spectrum under assessment. The selected MILES library contains 53 ages and 12 metallicities, which delivers a grid of 636 points. SALT spectra were fitted between 3800 and 6800Å and fitting was controlled by the following parameters set within the input script –

- moments – the default value of moments=4 was adopted.
- degree – Cappellari (2017) recommends only using multiplicative polynomials for analysis of stellar populations, to avoid affecting the line strengths of spectral features. Therefore, additive polynomials were excluded by setting degree = -1.
- mdegree – Cappellari recommends a value of mdegree=10 for stellar populations analysis, in the help text within the ppxf_example_population_gas_sdss.py script. This value has been found by Baldwin *et al.* (2018) enable a good fit of the continuum for ATLAS^{3D} spectra, without fitting the absorption features. Testing at mdegree=10 showed a recurrence of the mild wave pattern in the residuals, previously discussed in Section 4.3. While the wave pattern was suppressed by

using a higher order polynomial e.g. mdegree=16, reduced χ^2 was not significantly improved, therefore, a value of mdegree=10 was adopted.

- regul – as seen in the upper panel of Figure 5-1, pPXF produces a best fit i.e. with minimum χ^2, when un-regularized (see Cappellari (2017) Section 3.5). However, this solution is unlikely to be physically realistic as it is focused on a few grid elements, implying a stellar population with discrete age and metallicity components. A more physically realistic solution is produced by including regularisation which applies a penalty to χ^2 and biases the solution to increase the number of incorporated SSP templates, resulting in smoother age and metallicity outputs. This is illustrated in the lower panel of Figure 5-1. The amount of regularisation is controlled by the *regul* parameter, and the objective is to choose the minimum value for *regul* which gives a solution with delta χ^2 ($\Delta\chi^2$) = desired $\Delta\chi^2$, see Cappellari (2020), where –

$$\text{desired } \Delta\chi^2 = (2*\text{number of dispersion pixels})^{½} \qquad \text{Equation 5-1}$$

The χ^2 value calculated by pPXF is dependent on the estimate of noise in the input spectrum (Baldwin *et al.*, 2018), therefore the optimum value of *regul* needs to be determined for each input spectrum individually. The following two step iterative process from Cappellari (2020) was used to determine the most suitable values for *regul* –

1. with *regul* = 0 iterative fittings were performed using a range of input S/N ratios to determine the S/N ratio which produces a fit with χ^2/DOF as close as possible to 1.
2. using the S/N ratio from step 1, iterative fittings were performed using increasing values of *regul* until the value of $\Delta\chi^2$ reported by pPXF equals the desired $\Delta\chi^2$ value of 69.3, from Equation 5-1.

Initial fittings were performed on the central $R_e/8$ aperture from each target galaxy. The expected behaviour of $\Delta\chi^2$ with increasing regularisation is illustrated in the top panel of Figure 5-2 and was seen for GAMA227266, 422436, 546040 and 560238, with desired $\Delta\chi^2$ being achieved using *regul* values in the range 10 to 25. GAMA99687 and 227264 showed similar behaviour but required *regul* $\simeq$ 150 before $\Delta\chi^2$ approximated desired $\Delta\chi^2$. For GAMA65075, 79849, 85416, 136847, 272990, 298980, 569555, 570227 and 3576053, $\Delta\chi^2$ did not increase to equal desired $\Delta\chi^2$ even with *regul* as high as 200, as illustrated in the lower panel of Figure 5-2. This was unexpected behaviour (personal communication M. Norris 07/06/2021) which could be investigated using Monte Carlo simulations to test the effects of noise in the input spectrum. This investigation was not possible within the time available for this project and a value of *regul* = 20 was estimated

from $\Delta\chi^2$ vs. *regul* plots, e.g. Figure 5-2, as the minimum value of *regul* which gave the largest change in $\Delta\chi^2$. Resulting values of log Age and [M/H] should be taken as indicative as these fittings are under regularised. As shown in Figure 5-3, results for V and LOSVD are essentially unaffected by the amount of regularization while results for age and [M/H] reduce as regul increases. Results obtained for age and [M/H] from the central $R_e/8$ aperture, and pPXF plots for each target galaxy are presented in Section 6.3.

Based on results from fitting the central $R_e/8$ aperture, only targets which showed the expected behaviour of $\Delta\chi^2$, i.e. GAMA227266, 422436, 546040 and 560238, were taken to the second phase of fitting of individual apertures to produce spatial profiles for age and [M/H]. This was performed as a pilot study for later stellar population analysis work and results are presented in Section 6.

5.3 Estimation of Uncertainties for Stellar Populations

While pPXF reports formal uncertainties for kinematics parameters V, LOSVD, h_3 and h_4, it does not report uncertainties for age and metallicity. The main sources of uncertainties in the reported age and metallicity are –

- Observational uncertainties – primarily noise and differences in the continuum shapes discussed above.
- Inaccuracies in the assumptions used to build the SSP templates.
- Degeneracies between parameters e.g. age/metallicity.

Monte Carlo simulation methods are normally used to determine uncertainties in the reported population parameters, see Chilingarian and Grishin (2020) and Ge *et al.* (2018) for a discussion, however, due to time constraints it was not possible to develop a Monte Carlo method as part of this project. An alternative, approximate, method was adopted where uncertainties were estimated by visual examination of the pPXF age vs metallicity plots, see Section 6.3.

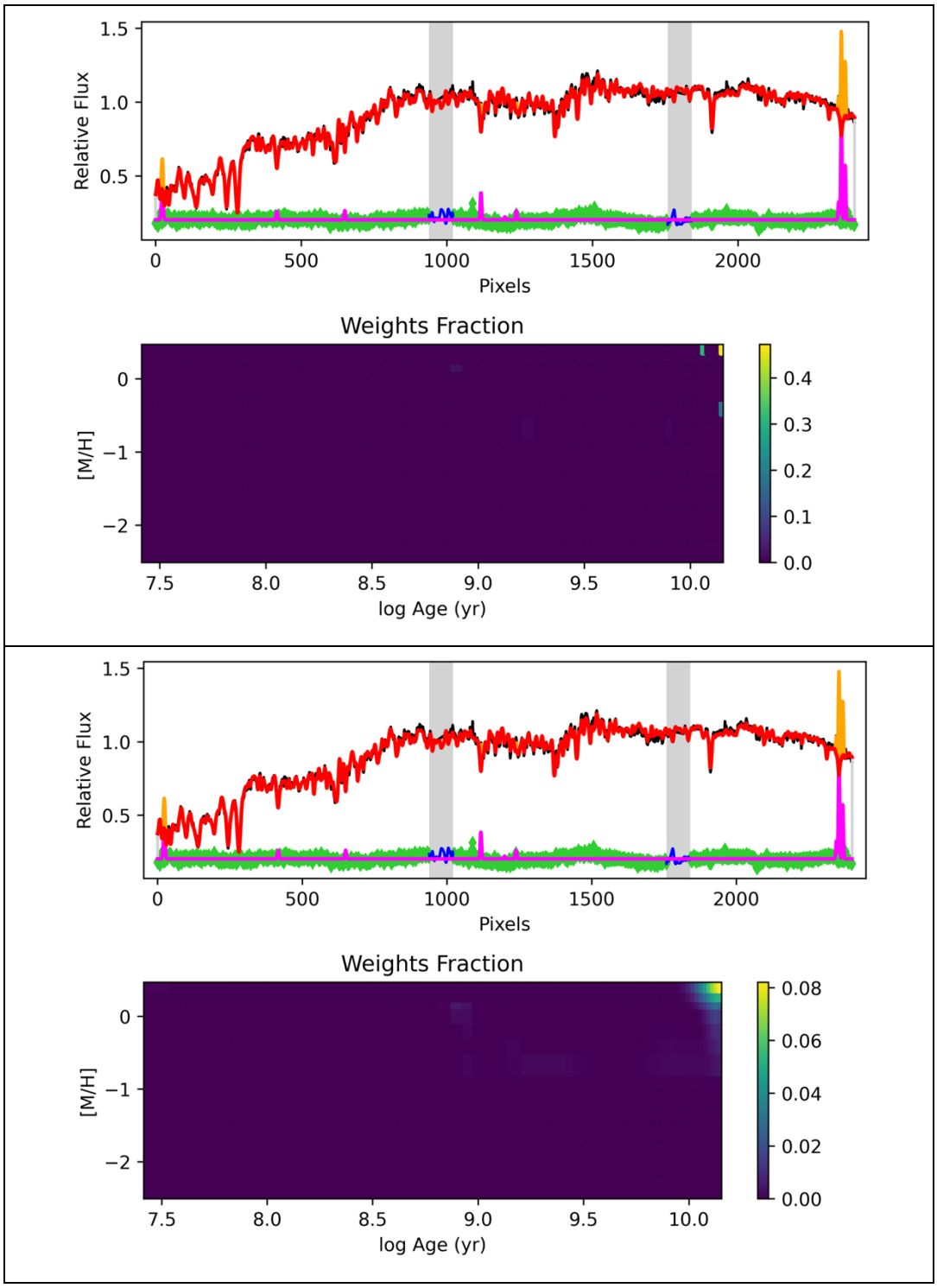

Figure 5-1: Plots showing typical pPXF outputs from analysis of stellar populations in GAMA227264. The wavelength vs. relative flux plots show masking of chip gaps and quality of the fit, previously discussed in Figure 4-1, and are visually indistinguishable between upper and lower panels. As previously, the x-axis is in log rebinned pixels, with pixel 0 ≡ 3800Å and pixel 2400 ≡ 6800Å. Grids of [M/H] vs log Age show the weights fraction at each grid point represented by colour. The upper grid shows *regul*=0 and has given a narrow distribution of ages and metallicity with several discrete points. The lower grid shows *regul*=100, which has given a smoother solution by incorporating additional templates with a wider range of ages and metallicities.

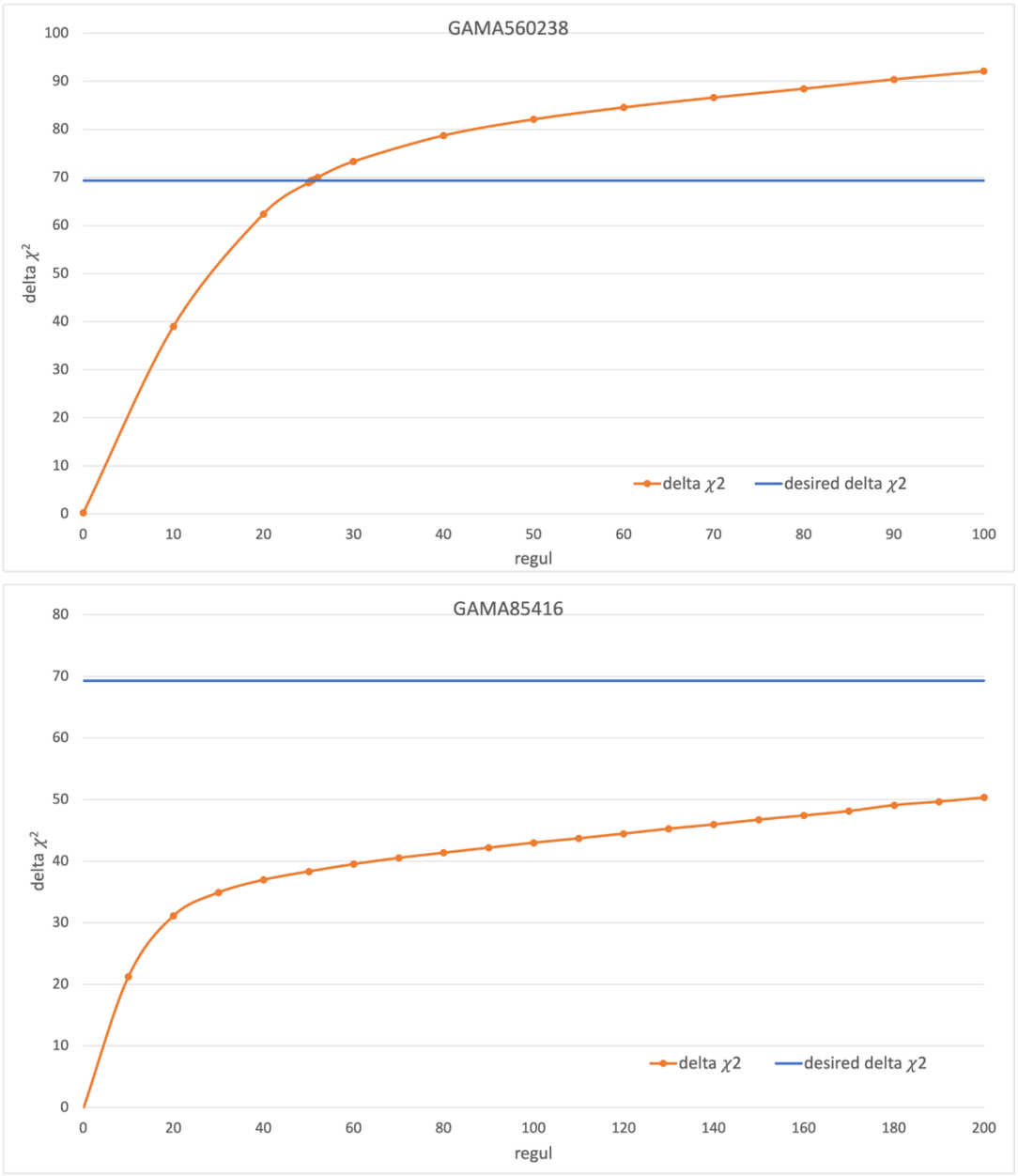

Figure 5-2: Effect of increasing regul on $\Delta\chi^2$ from fitting an example central $R_e/8$ aperture spectrum. The top panel shows an example of the expected behaviour with $\Delta\chi^2$ increasing through desired $\Delta\chi^2$. The lower panel shows an example of the alternative behaviour where $\Delta\chi^2$ does not reach desired $\Delta\chi^2$.

regul	delta chi2	V	LOSVD	log Age	Age	[M/H]
		km s^{-1}	km s^{-1}		yr	
0	-0.5	7639	144	10.143	1.390E+10	0.264
10	65.1	7639	141	10.112	1.294E+10	0.240
20	97.4	7639	141	10.112	1.294E+10	0.221
30	111.2	7639	142	10.111	1.291E+10	0.212
40	118.4	7639	143	10.109	1.285E+10	0.206
50	123.4	7639	143	10.106	1.276E+10	0.200
60	127.5	7639	142	10.104	1.271E+10	0.195
70	131.0	7639	142	10.102	1.265E+10	0.192
80	134.3	7639	142	10.100	1.259E+10	0.188
90	137.3	7639	142	10.098	1.253E+10	0.184
100	148.3	7639	141	10.096	1.247E+10	0.181

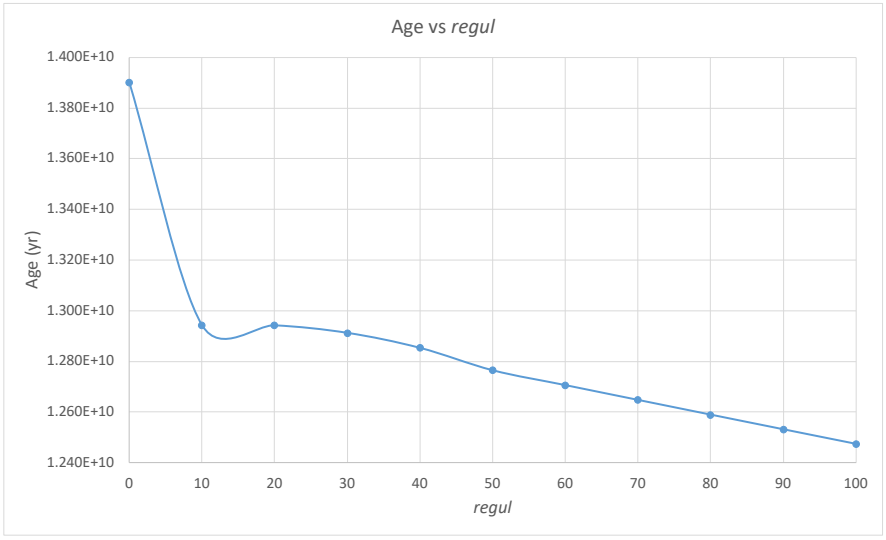

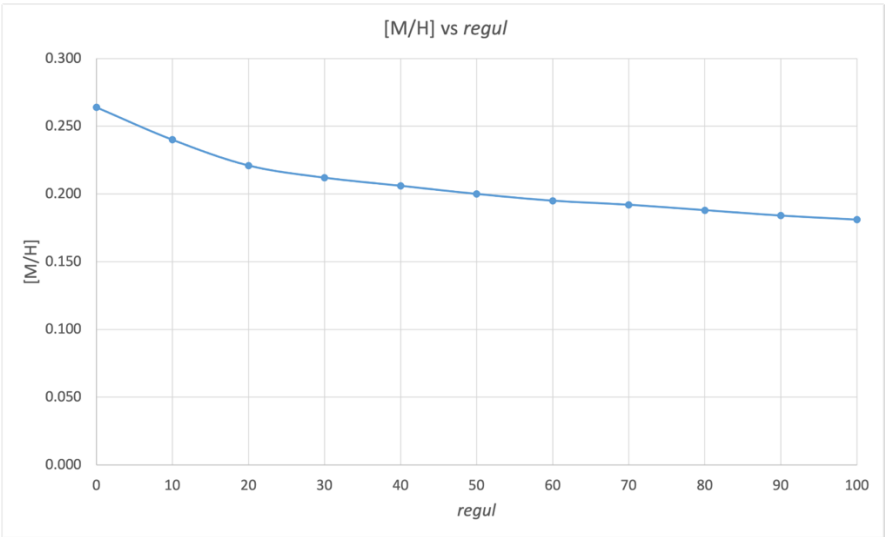

Figure 5-3: The top panel shows results from fitting the central $R_e/8$ aperture of GAMA422436 using increasing values of *regul*. While results for V and LOSVD are unaffected by regularisation, results for age and [M/H] decrease as regularisation increases. The lower panels show the trend in age and [M/H].

6 RESULTS

The results obtained are presented and discussed in this Section and comments are given on the techniques and methods used. Results for individual ETGs are presented and discussed in Section 7.

6.1 Data Reduction and Spectroscopy

Data reduction proceeded as expected, however, the reduced spectra generally had a lower S/N ratio than the target of 30 set in the SALT PIPT. SALT indicates that S/N ratio based exposure times are often underestimated when using the RSS Simulator (SALT Ast Ops, 2020), and it is likely that additional exposure time would be required to achieve the expected S/N ratio for all targets. This excludes GAMA78425 where existing observations were affected by cloud and appear unusable.

All target galaxies display spectral features typical of ETGs, with absorption features for Na, Mg, Fraunhofer G, H and K bands, and a 4000Å break, indicating that the areas sampled are dominated by intermediate/old age stellar populations. The 4000Å break is ratio of flux at 4050 - 4250Å to flux at 3750 - 3950Å and is a key age indicating feature caused by absorption due to metals in the atmospheres of intermediate to old age stars and a lack of hot, blue stars in older stellar populations. Some targets show emission features of [OIII] and for lower redshift targets emission features of [NII] (doublet), Hα and [SII] (doublet). The Hβ line can be identified either in emission or absorption, however higher order Balmer lines e.g. Hγ, Hδ etc. are difficult to identify by visual inspection.

A list of key spectral features and their wavelengths is presented in Table 6-1. Two typical 1D spectra are presented in Figure 6-1 and a summary of spectral features visually identified in the central aperture 1D spectrum of each target galaxy is presented in Table 6-2. A redshift corrected spectrum was created for each target ETG using IRAF *dopcor* and the redshift value from Table 2-2. These are presented in Appendix B.

For each target the 1D spectrum from the central aperture was compared with the GAMA catalogue spectrum and a good visual match was found for presence and strength of the main absorption and emission features. However, this comparison again showed differences in the mid-spectrum continuum shape in the 4700 - 5700Å region, as previously discussed in Section 4.3. These shape differences should not affect downstream analysis as high order polynomials were used to fit the continuum shape for analysis of stellar kinematics (mdegree = 12) and stellar populations (mdegree = 10).

Table 6-1: Rest wavelengths in air of key optical spectral features for ETGs.

Absorption	Wavelength (Å)
Ca (K)	3933.7
Ca (H)	3968.5
G-band (CN)	4304.4
Mg I b (triplet)	5167.3, 5172.7 & 5183.6
Fe II	5270, 5335 [1]
Na I D (doublet)	5890.0 & 5895.9
TiO	6180

Emission	Wavelength (Å)
[OII]	3727.3
Hδ	4102.8
Hγ	4340.0
Hβ	4861.4
[OIII] doublet	4958.9 & 5006.8
[NII] doublet	6548.0 & 6585.2
Hα	6562.8
[SII] doublet	6716.4 & 6732.7

Sky	Wavelength (Å)
[OIII]	5577.3
[OI]	6303.0
[OI]	6365.3

Table 6-1 Notes –
[1] there are many Fe absorption features in optical spectra, these two are given as examples.

Section 7.7 of the SALT Call for Proposals (SALT Ast Ops, 2020) indicates that the issue of stray light causing a decrease in S/N ratio of observations of faint targets was resolved in 2015, however Katkov *et al.* (2019) found sufficient scattered light to affect measurement of LOSVD. Therefore, the process for scattered light removal developed by Katkov et al., and accompanying Python scripts, were used to remove scattered light from the 2D spectra. Scattered light was successfully removed, as indicated by the reduction in LOSVD in spectra with scattered light removed. However, the majority of SALT standard star spectra, used to model spatial profiles of scattered light, produced asymmetric profiles which were not physically feasible. For this project there were sufficient symmetric profiles to choose from, assuming that the scattered light profile changes slowly with time e.g. due to a build-up of dust in the instrument optics, and further investigation is recommended, see Section 7.2, to explain the root cause of the asymmetric profiles.

As discussed in Section 3.4.1 spectral resolution varies from ~5.5Å at the blue end to ~4.5Å at the red end of the spectrum, giving a mid-spectrum FWHM instrument dispersion of ~119 km s^{-1} using Equation 2-1. A mid-spectrum resolution of ~5Å is lower than 3.8Å predicted by the RSS simulator and ~3Å quoted by Vaghmare *et al.* (2018) for an identical SALT configuration. While the root cause of lower spectral resolutions is not understood, LOSVDs for the target ETGs are in the approximate range 120–200 km s^{-1}, see Section 6.2, and the spectra remain suitable for full spectral fitting using pPXF. See Cappellari (2017) for a discussion of using full spectral fitting where velocity dispersion is similar to the instrument dispersion.

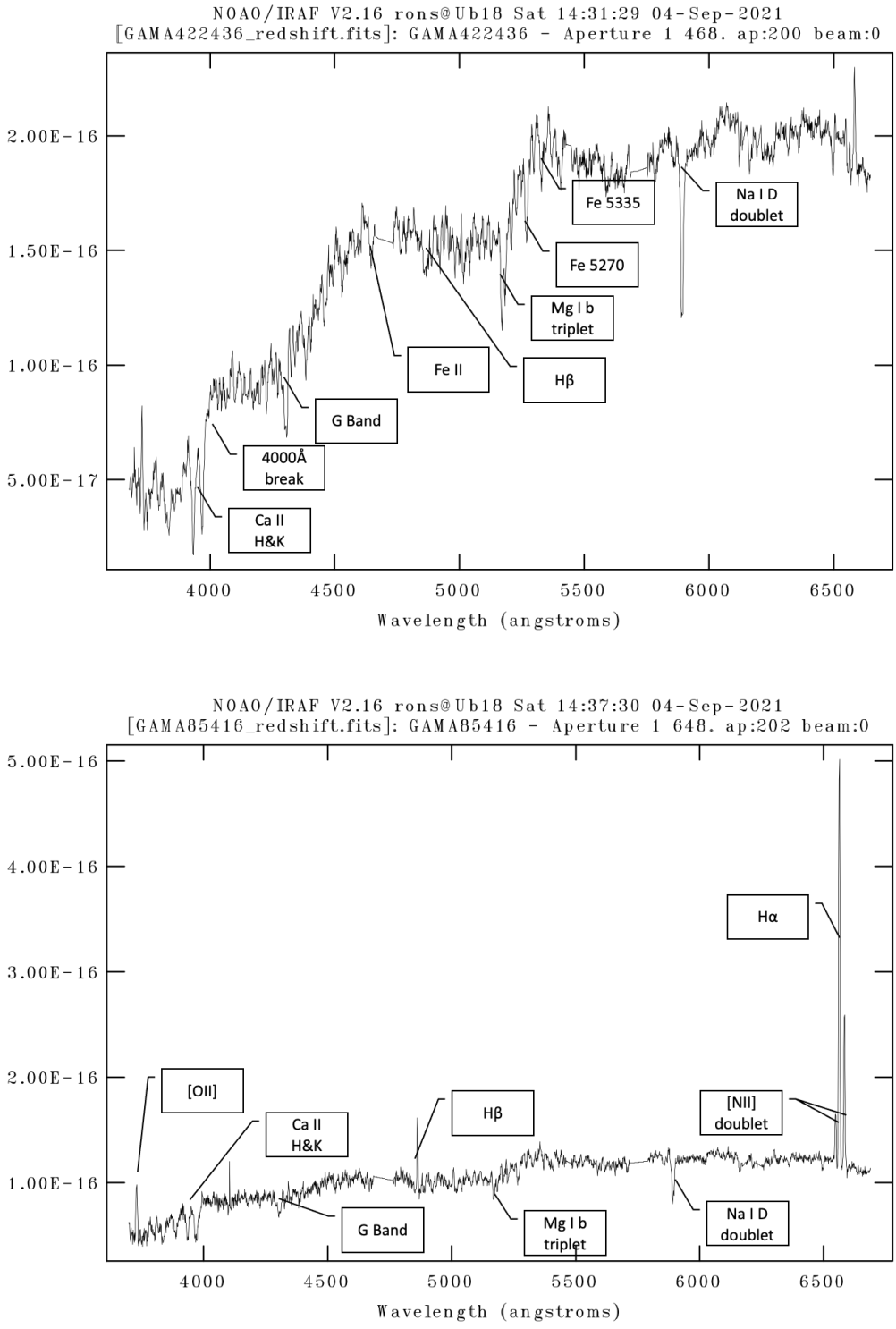

Figure 6-1: Example 1D spectra from the central aperture of two target ETGs with key emission and absorption features marked. The upper panel is the spectrum of GAMA422436 showing strong absorption features typical of an older stellar population. The lower panel is the spectrum of GAMA85416 showing strong absorption features but with the addition of emission features of H, N and O indicating the possible presence of a younger stellar population component. Vertical scale is ergs/s/cm^2/Å but is not an absolute flux calibration due to the SALT variable pupil. Rest wavelength of the features is given in Table 6-1.

Table 6-2: Qualitative summary of absorption and emission features based on visual inspection of the central aperture 1D spectra.

Galaxy GAMA	4000A Break	Absorption Features				Emission Features			Balmer [1]	
		H & K	G	Mg	Na	[OII]	[OIII]	[NII]	Hα	Hβ
67075	+	+	+	+	+	×	-	-	Em	Ab
78425	-	+	+	+	+	+	+	→	→	Em +
79849	+	+	+	+	+	-	×	→	→	Ab
85416	-	+	+	+	+	-	×	+	Em +	Em # +
99687	+	+	+	+	+	-	×	→	→	Ab
136847	+	+	+	+	+	-	-	-	Em -	Ab
227264	+	+	+	+	+	-	×	-	Em	Ab
227266	+	+	+	+	+	-	×	-	Em	Ab
272990	+	+	+	+	+	-	×	→	→	Ab +
298980	+	+	+	+	+	+	-	+	Em +	Em # +
422436	-	+	+	+	+	+	×	-	Em -	Ab -
546040	+	+	+	+	+	+	×	-	Em -	Ab -
560238	+	+	+	+	+	+	×	-	Em -	Ab -
569555	-	+	+	+	+	-	+	→	→	Em # +
570227	+	+	+	+	+	-	×	-	Em -	Ab +
3576053	+	+	+	+	+	×	×	→	→	Ab

Notes :
Em = feature is present in emission. Ab = feature is present in absorption. # = absorption wings visible at base of the Hβ emission feature.
- = feature is weak. + = feature is strong. × = feature is not visible. → = feature is beyond the red wavelength limit.
[1] only Hα and Hβ Balmer lines are listed as higher order Balmer lines are difficult to identify reliably by visual inspection

6.2 Stellar Kinematics

Spatial profiles of V and LOSVD from pPXF are presented as plots in Figure 6-2 and a summary of kinematic results is presented in Table 6-3. Results for h_3 and h_4 are not presented as their values were approaching zero and were less than their reported errors for all fits, confirming that V and LOSVD were well modelled by Gaussian functions. The kinematic profiles presented in Figure 6-2 show rotational velocity (V_{Rot}), which is recession velocity minus central recession velocity, and show that the SALT spectra had a sufficiently high S/N ratio for stellar kinematic analysis only within R_e. The plots also show that velocity profiles do not extend spatially to the point where velocity reaches V_{max}, except possibly for GAMA422436 where rotational velocity may be flattening in the outer apertures. This also applies to velocity profiles obtained from lower S/N ratio apertures.

For targets with data recoverable at S/N ratio ≥20 the majority of reduced χ^2 values were in the range 0.7 to 2 vs. a target value of 1, indicating a satisfactory fit of template spectra to science spectra. Where kinematic results were obtained at a S/N ratio >20 the overall shape of the velocity and LOSVD spatial profiles was confirmed by repeating the analysis at S/N ratio = 20. Five spatial bins or spread of spatial bins across both sides of the centre line, could not be obtained for GAMA 569555, 570227 and 3576053 even at S/N ratio = 20. For these targets pPXF fitting was attempted using spatial bins extracted at S/N ratio = 15, however, while this provides an indication of overall shape of the V and LOSVD profiles, the results were not quantitatively meaningful due to their large uncertainties. Due to its low S/N ratio no fittings were performed for GAMA78425.

Stellar kinematics profiles, presented in Figure 6-2, confirm the assertation of Katkov *et al.* (2019) on the effects of scattered light, seen from behaviour of the blue profile (scattered light not removed) vs. green profile (scattered light removed). Rotational velocity appears largely unaffected by scattered light, within the uncertainty estimates. LOSVD values are generally lower in profiles with scattered light removed. Most targets show reduction of LOSVD with increasing radius, as expected from the results of SAURON and ATLAS^{3D}. However, there are several anomalous results which suggest disturbed kinematics or kinematic sub-structures –

- GAMA65075 shows dips and peaks in the LOSVD profile, suggesting disturbed stellar kinematics relatively close to the centre line.
- GAMA85416 shows an asymmetric LOSVD profile.

- GAMA272990 shows asymmetric LOSVD, possibly with LOSVD increasing with radius.
- GAMA546040 has a dip in LOSVD at ~+2 arcsec from the centre line, but within the uncertainties.
- GAMA560238 shows a relatively flat LOSVD profile within ~3 arcsec of the centre line, outside this LOSVD appears to increase with radius. These suggest disturbed stellar kinematics in this galaxy.
- GAMA569555 shows LOSVD values for the scattered light removed profile to be greater than those for the profile containing scattered light, albeit within high uncertainties.
- GAMA3576053 shows single sided profiles for velocity and LOSVD. BINBATCH failed to select data for apertures >201 even at a S/N ratio of 15. To verify the V and LOSVD profiles, apertures were manually selected at pixel values on both sides of the centre line at S/N ratio ~20. Kinematic results from these show relatively symmetric profiles on both sides of the centre line with LOSVD decreasing and rotational velocity increasing with distance from the centre. This suggests that there is an aperture close to spatial row 202 which caused an issue in the BINBATCH code.

Of these only GAMA560238 has an identifiable source of polluting light in the sampled area, as discussed in Section 7.1.

The relative positions of the blue and green profiles in Figure 6-2 confirms that scattered light is broadening the absorption features, and its removal is recommended for any future stellar kinematics analysis based on SALT/RSS spectra. Future work will require an improved understanding of the process for determination of the scattered light profile from SALT standard star spectra. The kinematics profiles also show that the lower-than-expected S/N ratio limited spatial sampling essentially to within R_e. Therefore, profiles presented in Figure 6-2 cover only the bulge and inner part of the disc of the S0-Sa galaxies in the sample and do not extend to the outer disc. Generally, LOSVD reduces with radius and LOSVD uncertainties generally increase with radius. Increasing uncertainties is an expected effect of the S/N ratio based apertures becoming more spatially extended as radius increases, due to reducing flux with increasing distance from the peak of the trace.

Results for LOSVD from fitting central $R_e/8$ apertures, presented in Table 6-3, show close agreement to LOSVD results for the galaxy centres presented in Figure 6-2, confirming the results for the central kinematics. The 89 to 203 km s^{-1} range of LOSVD

for the central areas, given in Table 6-3, matches the results of 82 to 191 km s^{-1} obtained using SALT longslit spectra for the central area of seven nearby ETGs by Katkov, Kniazev and Sil'chenko (2015).

ETGs are supported by a balance of gravitational and kinetic energies, with the kinetic component being distributed between rotation (ordered motion) and velocity dispersion (random motion) (Ferreras, 2019). Rotation causes flattening of the system, with the amount of flattening depending on the balance of rotational vs. dispersion support, which can be represented by V_{max}/LOSVD. Apparent flattening is indicated by ellipticity (ε), which is defined as –

$$\varepsilon = \left(1 - \frac{b}{a}\right) \qquad \text{Equation 6-1}$$

Where – a = semi-major axis length and b = semi-minor axis length.

Flattening can also be caused by anisotropy in velocity dispersion. As anisotropy increases, the orbits of stars elongate in the direction of larger velocity dispersion, causing flattening i.e. increasing anisotropy gives increasing ε. ETGs without rotation, i.e. where V_{max}/LOSVD tends to 0, and with isotropic velocity dispersions will not be flattened. Flattening of isotropic ETGs by rotation alone is shown by the oblate spheroid line in Figure 6-3, which is derived from the approximation by Kormendy (Kormendy and Kennicutt Jr, 2004) given in Equation 6-2, and which is accurate to 1% for $0 \leqq \varepsilon \leqq 0.95$.

$$\frac{V_{max}}{LOSVD} \approx \sqrt{\frac{\varepsilon}{1-\varepsilon}} \qquad \text{Equation 6-2}$$

As the velocity profiles do not extend spatially to the point where velocity reaches V_{max}, maximum measured rotational velocity was used as the lower limit for V_{max}, shown in Table 6-3. Therefore, the plot of V_{max}/LOSVD vs. ε in Figure 6-3 is based on the lower limit of V_{max}. Figure 6-3 indicates that there is significant rotational support for all targets, with most lying close to the line of rotationally supported oblate spheroids. The result for GAMA85416 appears anomalous as it is morphologically classified as Elliptical but has the highest level of rotational support while other elliptical galaxies in the sample sit towards lower left of the plot. This is discussed further in Section 7.1.4. The V_{max}/LOSVD vs ε format is used rather than the more recent and robust (less inclination dependent) λ_R vs. ε format (Emsellem *et al.*, 2007), as the latter is based on integral field observations.

Use of a pixel by pixel noise input, based on the sigma spectrum, delivered acceptable results but was probably an unnecessary complication as later experimentation using an average noise value gave similar results.

Figure 6-2: Plots of Rotational Velocity (V_{Rot}) and LOSVD vs. spatial position along the major axis. Vertical orange lines show the spatial centre, $R_e/8$ and R_e. The S/N ratio limits stellar kinematic analysis to within R_e.

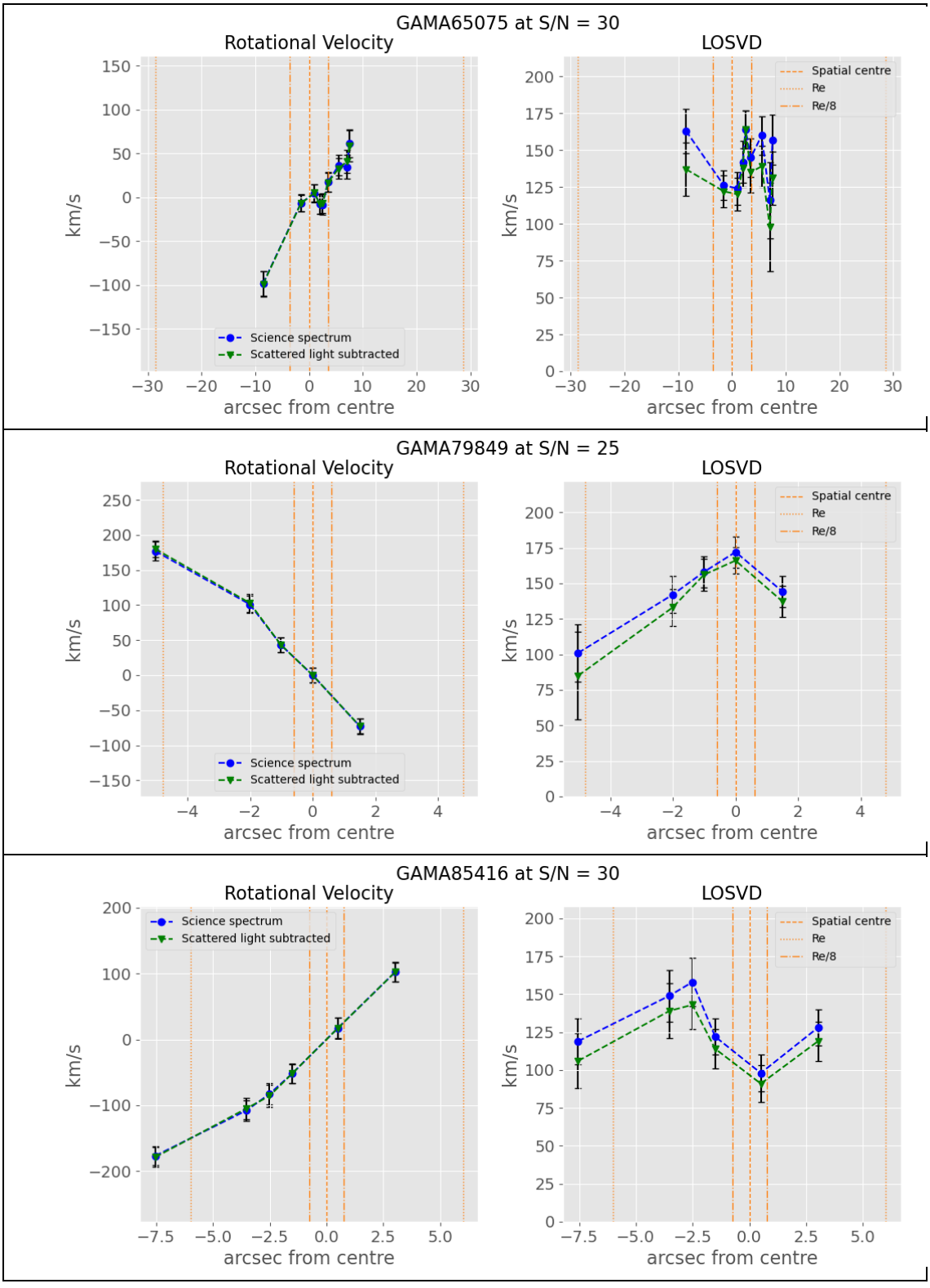

Figure 6-2 continued.

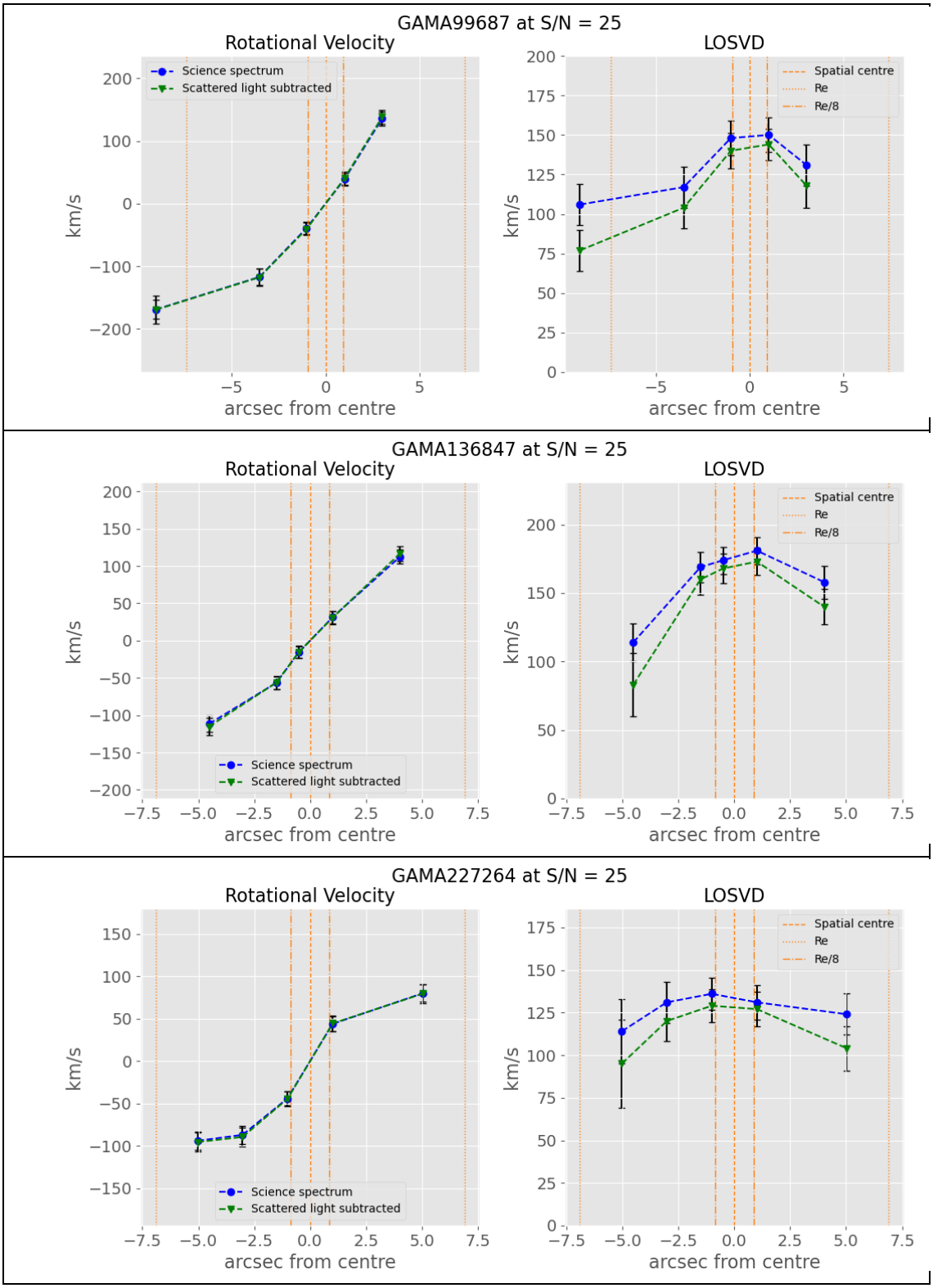

Figure 6-2 continued.

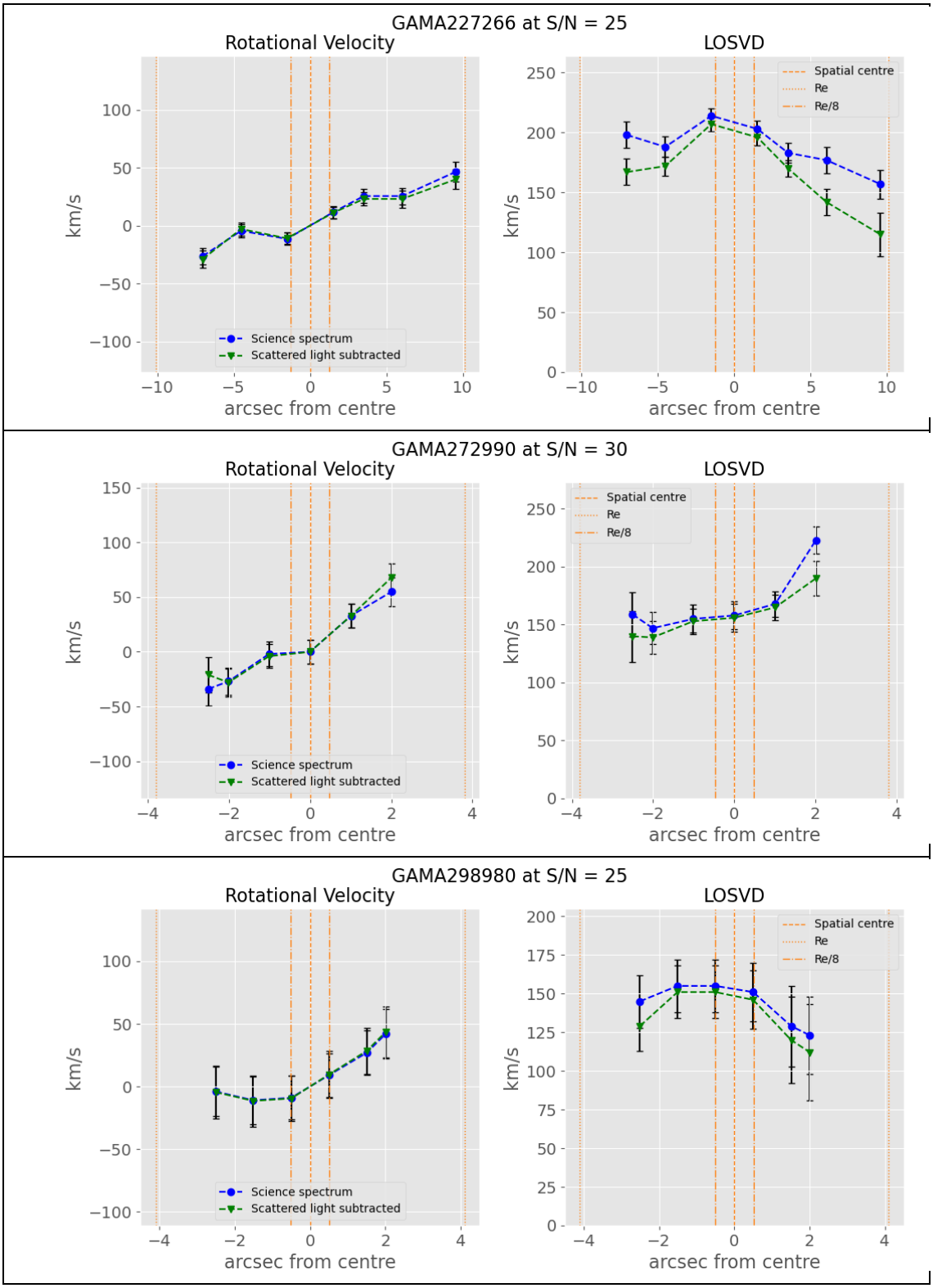

Figure 6-2 continued.

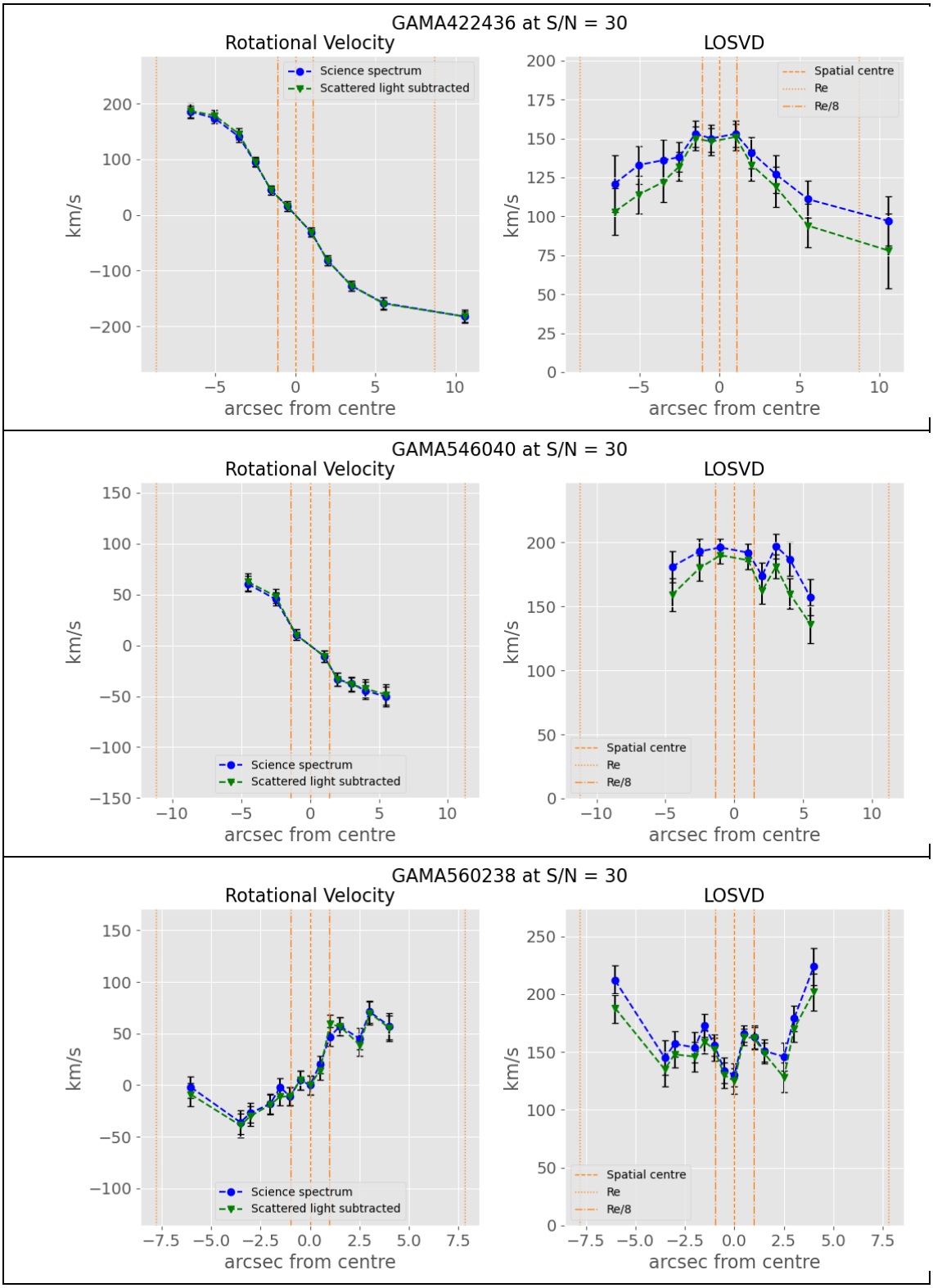

Figure 6-2 continued.

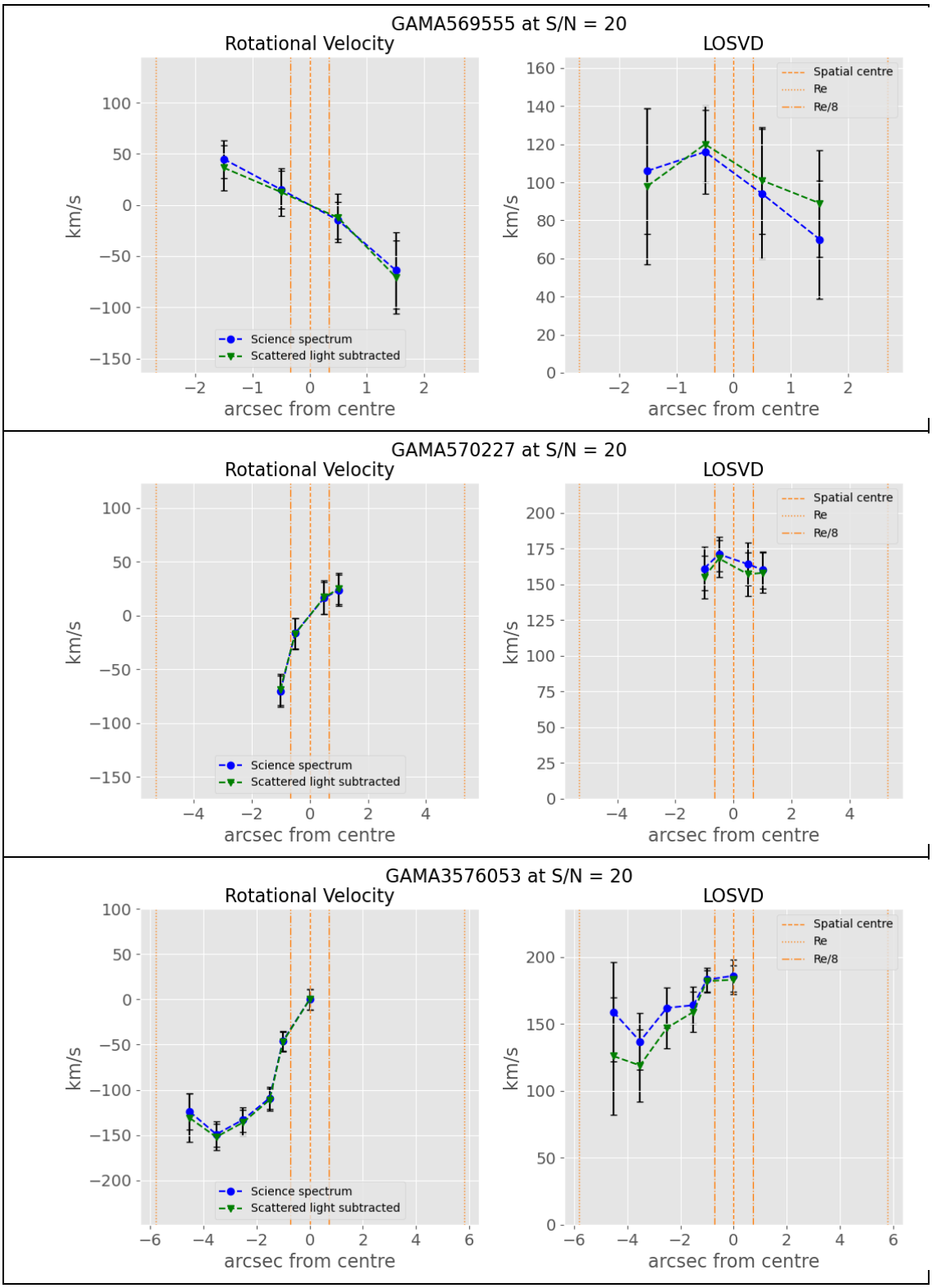

Table 6-3: Derived kinematic results for the central $R_e/8$ aperture of each target. Systematic velocity is recession velocity of the central aperture calculated by pPXF.

GAMA Galaxy	S/N ratio for profile	Number of bins	Spatial extent of profile	Systematic Velocity	Systematic Velocity as Redshift	Max Measured Rotational Velocity	Rotational Velocity Uncertainty	Central LOSVD	LOSVD Uncertainty	Velocity/ LOSVD	Ellipticity (ε)	Ellipticity Uncertainty
			arcsec	km s^{-1}		km s^{-1}	km s^{-1}	km s^{-1}	km s^{-1}			
								[1]		[2]	[3]	[4]
65075	30	9	16	1657	0.0055	99	14.3	126	9.9	0.79	0.336	0.0004
79849	25	5	7	13222	0.0441	180	12.2	158	9.0	1.14	0.423	0.0013
85416	30	6	11	5775	0.0193	179	14.9	89	11.0	2.01	0.665	0.0005
99687	25	5	12	14019	0.0468	170	22.5	142	12.0	1.19	0.624	0.0010
136847	25	5	9	8125	0.0271	117	9.9	168	8.8	0.69	0.298	0.0023
227264	25	5	10	7389	0.0246	96	10.9	132	8.4	0.72	0.449	0.0017
227266	25	5	17	7412	0.0247	47	8.6	203	6.0	0.23	0.112	0.0014
272990	30	6	4.5	12063	0.0402	68	12.6	160	9.5	0.43	0.254	0.0026
298980	25	6	4.5	7973	0.0266	44	20.4	149	17.0	0.29	0.322	0.0020
422436	30	11	17	7628	0.0254	187	13.7	147	7.7	1.27	0.584	0.0060
546040	30	8	10	7844	0.0262	63	8.5	190	6.4	0.33	0.086	0.0013
560238	30	14	10	6311	0.0211	70	11.1	148	7.5	0.47	0.295	0.0012
569555	20	4	3	16608	0.0554	71	35.6	108	18.0	0.65	0.392	0.0021
570227	20	5	3.5	12722	0.0424	69	14.6	160	11.0	0.43	0.578	0.0014
3576053	20	6	5	15152	0.0505	152	14.3	186	8.6	0.82	0.179	0.0022
78425	Insufficient S/N for kinematic analysis											

Table 6-3 notes:
[1] from the central $R_e/8$ aperture
[2] Equals Column 3 / Column 5
[3] from GAMA Catalogue parameter GALELLIP_r
[4] from GAMA Catalogue parameter GALELLIPERR_r

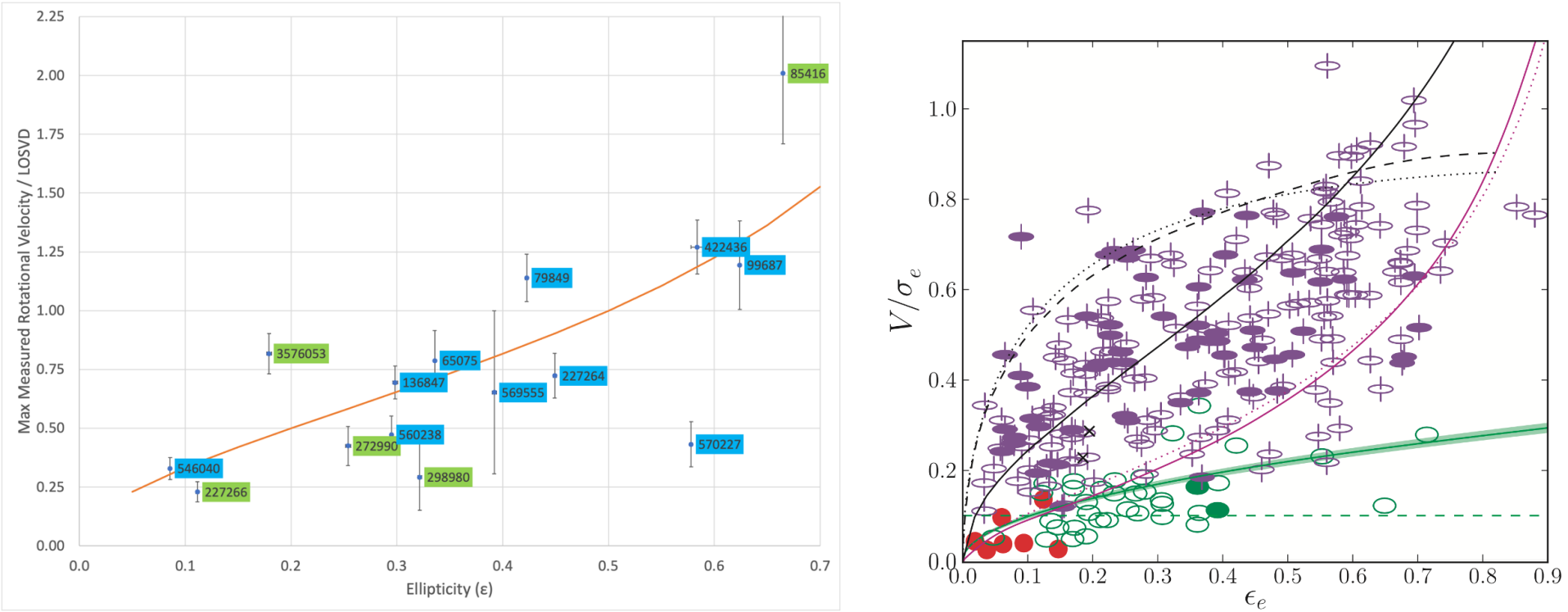

Figure 6-3: The left panel shows a plot of (maximum measured rotational velocity/LOSVD for the $R_e/8$ aperture) vs ε for the target ETGs, therefore, the points represent minimum possible value for V_{max}/LOSVD. The orange line represents isotropic oblate spheroids that are flattened only by rotation, according to the approximation by Kormendy, given in Equation 6-2. Lenticular galaxies are tagged blue and elliptical are tagged green. For comparison the right panel shows (velocity/LOSVD) vs ε for the ATLAS^{3D} sample (Emsellem *et al.*, 2011). The solid black line shows isotropic oblate systems viewed edge-on. Red circles show galaxies with no apparent rotation, green ellipses are non-regular rotators and purple symbols are regular rotators. Both the results from this project and from ATLAS^{3D} show rotational support for the lenticular ETGs.

6.3 Stellar Populations

Results for analysis of the central $R_e/8$ aperture stellar populations are presented in Table 6-4, with corresponding pPXF output plots presented in Figure 6-6. Table 6-4 shows the average stellar population age in the central $R_e/8$ apertures is intermediate to old[20] in all target ETGs, however, the pPXF age vs. metallicity grids presented in Figure 6-6, suggest younger stellar population components in GAMA85416, 272990, 298980 and 569555. The presence of younger stellar population components is reinforced by emission features in the spectra of GAMA85416, 298980 and 569555, see Appendix B,

A comparison with the SAURON survey results in Figure 6-4 shows that all targets –

1. have average central stellar population ages within the range reported by SAURON.
2. are within the SAURON range of metallicities except for GAMA298980 and 569555, which have significantly lower metallicity results.

Results for the central area of seven nearby ETGs, obtained from SALT longslit spectra by Katkov, Kniazev and Sil'chenko (2015), show ages in the range ~1.4×10^9 to ~8×10^9 yr, and metallicities in the range -0.38 to -0.16 dex. Comparison with Table 6-4, shows the sample from this project to have older central ages of ~3.9×10^9 to ~1.3×10^{10}, and a greater range of metallicities of -0.456 to +0.297 dex. However, the Katkov, Kniazev and Sil'chenko results also show younger ages and lower metallicities than the results from SAURON in Figure 6-4.

Figure 6-5 shows a plot of metallicity for the central $R_e/8$ aperture vs. log $M_\star$. Due to high uncertainties this plot shows only a loose trend of increasing metallicity with increasing stellar mass. A comparison with results from Trussler *et al.* (2021), in the right side panel of Figure 6-5, shows results from this project are consistent with their samples of Passive or Green Valley galaxies and less consistent with their sample of Star Forming galaxies. Figure 6-5 also shows that GAMA298980 and 569555, and also GAMA99687, have low metallicities for their mass, confirming the result from comparison with SAURON.

Plots of velocity, LOSVD, log age and metallicity vs. spatial position for four target ETGs where $\Delta\chi^2$ did converge through the desired $\Delta\chi^2$ are presented in Figure 6-7. These

[20] The following definitions of stellar population ages are used in this Thesis - Young < 1 Gyr. Intermediate 1 < age < 8 Gyr. Old > 8 Gyr.

show age and metallicity profiles matching trends from the SAURON survey, presented in Figure 6-4, where –

- age is independent of spatial position for old stellar populations i.e. red lines on the SAURON age plot
- metallicity decreases with increasing radius. SAURON results show an average reduction of ~-0.35 dex over R_e, and a similar order of reduction is seen in Figure 6-7 for GAMA227266, 422436 and 560238. GAMA546040 shows a steeper reduction in metallicity.

Kinematic profiles from pPXF stellar populations fittings compare well (within their uncertainties) with results from stellar kinematics fittings, shown by proximity of the green and red lines in Figure 6-7. However, there appears to be a systematic offset where the value of line-of-sight velocity from populations fitting is ~10 kms^{-1} greater than the value from kinematics fitting. One spectral pixel is equivalent to 1.25Å in the wavelength calibrated spectra, ≡ ~75 km s^{-1} at 5000Å, making the offset significantly less than 1 pixel equivalent. Therefore, the offset is not due to different pixel to wavelength mapping in the kinematics and populations pPXF scripts and will not have a material effect on the LOSVD, age or metallicity results.

Table 6-4: Results from analysis of stellar populations within the central $R_e/8$ aperture of each target galaxy.

GAMA Galaxy	$R_e/8$	$R_e/8$	Central Aperture	S/N Ratio	Reduced $\chi 2$	Normalised S/N Ratio	regul	Reduced $\chi 2$	$\Delta\chi 2$	Mass Weighted Age	Age min	Age max	Mass Weighted Metallicity	Metallicity min	Metallicity max
	GALRE_r	[1]	[2]	[3]	[4]	[5]		[6]	[7]		[8]	[8]	[9]	[8]	[8]
	arcsec	pixels	pixels							yr	yr	yr	dex	dex	dex
65075	3.9	7.6	15	73.4	3.8	37.46	0.0	1.00	0.00	1.36E+10	-	-	-0.012	-	-
							20.0	1.02	35.90	1.22E+10	6.31E+09	1.40E+10	-0.059	-1	0.4
78425	0.3	0.5	1	7.2	-	-	-	-	-	-	-	-	-	-	-
79849	0.6	1.2	3	37.4	1.1	36.78	0.0	0.99	0.00	7.24E+09	-	-	0.177	-	-
							20.0	1.01	28.57	7.26E+09	2.51E+09	1.12E+10	0.192	-0.4	0.4
85416	0.7	1.4	3	46.8	2.5	30.02	0.0	0.99	0.00	1.26E+10	-	-	0.268	-	-
							20.0	1.01	31.11	1.19E+10	1.00E+10	1.40E+10	0.180	-0.3	0.4
99687	0.8	1.6	3	30.7	0.5	46.08	0.0	1.00	0.00	1.10E+10	-	-	-0.182	-	-
							20.0	1.01	24.84	9.79E+09	6.31E+09	1.40E+10	-0.128	-0.8	0.3
136847	1.0	2.0	5	48.6	1.7	40.87	0.0	1.00	0.00	9.91E+09	-	-	0.316	-	-
							20.0	1.01	34.74	1.03E+10	7.08E+09	1.38E+10	0.282	0	0.4
227264	0.9	1.7	3	23.6	0.2	53.40	0.0	1.00	0.00	1.21E+10	-	-	0.241	-	-
							20.0	1.02	37.96	1.17E+10	1.00E+10	1.40E+10	0.204	0	0.4
227266	1.2	2.4	5	24.9	0.2	55.90	0.0	1.00	0.00	1.35E+10	-	-	0.331	-	-
							16.8	1.03	69.20	1.24E+10	1.00E+10	1.40E+10	0.297	0.1	0.4
272990	0.5	0.9	3	49.7	1.3	43.53	0.0	1.00	0.00	7.01E+09	-	-	-0.093	-	-
							20.0	1.01	25.55	5.07E+09	1.78E+09	6.31E+09	0.029	-0.7	0.4
298980	0.5	0.9	3	34.5	1.6	27.04	0.0	1.00	0.00	1.04E+10	-	-	-0.435	-	-
							20.0	1.00	10.38	7.87E+09	2.24E+09	1.40E+10	-0.373	-1	0
422436	1.0	2.0	5	49.9	1.7	41.58	0.0	1.00	-0.45	1.39E+10	-	-	0.264	-	-
							11.2	1.03	69.50	1.29E+10	1.12E+10	1.40E+10	0.238	0.1	0.4
546040	1.5	2.9	5	44.6	0.9	53.35	0.0	1.00	0.00	1.39E+10	-	-	0.264	-	-
							12.3	1.03	69.20	1.29E+10	1.12E+10	1.40E+10	0.245	0.1	0.4
560238	1.1	2.1	5	87.4	3.2	50.67	0.0	1.00	0.00	1.32E+10	-	-	0.267	-	-
							19.6	1.03	69.20	1.20E+10	1.12E+10	1.40E+10	0.240	0	0.4
569555	0.3	0.7	3	36.3	1.6	28.63	0.0	1.00	0.00	6.89E+09	-	-	-0.425	-	-
							20.0	1.01	11.78	5.69E+09	2.82E+09	1.12E+00	-0.456	-2.27	0.4
570227	0.7	1.4	5	34.8	1.1	33.07	0.0	1.00	0.00	9.66E+09	-	-	0.122	-	-
							20.0	1.01	20.96	9.02E+09	5.62E+09	1.12E+10	0.120	-0.9	0.4
3576053	0.8	1.5	5	35.3	0.8	39.52	0.0	1.00	0.00	5.89E+09	-	-	0.153	-	-
							20.0	1.01	24.47	3.86E+09	2.24E+09	7.94E+09	0.269	-0.2	0.4

Table 6-4 Notes –

[1] Central Aperture = (R_e/8)×2 (rounded to odd number)

[2] Pixels = binned pixels

[3] Measured as the median value from division of the aperture from the spectrum with scattered light removed by its sigma aperture

[4] From pPXF fitting using the S/N ratio in column 5

[5] Normalised to achieve reduced $\chi^2 = 1$

[6] From pPXF fitting using the normalised S/N ratio in column 7

[7] Desired $\Delta\chi^2 = 69.3$

[8] From pPXF age vs. metallicity grids presented in Figure 6-6

[9] Mass Weighted Metallicity ([M/H]) uses the metallicity definition from the MILES Library, see Glossary of Terms

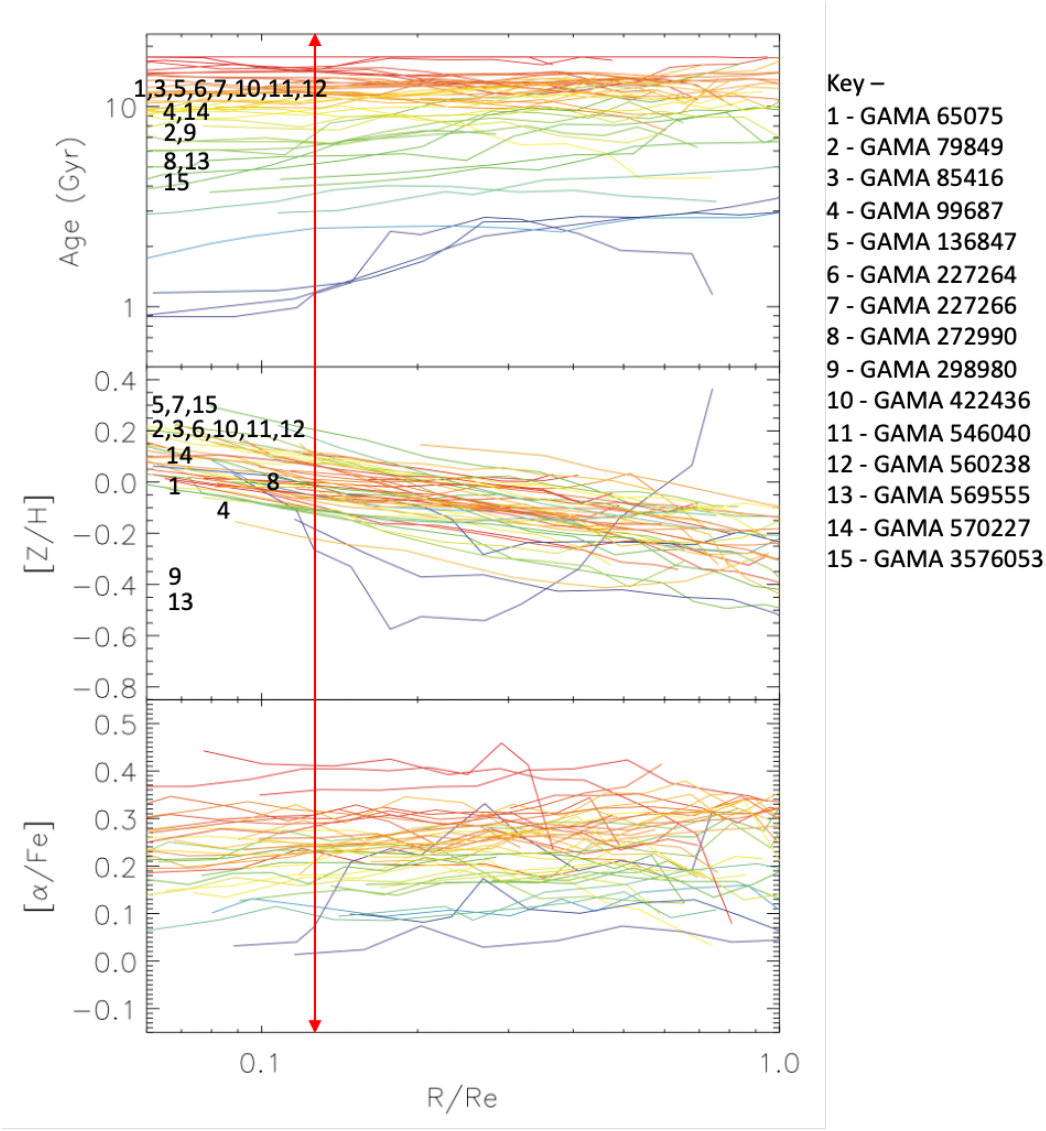

Figure 6-4: Plots of Age, [Z/H] and [α/Fe], taken from Kuntschner *et al.* (2010), show radial profiles for 48 ETGs in the SAURON survey. Line colour shows central $R_e/8$ age, with red indicating old and blue young stellar populations. Superimposed are central Age and [M/H] results from this project (Table 6-4 columns 11 and 14), shown by vertical position relative to the y-axis and with number indicating the ETG. Horizontal position is set to fit the numbers into the diagram and is not related to R/R_e. The vertical red line represents spatial extent of the $R_e/8$ aperture in the Kuntschner *et al.* (2010) data. MILES SSP templates used for fitting cover the full y-axis scale for Age and [Z/H].

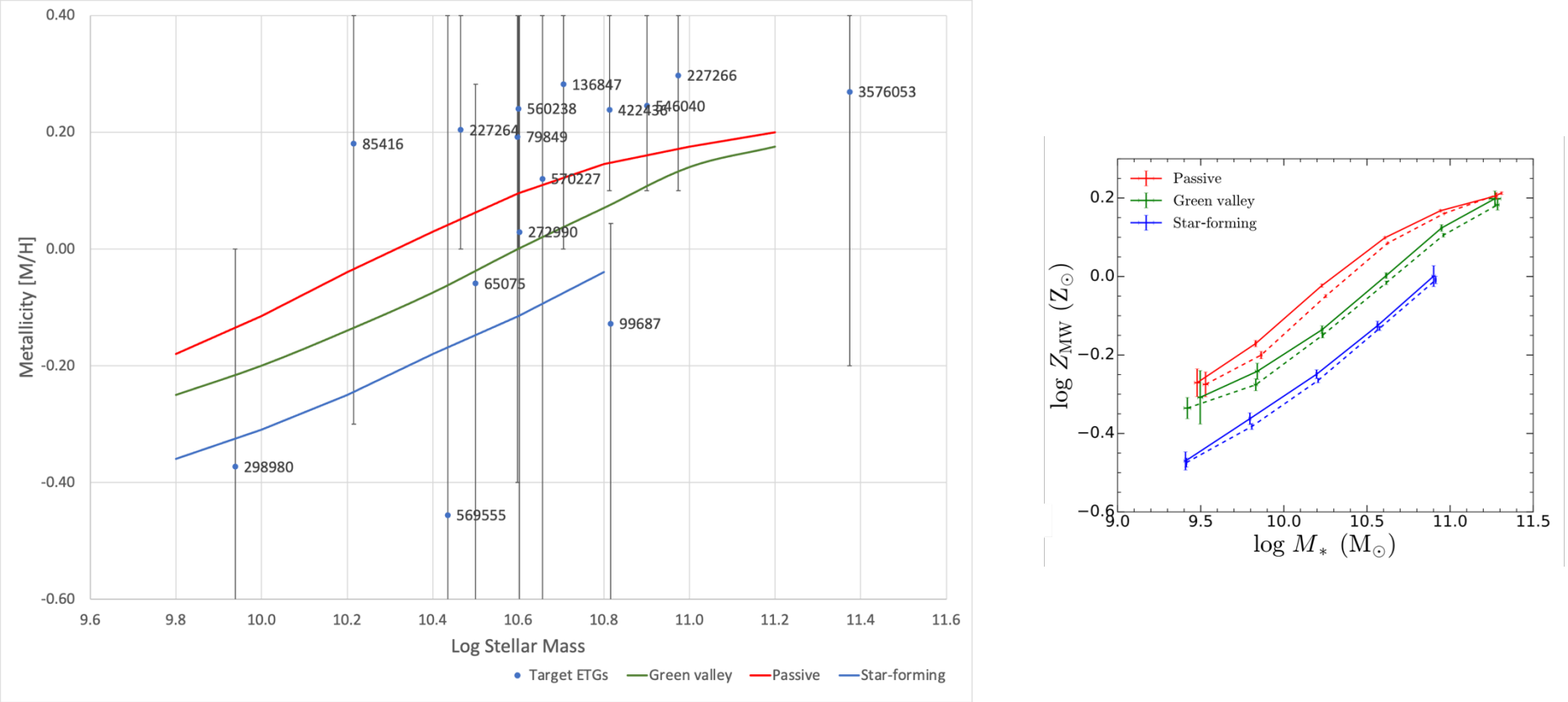

Figure 6-5: The left panel shows a plot of metallicity [M/H] (from Table 6-4) vs. log M★ (from Table 2-2) for the target ETGs. Results indicate increasing metallicity with increasing mass, with the caveat of very high uncertainties. Coloured lines are M★ vs. metallicity relationships for satellite Green Valley, Passive and Star forming galaxies from Trussler *et al.* (2021). The right panel reproduces the M★ vs. metallicity plot from Figure 2 of Trussler *et al.* (2021), where solid lines are satellite galaxies and dotted lines are centrals. Central and satellite galaxies may experience different environmental processes due to their position in a cluster's dark matter halo, however, their differences in metallicity are much less than difference in metallicity due to SFR categorisations (at a given M★.)

Figure 6-6: pPXF output plots from analysis of stellar populations within the central $R_e/8$ aperture. For each target the top panel shows the fit with regul = 0 and the bottom panel the fit with regul equal to the value listed in Table 6-4. Content of the plots is as described in Figure 5-1, with the x-axis in log rebinned pixels (pixel 0 ≡ 3800Å and pixel 2400 ≡ 6800Å).

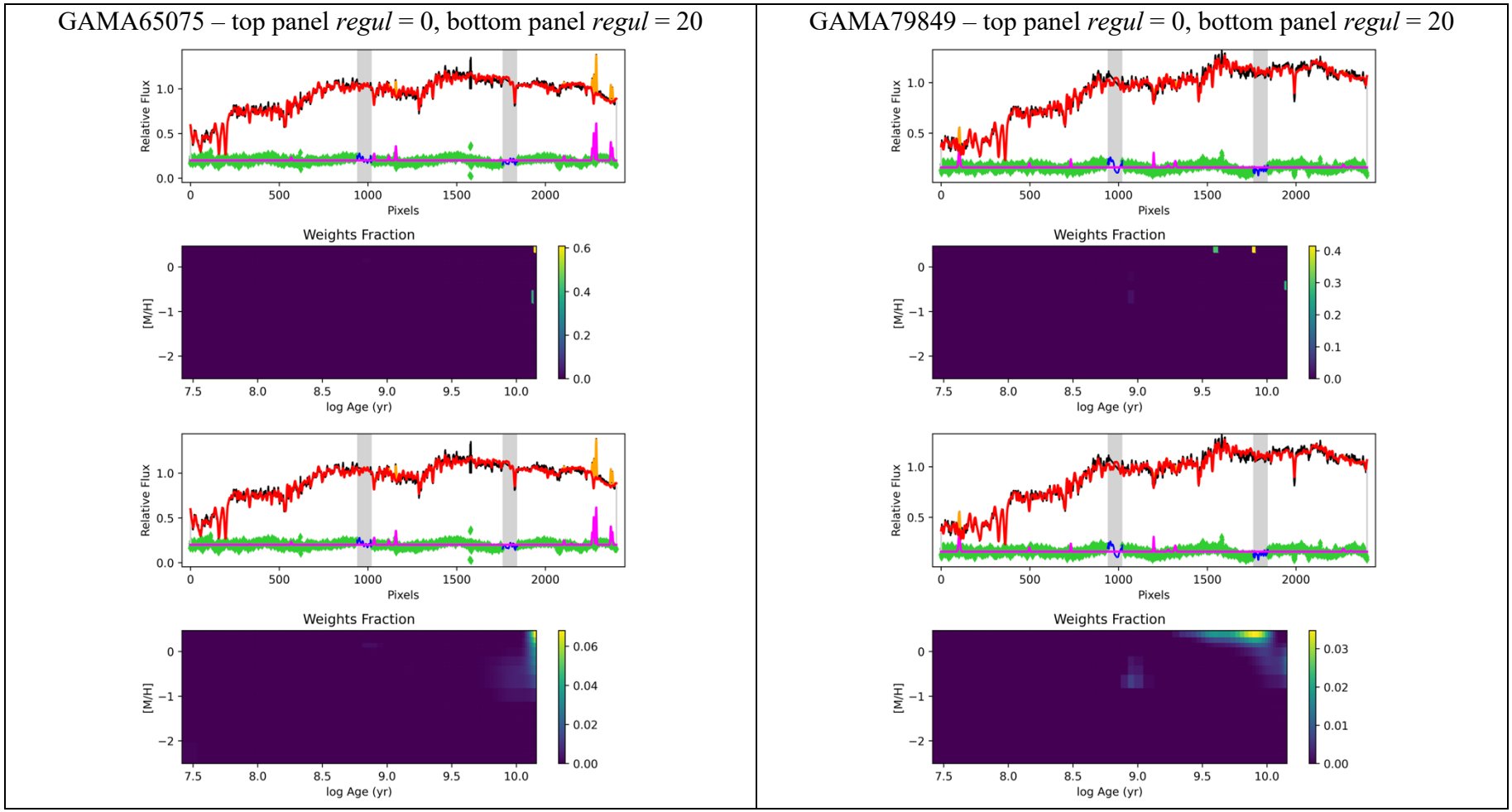

Figure 6-6: continued.

GAMA85416 – top panel *regul* = 0, bottom panel *regul* = 20

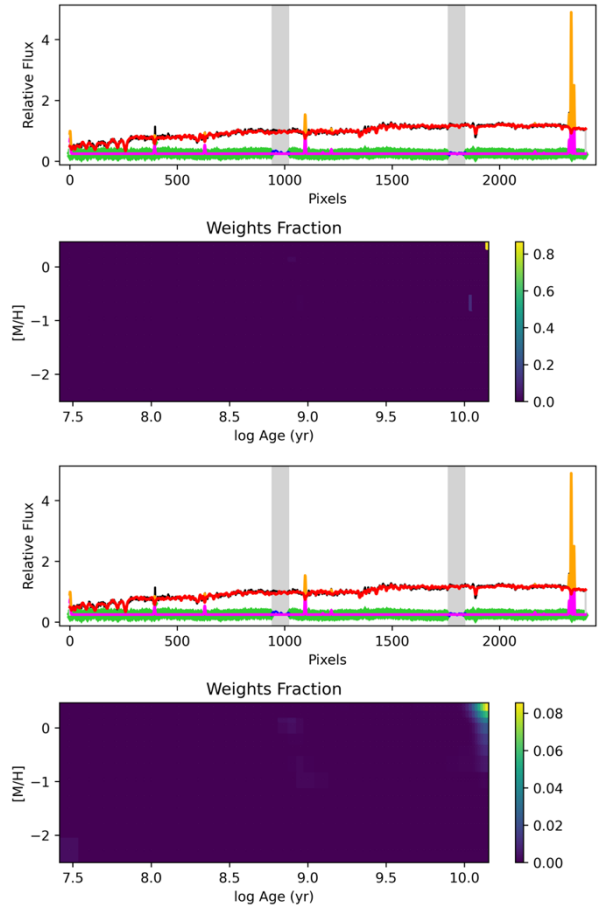

GAMA99687 – top panel *regul* = 0, bottom panel *regul* = 20

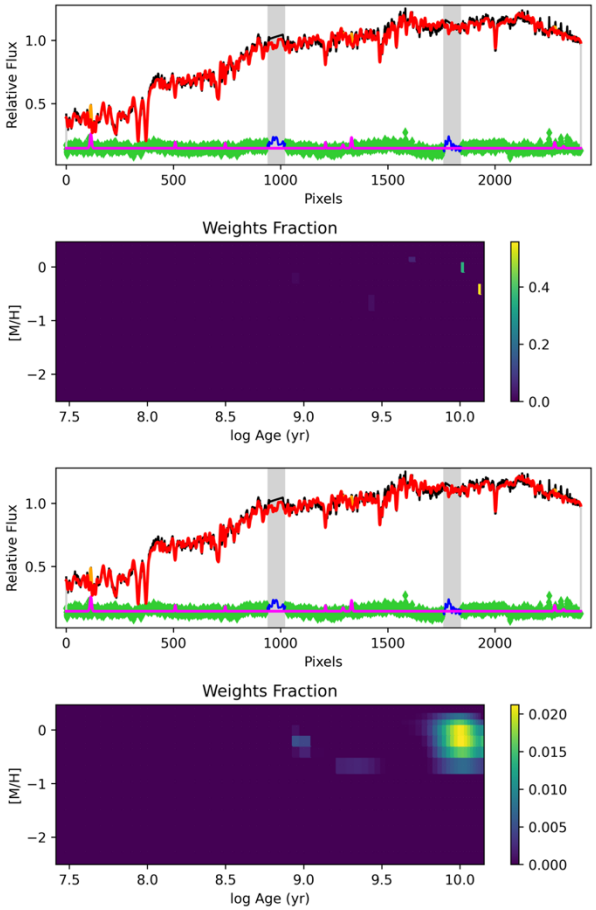

Figure 6-6: continued.

GAMA136847 – top panel *regul* = 0, bottom panel *regul* = 20

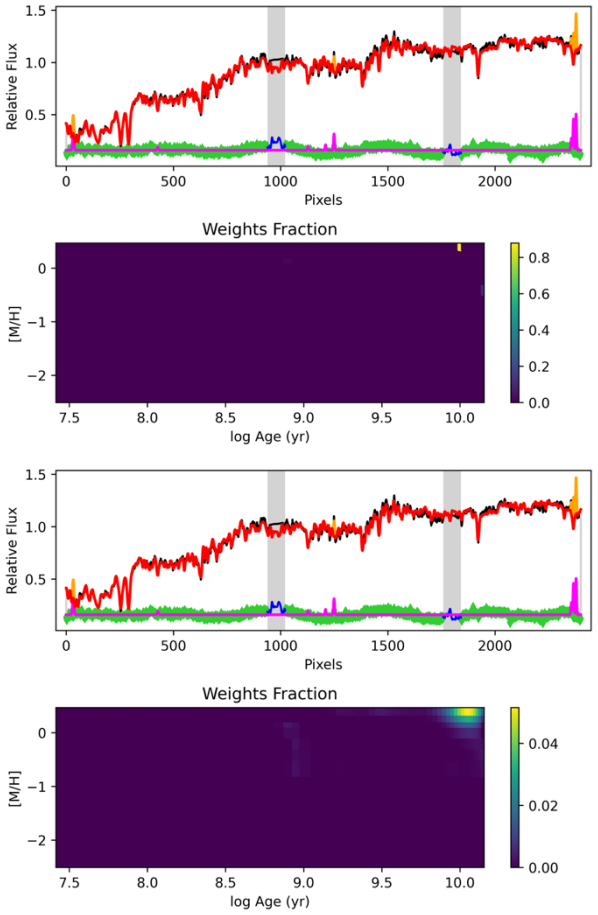

GAMA227264 – top panel *regul* = 0, bottom panel *regul* = 20

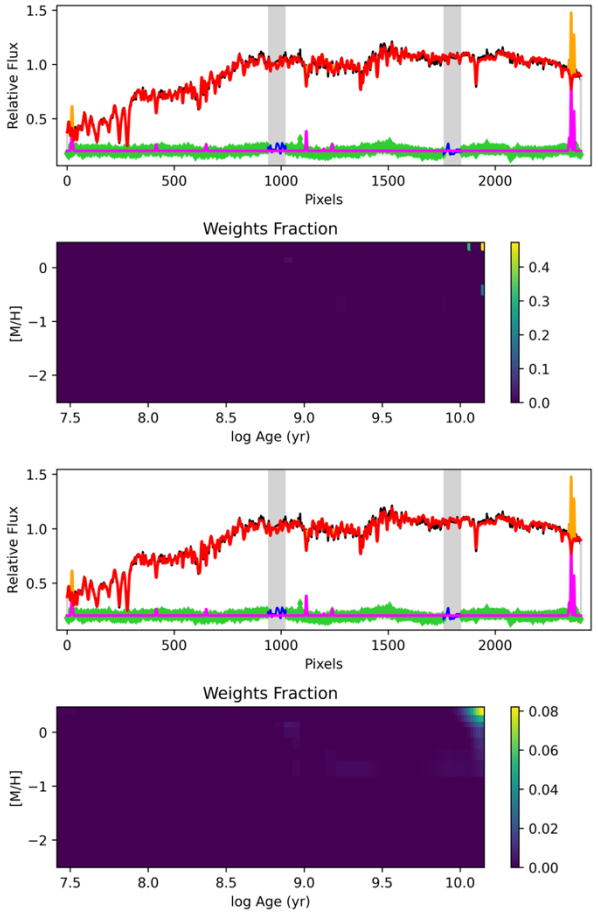

Figure 6-6: continued.

GAMA227266 – top panel *regul* = 0, bottom panel *regul* = 16.8

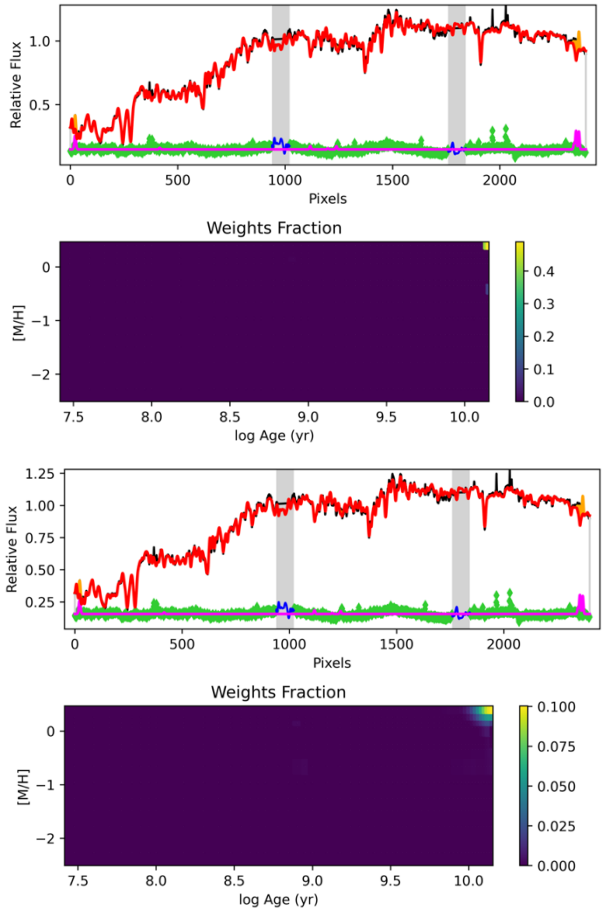

GAMA272990 – top panel *regul* = 0, bottom panel *regul* = 20

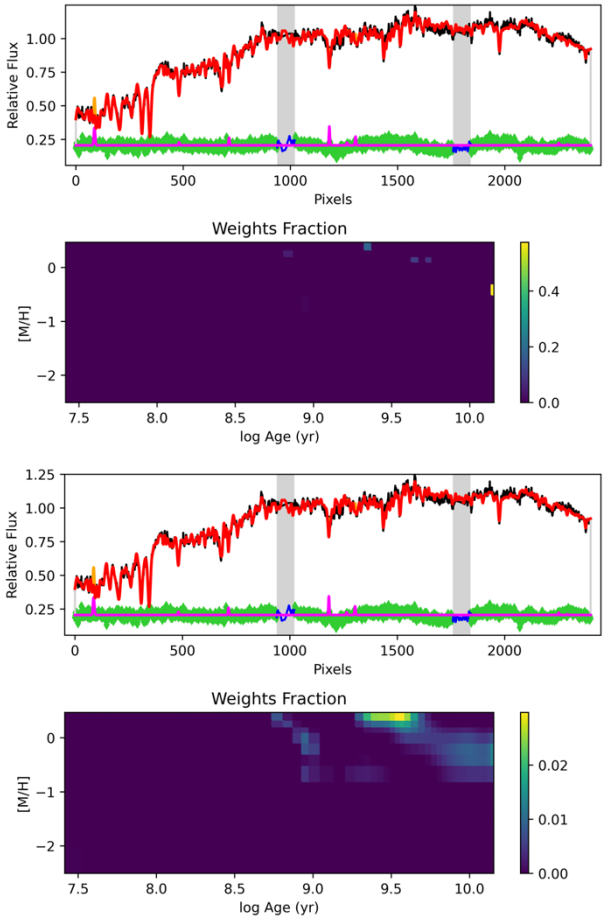

Figure 6-6: continued.

GAMA298980 – top panel *regul* = 0, bottom panel *regul* = 20

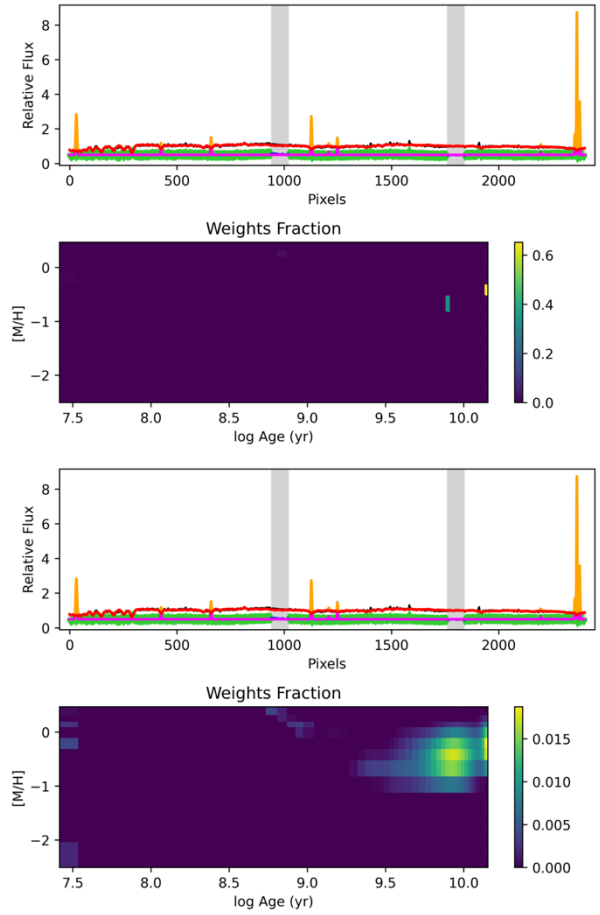

GAMA422436 – top panel *regul* = 0, bottom panel *regul* = 11.2

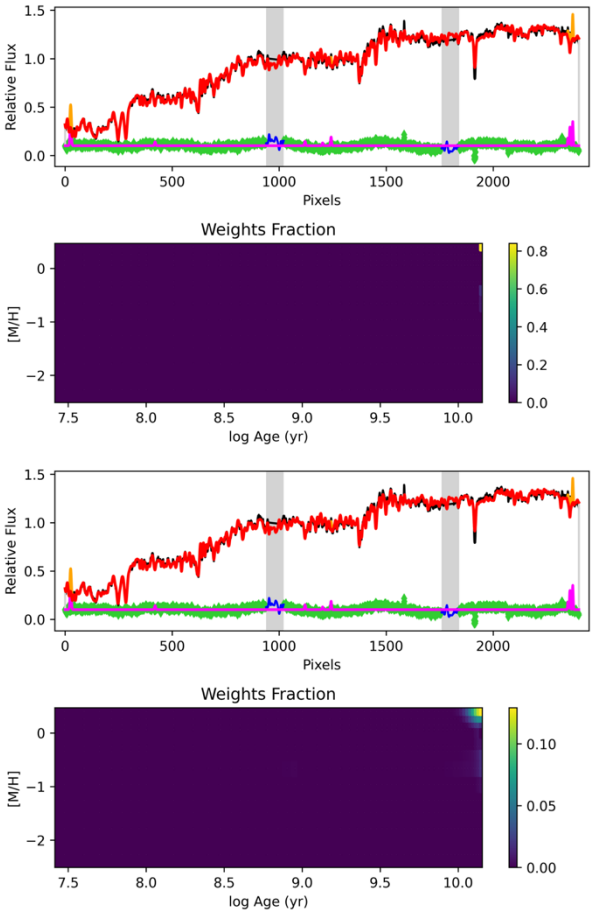

Figure 6-6: continued.

GAMA546040 – top panel *regul* = 0, bottom panel *regul* = 12.3

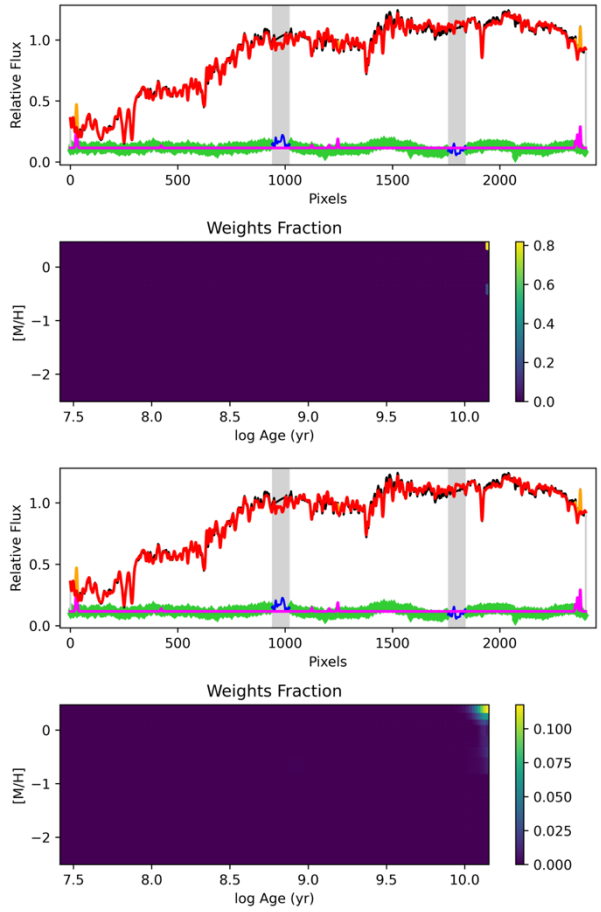

GAMA560238 – top panel *regul* = 0, bottom panel *regul* = 12.3

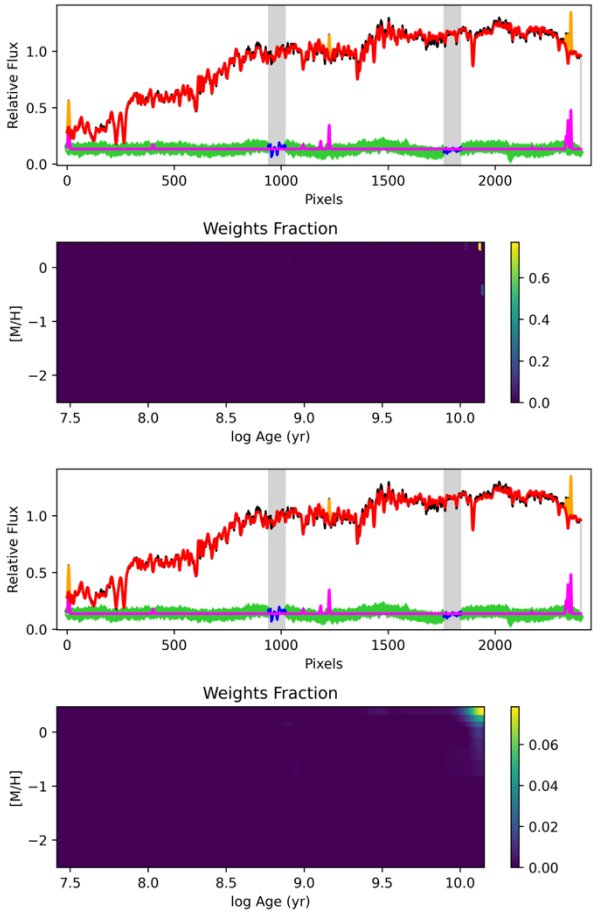

Figure 6-6: continued.

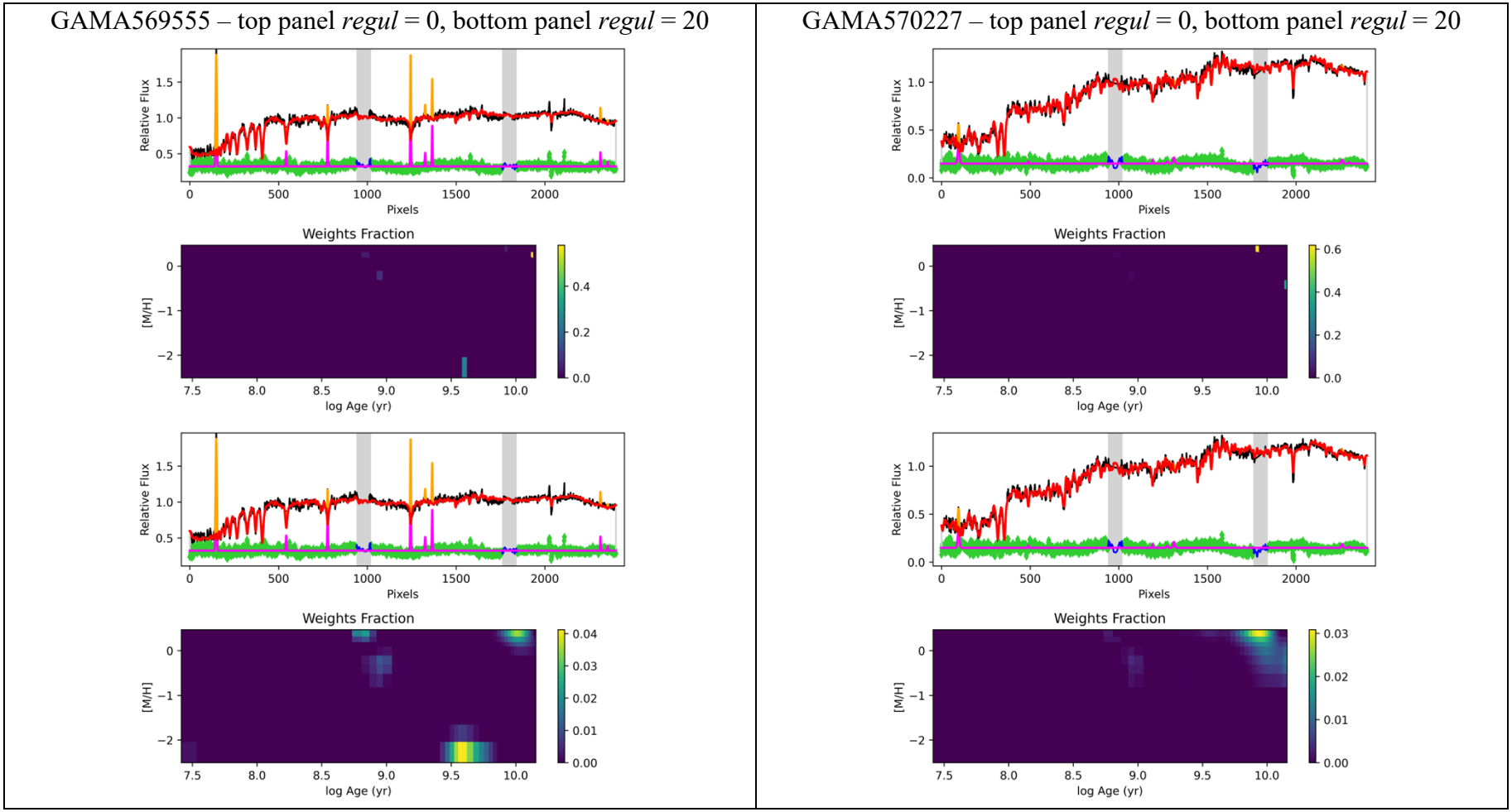

Figure 6-6: continued.

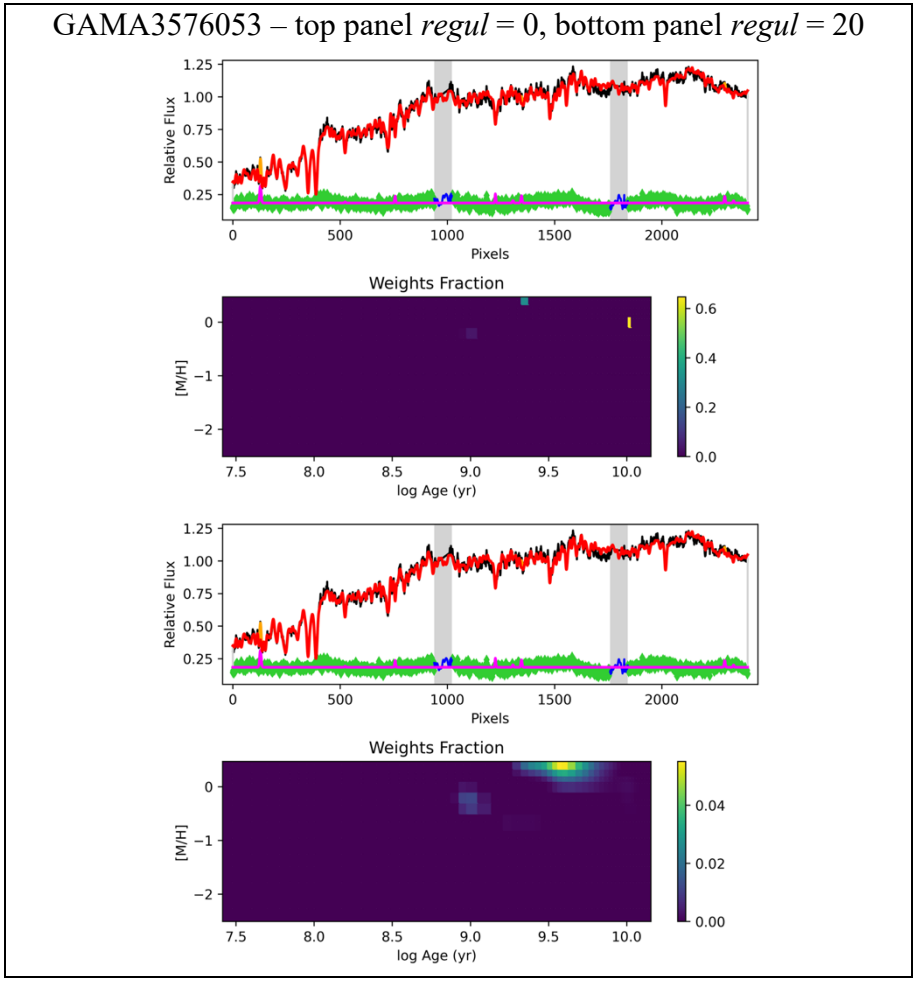

Figure 6-7: Plots of major axis stellar kinematics and populations results from pPXF. Each panel shows results for one target ETG, with the x axis in units of arcsec relative to the galaxy centre. Red lines show results from stellar populations analysis and green lines are results from kinematics analysis. Results are from science spectra from which scattered light has been removed.

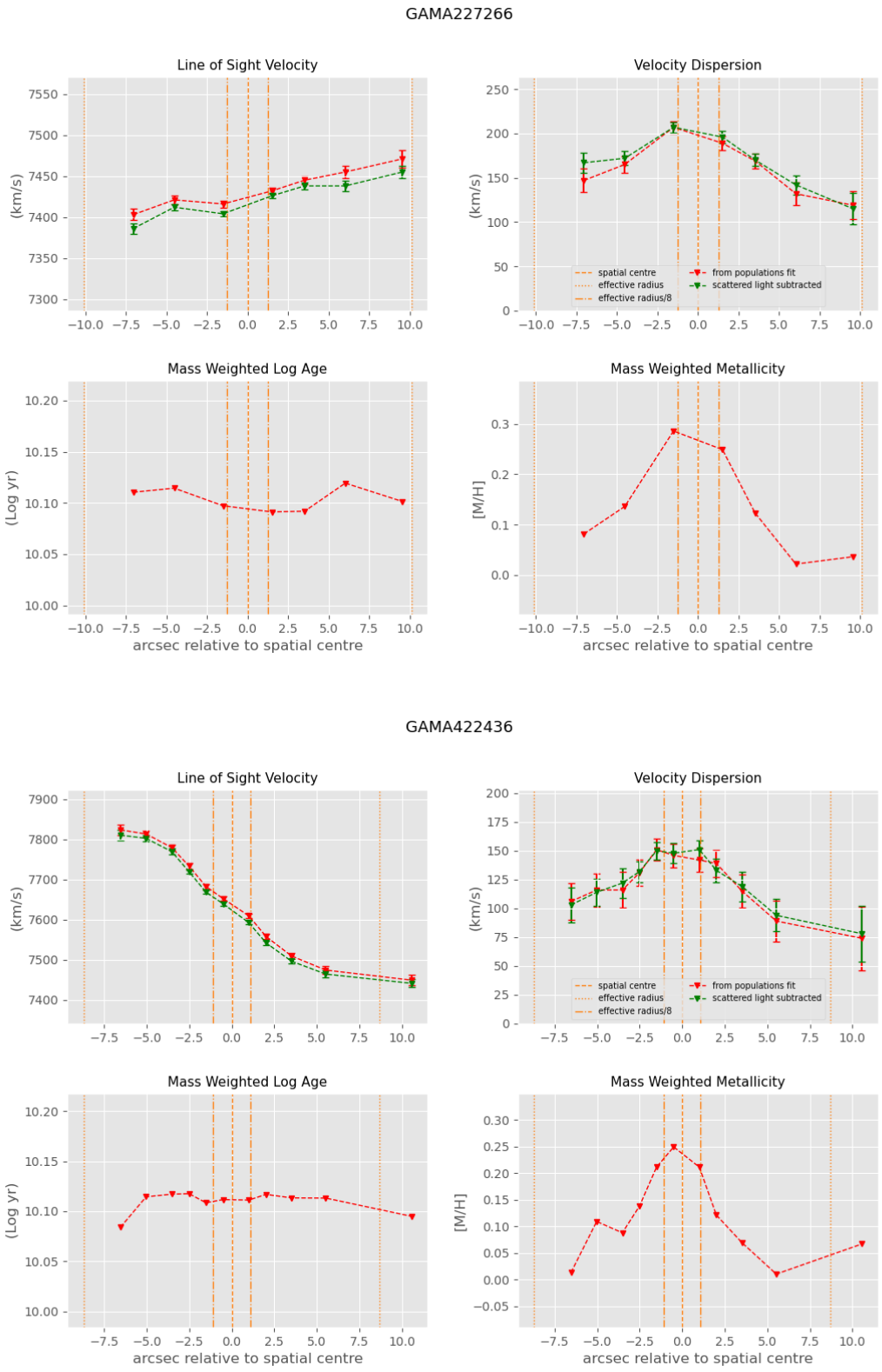

Figure 6-7 continued.

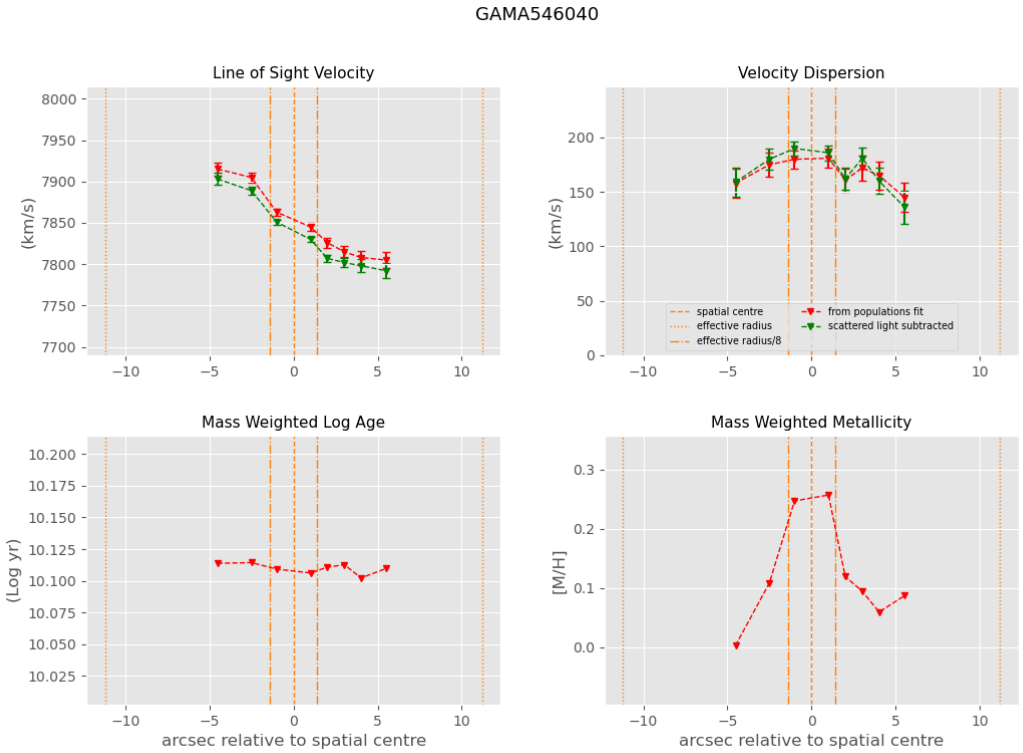

7 DISCUSSION AND CONCLUSIONS

This section provides a discussion of the results for individual ETGs, presents recommendations for follow-up work and conclusions from the results obtained.

7.1 Discussion of Individual Target ETGs

This section gives more specific comments on the results for each individual target galaxy, to supplement results given above. Physical properties of the target ETGs have been summarised in Table 2-2, results from spectroscopy in Table 6-2, stellar kinematics in Table 6-3 and stellar populations in Table 6-4.

7.1.1 GAMA65075

GAMA65075 is not typical of a S0-Sa ETG as it is barred and hosts a ring structure (Vaghmare *et al.*, 2018), which can be seen in Figure 7-1. In addition to the spectroscopy results summarised in Table 6-2 the spectrum displays the [SII] doublet emission feature, as this galaxy is at very low redshift (z=0.0055).

Figure 7-1: GAMA65075 images from the SDSS DR14 Finding Chart Tool[21] The red arrow approximates the direction of the RSS slit and spatial extent of the sampling for S/N ratio = 30, with the arrow pointing towards higher pixel values.

S/N ratio based sampling was not uniform and included the central bulge but not the surrounding ring. The LOSVD profile is not symmetric around the centre line of the trace and LOSVD does not reduce with increasing distance from the spatial centre, as seen for other ETGs in the SAURON and ATLAS^{3D} results. As this LOSVD profile was unusual, fitting was repeated with apertures extracted at S/N ratio = 20 which confirmed the asymmetry, indicating the possibility of sub-structures in the kinematics. However, the

[21] SDSS DR14 Finding Chart Tool is available at https://skyserver.sdss.org/dr14/en/tools/chart/image.aspx.

right panel of Figure 7-1 reveals some features, possibly dust lanes, which may have biased the value of LOSVD and contributed to higher-than-expected LOSVD uncertainties in apertures at higher spatial pixels. The pPXF plot in Figure 6-6 shows an old stellar population and Table 6-4 shows an age of ~1.2×10^{10} yr and metallicity of -0.059 for the central $R_e/8$ aperture. The left panel of Figure 7-1 reveals a bluish outer ring structure suggesting presence of a younger stellar population in this area. These results concur with results from Vaghmare *et al.* (2018) who found a central age of ~1×10^{10} yr and metallicity of 0.015.

7.1.2 GAMA78425

Investigation of the three science spectra, observed on 20190624, showed that the SALT Astronomers Log records significant cloud cover and high humidity for that night, suggesting that insufficient light was received from the target to provide an acceptable S/N ratio spectrum. No useful kinematic or stellar population data could be obtained from GAMA78425 observations.

7.1.3 GAMA79849

Examination of the 2D spectrum revealed a second trace centred on spatial pixel 132 and Figure 7-2 shows an additional light source, however, it is beyond the area sampled for analysis of stellar kinematics and populations.

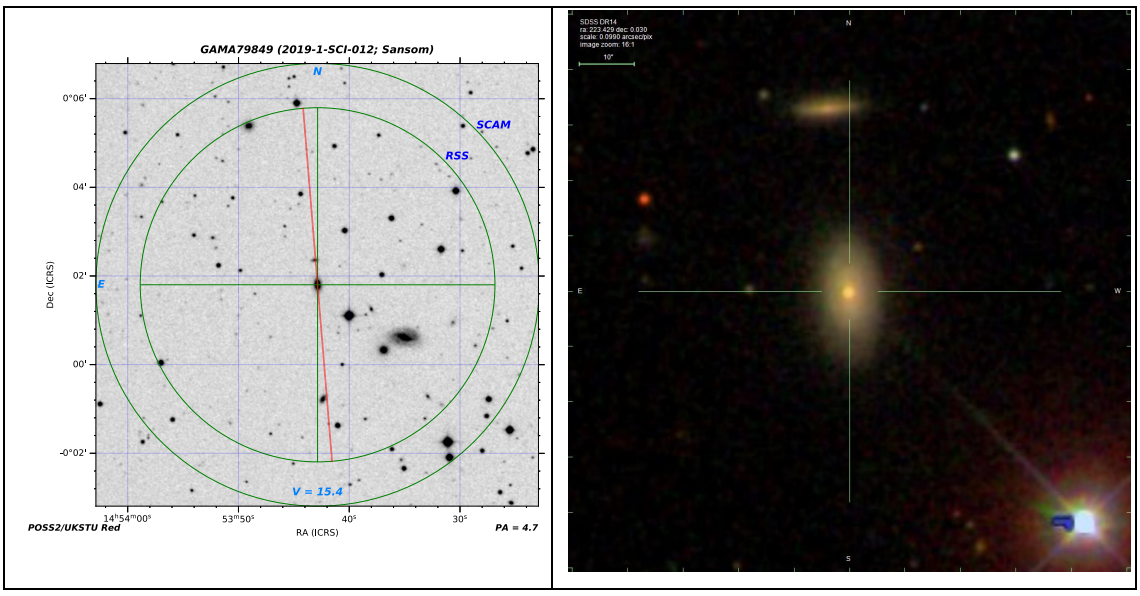

Figure 7-2: The left panel shows a SALT finder chart image for GAMA79849 with slit position indicated by the red line. The right panel is a magnified view of GAMA79849 from the SDSS DR14 Finding Chart Tool, showing the source of the additional trace.

Kinematic plots in Figure 6-2 show LOSVD decreasing and V_{Rot} increasing with distance from the centre. The shape of the LOSVD profile was confirmed using kinematic results extracted at S/N ratio = 20 across 8 spatial bins. The central $R_e/8$ aperture has a

stellar population with an average age of ~7.3×10^9 yr and metallicity of 0.192. The pPXF plot for GAMA79849 in Figure 6-6 shows the possible presence of a second intermediate age stellar population component, with an age of 1×10^9 yr and metallicity ~-0.7.

7.1.4 GAMA85416

The spectrum shows an unidentified strong emission feature at 4185Å which is an artefact from an incompletely removed CR.

The LOSVD profile is very asymmetric around the centre line of the trace, with LOSVD peaking at pixel 196 and not the spatial centre of the trace. This behaviour is present in both apertures extracted from the science spectrum and from the spectrum which has had scattered light removed. The shape of the LOSVD profile was confirmed using kinematic results extracted at S/N ratio = 20 across 11 spatial bins. A spatial cut of the 2D spectrum has an asymmetric spatial profile, shown in Figure 7-3, and the image in Figure 7-4 shows brightness variations in the central area, including yellow irregularities which may be dust lanes, and the possibility of a bluish ring which may indicate a young stellar population component. Figure 6-3 shows GAMA85416 to have the highest ellipticity in the sample and to have the highest V_{max}/LOSVD, making it an outlier when compared to other elliptical galaxies in the sample. The kinematics and image indicate that GAMA85416 may be a lenticular galaxy which has been misclassified as an Elliptical because of its high ellipticity.

The spectrum shows strong Hα, Hβ and [NII] emission features but analysis of the central $R_e/8$ aperture indicated an old stellar population with an average age of 1.19×10^{10} yr and metallicity of 0.18, with minimal indication of a young population component in the pPXF plots in Figure 6-6.

The asymmetric profile in the 2D spectrum, off-centre LOSVD profile, emission features and possible structures in the visual image prompt additional investigation of this target. As the off-centre LOSVD profile has been confirmed using the S/N = 20 apertures, the additional investigation should focus on extraction of profiles for age and metallicity, initially from the existing S/N ratio 20 and 30 apertures. pPXF results from this analysis could be compared with age and metallicity results from an alternative package e.g. STARLIGHT (Cid Fernandes *et al.*, 2005). This could inform a decision to collect additional spectra which could be combined with the original three spectra to generate a 2D spectrum with improved S/N ratio and greater spatial coverage. S/N ratio based spatial binning of this combined spectrum would give additional apertures at greater distance from the centre line, allowing kinematic profiling beyond R_e, and direct measurement of V_{max}. The position of GAMA85416 on the V_{max}/LOSVD vs. ε plot in Figure 6-3 could

then be confirmed. Higher S/N ratio spectra within R_e would also facilitate more granular spatial profiling of the stellar populations to identify locations of any young population components, which can then be correlated with the blue ring structure.

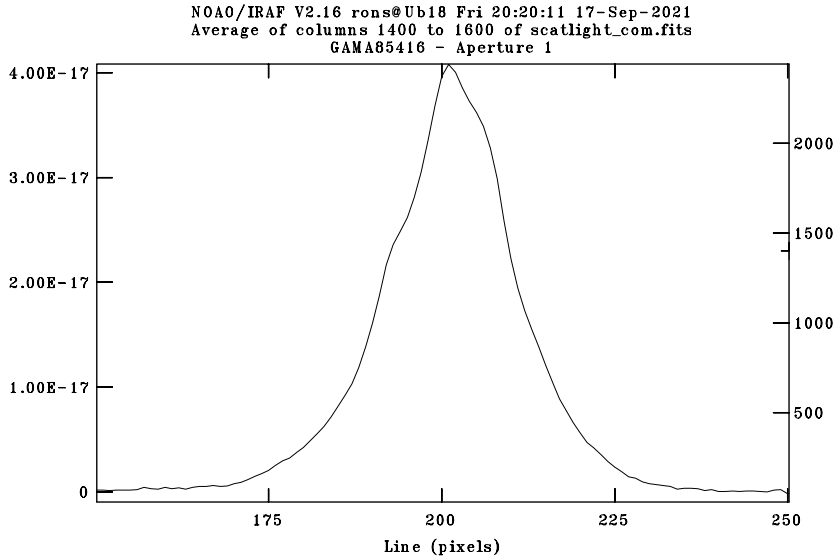

Figure 7-3: Spatial section of columns 1400 – 1600 from the science spectrum of GAMA85416, showing that the spatial profile is not symmetric.

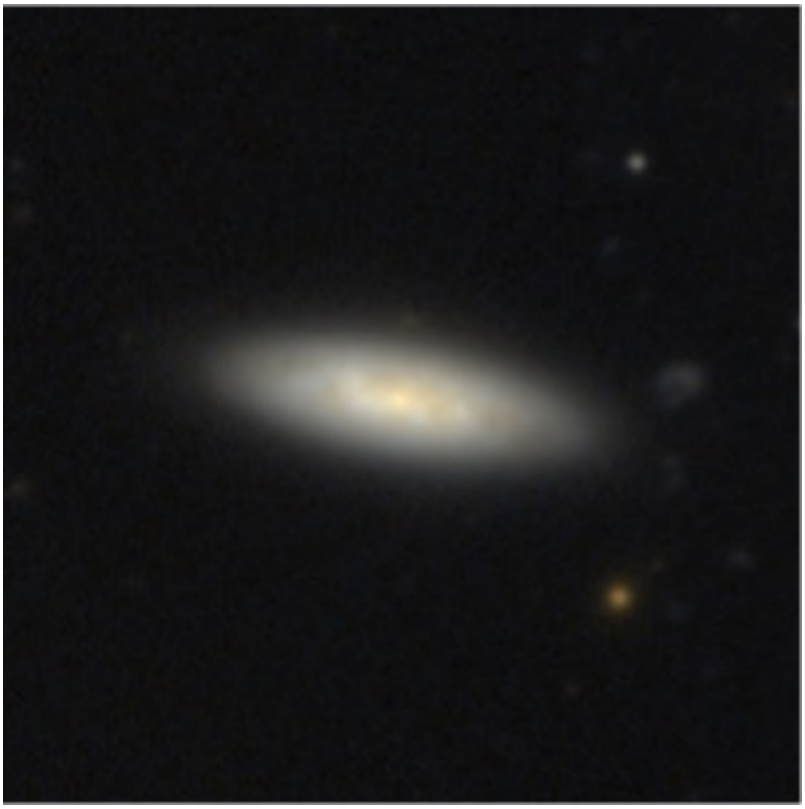

Figure 7-4: Composite RGB image of GAMA85416 (https://datacentral.org.au/services/cutout/). GAMA85416 has high ellipticity, shows possible central dust lanes and a blue tinted ring feature. Image size is 30 arcsec on the x and y axes. RGB colour bands used are, red – WISE W1, green – VST g, blue – SDSS i.

7.1.5 GAMA99687

Analysis of the central $R_e/8$ aperture indicated a stellar population with an average age of 9.8×10^9 yr and metallicity of -0.128. An image of GAMA99687 is presented in Figure 7-5. The pPXF plot in Figure 6-6 shows the possible presence of multiple intermediate and old stellar population components with ages between 1×10^9 and 1×10^{10} yr.

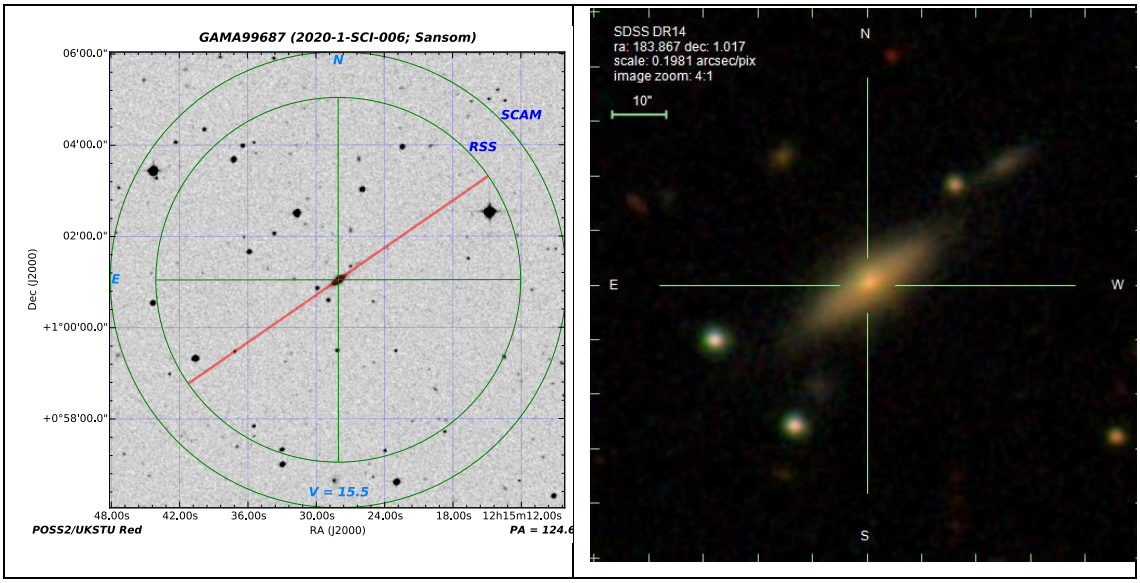

Figure 7-5: Layout is as Figure 7-2. The right panel is a magnified view of GAMA99687 from the SDSS DR14 Finding Chart Tool.

7.1.6 GAMA136847

Examination of the 2D spectrum revealed a second faint extended trace centred on spatial pixel 240 and Figure 7-6 shows the presence of two faint additional light sources in line with the galaxy's major axis. These were beyond the area sampled for analysis of stellar kinematics and populations. The central $R_e/8$ aperture has an old stellar population with an average age of 1×10^{10} yr and metallicity of 0.282, and the pPXF plot in Figure 6-6 shows a single old stellar population.

7.1.7 GAMA227264

Examination of the 2D spectrum revealed a second strong trace centred on spatial pixel 238 and Figure 7-7 shows the presence of an additional blue light source in line with the galaxy's major axis. This was beyond the area sampled for analysis of stellar kinematics and populations. The central $R_e/8$ aperture has an old stellar population with an average age of $\sim1.2\times10^{10}$ yr and metallicity of 0.204, and the pPXF plot in Figure 6-6 shows a single old stellar population.

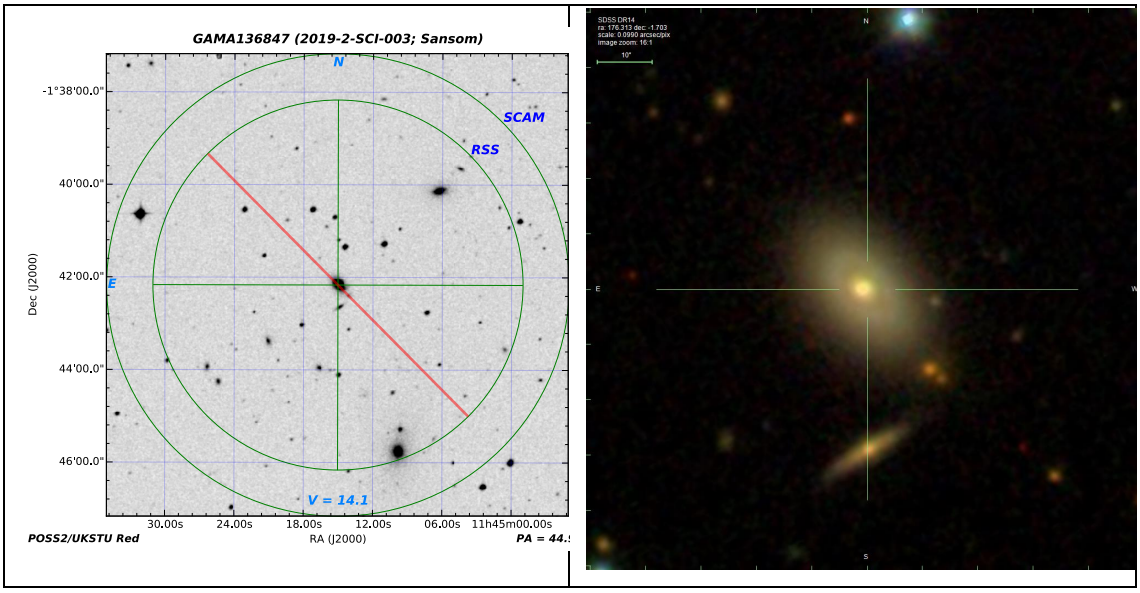

Figure 7-6: Layout is as Figure 7-2. The right panel is a magnified view of GAMA136847 from the SDSS DR14 Finding Chart Tool, showing the additional trace is due to two faint light sources aligned with the major axis.

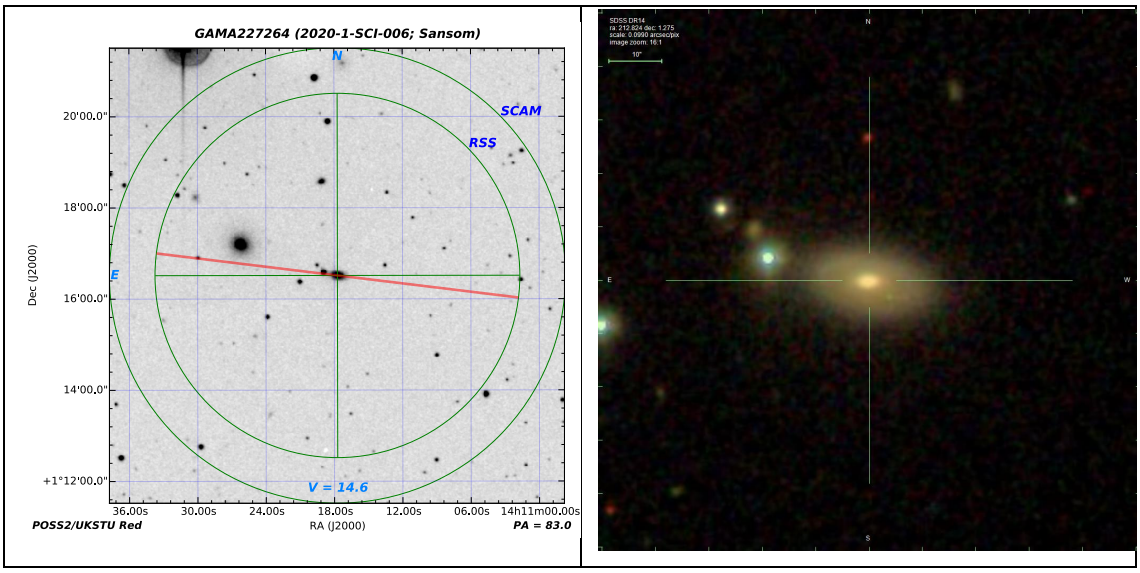

Figure 7-7: Layout is as Figure 7-2. The right panel is a magnified view of GAMA227264 from the SDSS DR14 Finding Chart Tool, showing the source of the additional trace to be a blue light source in the slit.

7.1.8 GAMA227266

The LOSVD profile from apertures with scattered light removed displays a reducing LOSVD with increasing distance from the spatial centre, typical for ETGs, however the LOSVD profile from apertures which have not had scattered light removed shows an increasing LOSVD with distance from the spatial centre. This confirms the assertion of Katkov *et al.* (2019) that light is scattered from the spatial centre in sufficient quantities to bias measurement of LOSVD. The shape of the LOSVD profile was confirmed using kinematic results extracted at S/N ratio = 20 across 11 spatial bins. An image of GAMA227266 is presented in Figure 7-8.

Analysis of the central $R_e/8$ aperture indicated an old stellar population with an average age of 1.24×10^{10} yr and metallicity of 0.297, and the pPXF plot in Figure 6-6 shows a single old stellar population. The lower panels in the GAMA227266 spatial profiles, shown in Figure 6-7, confirm an old, uniform stellar population in the sampled area with no spatial trends, together with a profile of reducing metallicity with increasing radius as reported for ETGs in the SAURON and ATLAS^{3D} surveys (Kuntschner *et al.*, 2010; Kuntschner, 2014). The central metallicity value of 0.297 appears moderately high for an ETG with an old stellar population when compared to results from SAURON presented in Figure 6-6. The upper panels for GAMA227266 in Figure 6-6 show the V and LOSVD profiles derived from kinematics and populations fittings match within their uncertainties, which provides additional assurance of the profile shapes.

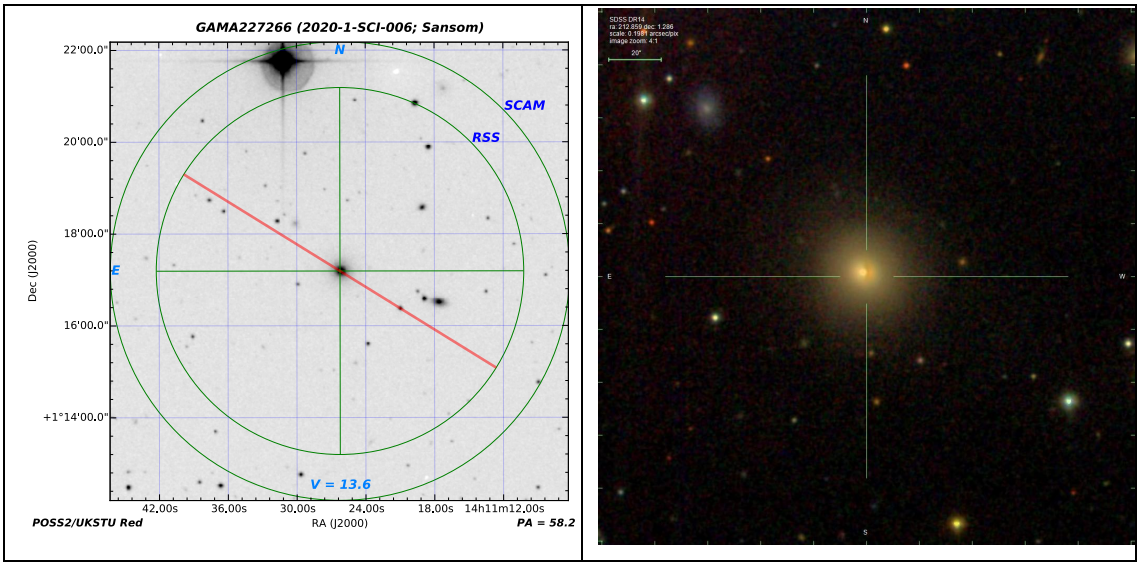

Figure 7-8: Layout is as Figure 7-2. The right panel is a magnified view of GAMA227266 from the SDSS DR14 Finding Chart Tool.

7.1.9 GAMA272990

GAMA272990 is an Elliptical galaxy with an unusually high molecular hydrogen content (Sansom et al., 2019) and high levels of dust. An image of GAMA272990 is presented in Figure 7-9. The spectrum displays absorption features typical of an ETG. The Balmer absorption lines are strong and there is a prominent 4000Å break, suggesting that this galaxy is dominated by an intermediate age stellar population.

The velocity profile shows a symmetric increase in rotational velocity with increasing distance from the spatial centre. The LOSVD profile appears asymmetric around the centre line of the trace and unexpectedly shows LOSVD increasing with distance from the spatial centre, suggesting a sub-structure in the stellar kinematics. Previous work (Sansom *et al.*, 2019) has reported undisturbed kinematics in the ISM molecular gas. The central $R_e/8$ aperture has a stellar population with average age of $\sim5.1\times10^9$ yr and

metallicity of 0.029. The pPXF plot in Figure 6-6 shows the possible presence of three individual intermediate to old stellar population components with ages between 1×10^9 and $\sim1.1\times10^{10}$ yr and metallicities between ~0.2 and ~-0.5. The unexpected LOSVD profile and multiple stellar population components may provide clues to the origin of the high ISM dust and gas content, e.g. minor mergers. This could be further investigated by reanalysing the current data, e.g. using the STARLIGHT package to investigate star formation history. Acquisition of additional longslit spectra would improve the S/N ratio and extend the spatial extent of the sample to enable analysis of stellar kinematic and population profiles out to R_e. Alternatively, given its relatively low ellipticity of 0.254, an integral field study could provide two-dimensional data on stellar kinematics and populations of this target.

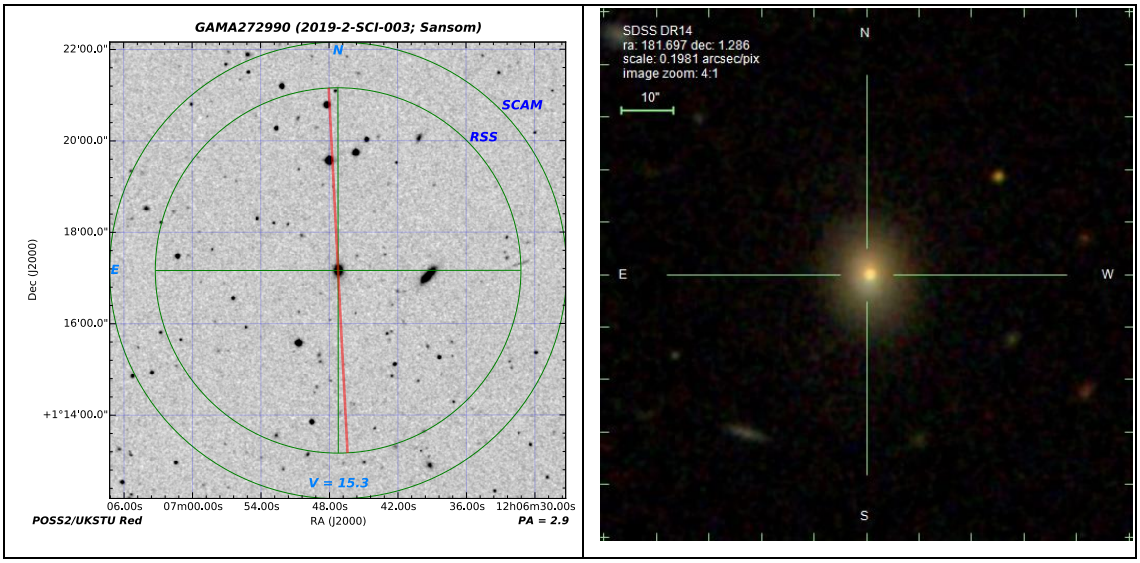

Figure 7-9: Layout is as Figure 7-2. The right panel is a magnified view of GAMA272990 from the SDSS DR14 Finding Chart Tool.

7.1.10 GAMA298980

GAMA298980 has the lowest stellar mass in the sample at $\sim7\times10^9$ $M_\odot$ and has been classified as an Elliptical galaxy, however its spectrum shows strong emission lines of [OIII], [OII], [NII], Hα and Hβ, and the 4000Å break is difficult to detect. The emission features suggest relatively recent star formation. An image of GAMA298980 is presented in Figure 7-10. The central $R_e/8$ aperture has a stellar population with an average age of 7.9×10^9 yr and metallicity of -0.373. This places GAMA298980 closer to the star forming population on the mass vs. metallicity plot shown in Figure 6-5. The pPXF plot in Figure 6-6 shows the possible presence of three individual stellar population components, the major component is old at $\sim1\times10^{10}$ yr and the secondary component is intermediate age at $\sim1\times10^9$ yr. The third component shows as a trace young population at $\sim0.03\times10^9$

yr, reinforcing the suggestion of a recent burst of star formation. This complex star formation history in a galaxy morphologically classified as Elliptical and the particularly low metallicity of -0.373 require further investigation, ideally using higher S/N ratio longslit spectra to improve sampling in the central regions and to extend the area sampled.

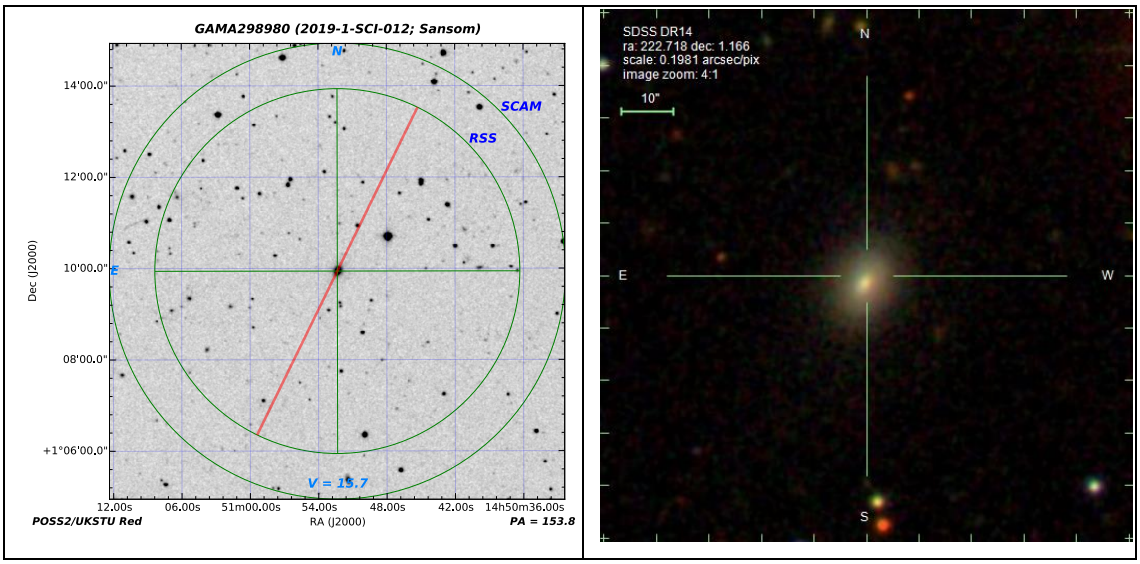

Figure 7-10: Layout is as Figure 7-2. The right panel is a magnified view of GAMA298980 from the SDSS DR14 Finding Chart Tool.

7.1.11 GAMA422436

Examination of the 2D spectrum revealed a second faint extended trace centred on spatial pixel 165. Figure 7-11 shows the presence of an additional, blue light source superimposed on the galaxy disc, in line with the major axis but beyond the area sampled for analysis of stellar kinematics and populations.

The LOSVD profile appears relatively symmetric around the centre line of the trace and shows reducing LOSVD with increasing distance from the spatial centre, typical of ETGs. The central $R_e/8$ aperture has a single old stellar population with an average age of 1.29×10^{10} yr and metallicity of 0.238. Spatial profiles, shown in Figure 6-7, confirm an old, uniform stellar population in the sampled area with no spatial trends and reducing metallicity with increasing radius.

7.1.12 GAMA546040

The LOSVD profile is relatively symmetric around the centre line but has an unexpected dip at ~+2 arcsec, see Figure 6-7. No additional light sources are visible in this area, however in the image in Figure 7-12 GAMA546040 is saturated at ~+2 arcsec. No differences have been identified in the 1D spectrum from that aperture, therefore no root cause can be identified. As the dip is within the uncertainties and affects one aperture it is not interpreted as evidence of a kinematic sub-structure.

The image in Figure 7-12 shows the presence of an additional light source ~10 arcsec from the centre of the galaxy. This light source is close to but not in the slit and no additional trace is seen on the 2D science spectrum.

The central $R_e/8$ aperture has an old stellar population with an average age of 1.29×10^{10} yr and metallicity of 0.246, shown in the pPXF plot in Figure 6-6. Spatial profiles, shown in Figure 6-7, confirm an old, uniform stellar population in the sampled area with no spatial trends, and reducing metallicity with increasing radius.

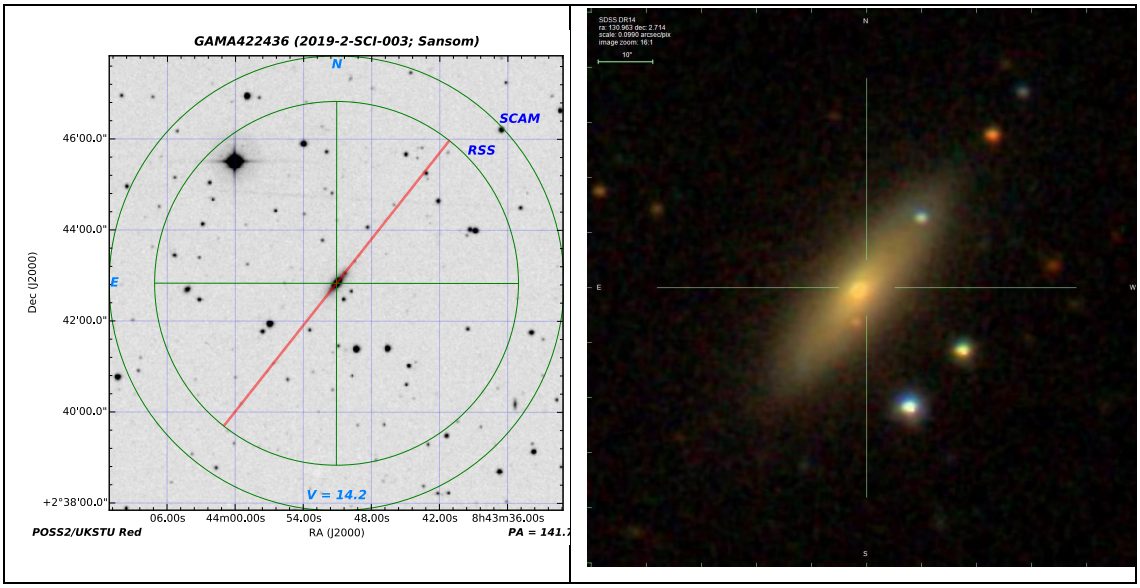

Figure 7-11: Layout is as Figure 7-2. The right panel is a magnified view of GAMA422436, from the SDSS DR14 Finding Chart Tool, showing the source of the additional trace to be a blue light source in the slit.

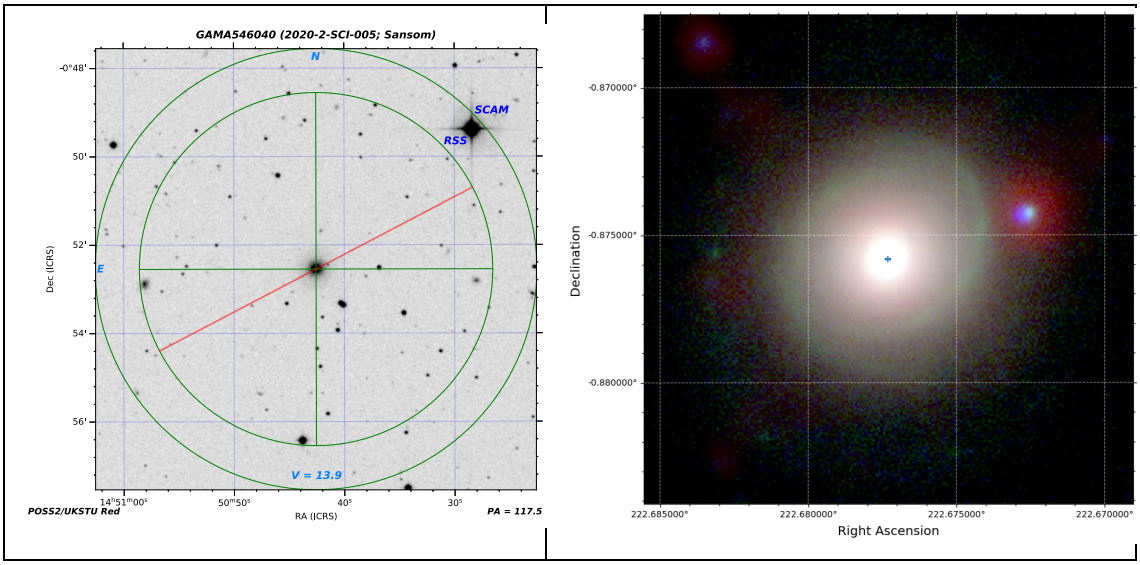

Figure 7-12: Layout is as Figure 7-2. The right panel is a composite RGB image of GAMA546040 (https://datacentral.org.au/services/cutout/). The image size is 30 arcsec on the x and y axes. RGB colour bands used are, red – WISE W1, green – VST g, blue – SDSS i.

7.1.13 GAMA560238

Examination of the 2D spectrum revealed a second trace centred on spatial pixel 217, with overlap between this trace and the trace of GAMA560238 at pixel ~209, as shown in Figure 7-13. Figure 7-14 shows the presence of an additional light source. The spectrum from pixel 217 has a redshift of z ~0.0002, indicating that the additional light source is a foreground object. Apertures from pixels >209 were not included in the analysis, and the higher numbered apertures that were included will contain some polluting light.

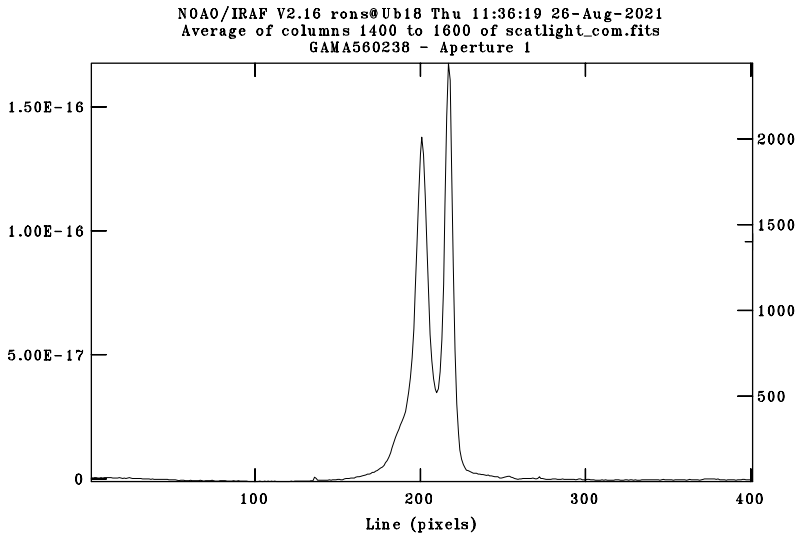

Figure 7-13: Spatial section of columns 1400 – 1600 of the science spectrum of GAMA560238 showing the science trace on the left side and the overlapping trace of the additional light source on the right. The traces intersect at spatial pixel 209.

The right panel of Figure 7-14 shows a ring of bluer colour ~5 arcsec from the centre, suggesting a younger stellar population. The sampled area includes the inner part of this ring. The LOSVD profile is unusual, being relatively flat over the central part of the target and then increasing with radius, however it is possible that the increase on the right side in Figure 6-2, i.e. at higher aperture numbers, is due to light pollution from the additional light source. Analysis of the central $R_e/8$ aperture, which should be relatively unaffected by the ring and polluting light, indicated an old stellar population with an average age of 1.26×10^{10} yr and metallicity of 0.24, and the pPXF plot in Figure 6-6 shows a single old stellar population. The spatial profiles for GAMA560238 shown in Figure 6-7, confirm an old stellar population with no spatial trends, together with a profile of reducing metallicity with increasing radius.

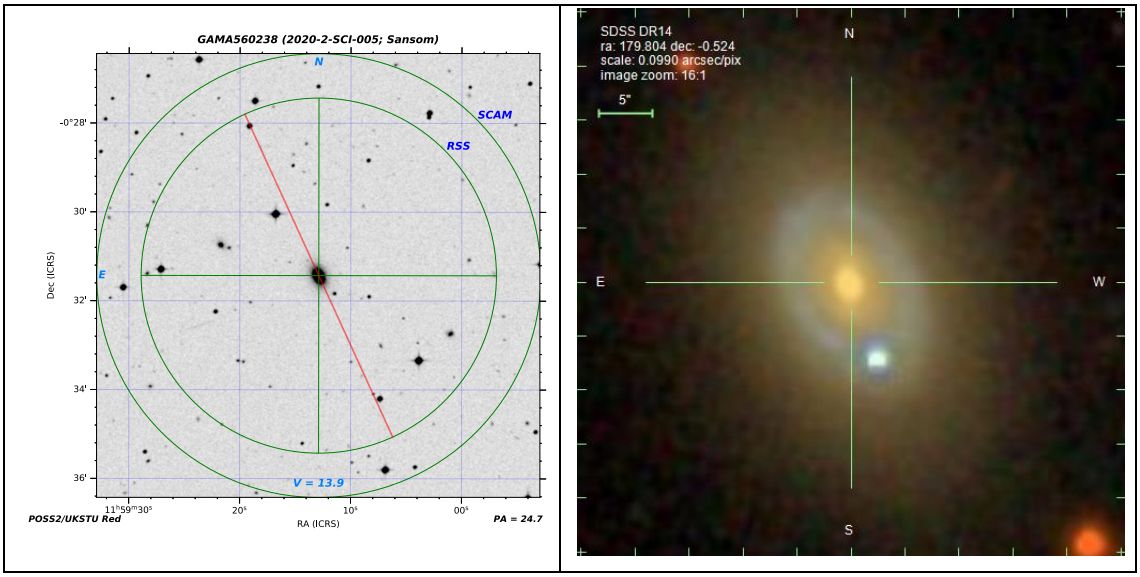

Figure 7-14: Layout is as Figure 7-2. The right panel is a magnified view of GAMA560238 from the SDSS DR14 Finding Chart Tool, showing position of the additional light source superimposed on the outer regions of the target galaxy and in line with the slit. The additional light source is not visible in the left panel as it is within the saturated area of the target galaxy.

7.1.14 GAMA569555

The spectrum shows an unidentified strong emission feature at 6338Å which is an artefact from an incompletely removed CR. Examination of the 2D spectrum revealed a second trace centred on spatial pixel 130 and Figure 7-15 shows the presence of the additional light source in the slit. This is located outside the area sampled for analysis of stellar kinematics and populations.

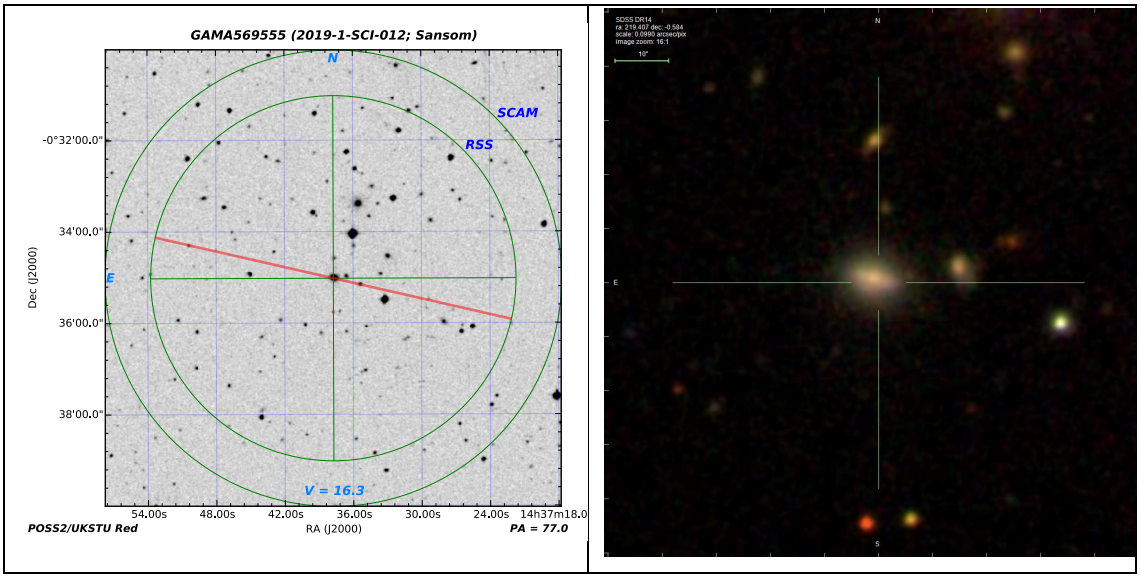

Figure 7-15: Layout is as Figure 7-2. The right panel is a magnified view of GAMA569555, from the SDSS DR14 Finding Chart Tool, showing the source of the additional trace to be a white light source in the slit.

Unexpectedly, for three of the four LOSVD measurements the scattered light removed value is higher than the value from the science spectrum including scattered light. The

SALT Astronomers Log for that night does not record any technical or weather-related issues that could have caused the unusual LOSVD profile shape and accompanying high uncertainty values. The central $R_e/8$ aperture has a stellar population with an average age of 5.69×10^9 yr and very low metallicity of -0.456. The pPXF plot in Figure 6-6 shows the possible presence of three individual stellar population components with ages between $\sim3\times10^8$ and $\sim1\times10^{10}$ yr and metallicities between ~0.2 and <-2, with the major population component being at the very low metallicity value of <-2. It is unlikely that this solution is physically realistic as –

- metallicity changes from high to very low and then back to high, see Figure 6-6
- main component metallicity is unexpectedly low when compared with the ETG population, see Figure 6-5
- LOSVD results have high uncertainties

As strong emission lines in the science spectra indicate a young stellar population component, further investigation of this target is recommended, initially to identify if the low S/N ratio input spectra have caused the anomalous LOSVD and stellar populations results.

7.1.15 GAMA570227

Analysis of the central $R_e/8$ aperture indicated an old stellar population with an average age of 9.2×10^9 yr and metallicity of 0.12. An image of GAMA570227 is presented in Figure 7-16.

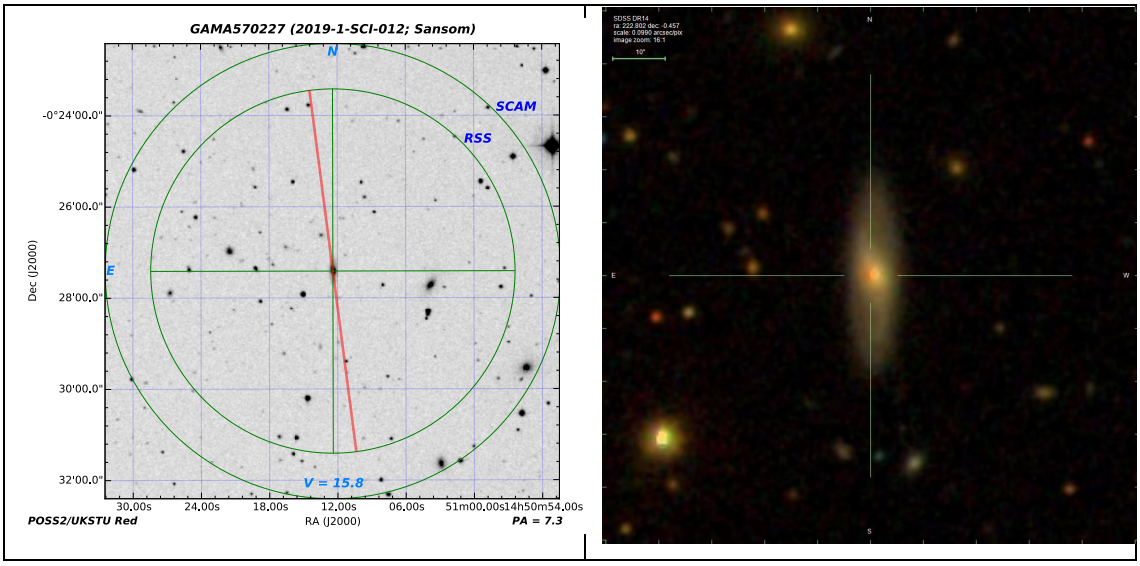

Figure 7-16: Layout is as Figure 7-2. The right panel is a magnified view of GAMA570227 from the SDSS DR14 Finding Chart Tool.

The pPXF plot in Figure 6-6 shows the possible presence of a second, intermediate age, stellar population component with age $\sim1\times10^9$ yr and metallicity ~-0.4. Figure 6-3

shows GAMA570227 to have a low V_{max}/LOSVD for its ellipticity. This is likely due to underestimation of V_{max} from the stellar kinematics plot in Figure 6-2.

7.1.16 GAMA3576053

Kinematic results were extracted at S/N ratio = 20 across 6 spatial bins from pixel 192 to pixel 201, all on the lower side of the spatial centre. The 2D science spectrum does not show any secondary traces and appears spatially symmetric around the centre line across the wavelength range. An image of GAMA3576053 is presented in Figure 7-17 showing the galaxy to be visually symmetric. Manually extracted apertures showed relatively symmetric profiles for V and LOSVD, with LOSVD decreasing and V increasing with distance from the centre. Therefore, data are available from both sides of the centre line of this galaxy and these could contribute to future investigations. The cause of the failure to select bins at pixels >201 is probably within the BINBATCH program.

The central $R_e/8$ aperture has an intermediate age stellar population with an average age of 3.89×10^9 yr and metallicity of 0.269. The pPXF plot in Figure 6-6 shows the main stellar population component with an age of $\sim9.5\times10^9$ yr and a metallicity of ~0.2, and the possible presence of an additional stellar population component with age $\sim1\times10^9$ yr and metallicity ~-0.2.

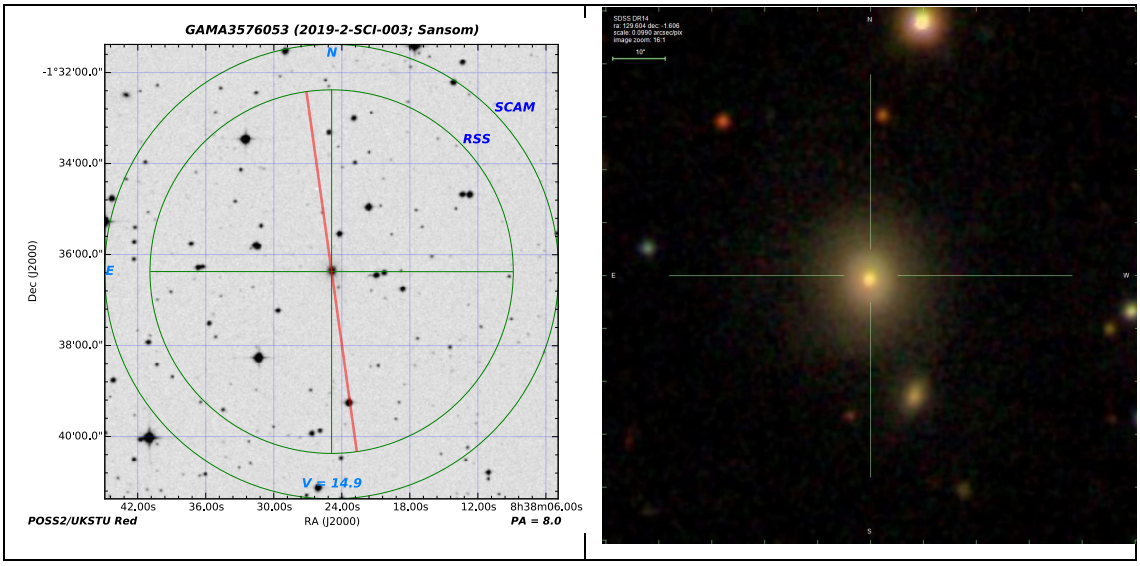

Figure 7-17: Layout is as Figure 7-2. The right panel is a magnified view of GAMA3576053 from the SDSS DR14 Finding Chart Tool.

7.2 Recommendations for Further Work

The lower-than-expected S/N ratio limited the spatial extent of sampling and information that could be reliably extracted by full spectral fitting. As discussed above, the lower-than-expected S/N ratio is most likely due to underestimation of noise by the SALT RSS Simulator and variable weather conditions. Therefore, obtaining additional

observations and including these in the combined science spectra could extended the spatial coverage of the sampling, and allow extraction of additional kinematic and population data. Kinematic and stellar population results from the current spectra do not reveal any features which differentiate the entire sample of dusty ETGs from the general population of ETGs in the SAURON or ATLAS^{3D} surveys. However, analysis was limited to within R_e for kinematics and to a single $R_e/8$ aperture for most populations. An improved S/N ratio would allow –

1. investigation of stellar kinematic profiles at greater distance from the spatial centre and a direct measurement of V_{max}
2. extraction of stellar population profiles for those targets which have young age stellar population components.

Given the overhead in obtaining additional spectra, e.g. time required for flat and arc calibration images, follow up is not recommended for those targets which have intermediate/old stellar populations and profiles which do not suggest the presence of stellar kinematic sub-structures i.e. GAMA79849, 99687, 136847, 227264, 227266, 422436, 546040, 570227 and 3576053.

While GAMA65075 has a very irregular LOSVD profile its single, old stellar population in the central area is typical when compared with SAURON results in Figure 6-4 and it sits close to the Green Valley line on the mass vs. metallicity plot in Figure 6-5. The presence of dust lanes in the central area could explain the irregular LOSVD profile rather than sub-structures in the stellar kinematics.

GAMA560238 has a single old stellar population in the central area, a possible young population in a ring structure and an atypical, irregular LOSVD profile with upturns at its outer edges. While these could indicate kinematic sub-structures the presence of polluting light from the foreground light source seen in Figure 7-14 would make further investigation by longslit spectroscopy difficult.

Follow up is recommended for the following targets –

- GAMA85416 – the asymmetric LOSVD profile suggests the presence of kinematic sub-structures and emission features in the 1D spectra from all apertures suggests a relatively recent star forming episode, contradicting the single old stellar population found by full spectral fitting of the central aperture. Extraction of spatial profiles for stellar age and metallicity to identify the location of the young stellar population components is recommended, using pPXF with both the S/N ratio 20 and 30 apertures. Given the failure of pPXF

to converge on a value of regul, additional analysis of the stellar populations is recommended using an alternative package e.g. STARLIGHT.

- GAMA272990 – shows an inverted LOSVD profile i.e. increasing with radius, and there are three stellar population components ranging from young/intermediate (~0.5×10^9 to ~1×10^9 yr) to old (~14×10^9 yr). The ISM of this galaxy has previously been investigated and contains unusually large amounts of molecular hydrogen. Reanalysis of the existing data using a different software package, additional stellar kinematic and populations analysis at greater radii, or an integral field study, may provide information on the source of the cold gas and dust.
- GAMA298980 – the appearance of a young stellar population component of ~0.03×10^9 yr and a relatively low average population age of 7.9×10^9 yr in the central $R_e/8$ aperture suggest a complex star formation history for a galaxy morphologically classified as Elliptical and without stellar kinematic sub-structures. These results require confirmation given the low metallicity of -0.373, initially with a focus on improving understanding of uncertainties. As for GAMA85416, additional analysis of the stellar populations is recommended using an alternative package. However, this may require higher S/N ratio input spectra as only four apertures could be extracted from the combined SALT science spectrum at S/N = 30, see Table 3-3.
- GAMA569555 – high uncertainties in LOSVD and a reversed response to scattered light removal indicate that the binned spectra with S/N ratio = 20 may have been too noisy for reliable stellar kinematics analysis. While recognising that the current stellar populations solution may be biased by noise, e.g. the extremely low metallicity of the main component, the presence of a young stellar population component suggests some complexity in the star forming history. Given the failure of pPXF to converge on a value of regul a formal analysis of the uncertainties in the pPXF solution should be performed, and additional analysis of the stellar population components in the central aperture is recommended using an alternative package e.g. STARLIGHT.

Further work is also required to improve and refine the processes for data reduction and extraction of results from 1D spectra, specifically –

- Rejection of potentially useful data for GAMA3576053 by BINBATCH requires investigation.

- Many of the scattered light profiles of SALT standard stars from the Katkov *et al.* (2019) process were asymmetrical and therefore were unusable. A symmetrical profile would be expected for scattering of light in the telescope optics and the root cause of the asymmetries was not clear. Robustness of the derived results would be improved with a deeper understanding of the scattered light profiles.
- Failure of $\Delta\chi^2$ to converge to the desired $\Delta\chi^2$ for some targets remains unexplained and is not covered in the literature. Initial investigations should focus on the effects of noise in the input spectra. This could be achieved by a Monte Carlo simulation where noise from a Gaussian distribution is added to each pixel in the spectrum, which is then fitted using pPXF. The output would allow understanding of the effects of noise in the input spectrum.
- A more robust process is required for estimation of uncertainties in the age and metallicity results. For example, the pPXF pp.weights vector contains the mapping of library templates fitted to the input spectrum from which a distribution of ages and metallicities could be extracted. These could be fitted with a Gaussian function to provide an estimate of uncertainties. Alternatively, a Monte Carlo simulation method could be developed to provide a more formal determination of uncertainties in the stellar population parameters.

7.3 Conclusions

7.3.1 Primary Conclusion

Stellar kinematic profiles show undisturbed kinematics and no stellar kinematic sub-structures, see Section 1.2.1, in 10 of the 15 targets and analysis of stellar populations shows young stellar population components in only 4 of the 15 targets. While these young stellar population components point to a possible merger origin for some of the dust in those targets, there is no evidence that mergers contributed to the high dust content in all targets in this sample of dusty ETGs. Therefore, these results suggest that there may also be internal origins for the dust.

7.3.2 Supporting Conclusions

The primary objective of obtaining and reducing SALT longslit optical spectra was achieved, and the spectra show absorption features typical of intermediate/old age stellar populations, with three showing emission features of H and O typical of young stellar population components.

A lower-than-expected S/N ratio limited the spatial extent of S/N ratio based binning to less than R_e. Within the spatial extent that could be sampled GAMA79849, 99687, 136847, 227264, 227266, 298980, 422436, 546040, 570227 and 3576053 have undisturbed stellar kinematics with LOSVD reducing with increasing radius. GAMA65075, 85416, 272990, 560238 and 569555 show some LOSVD irregularities which may indicate stellar kinematic sub-structures. Inspection of visible light images of these targets does not show any foreground/background objects which could explain the kinematic features.

The plot of V_{max}/LOSVD vs. ε in Figure 6-3 shows the target galaxies grouped around the oblate spheroid line, except for GAMA570227 which has a low V_{max}/LOSVD, probably due to underestimation of V_{max}, and GAMA85416 which has the highest V_{max}/LOSVD within the sample. The position of GAMA85416 on the plot is atypical, suggesting possible misclassification of a lenticular as an elliptical.

Stellar kinematics profiles generally show LOSVD measured from spectra with scattered light removed is less than LOSVD from spectra containing scattered light. This confirms the assertion of Katkov *et al.* (2019), that light is scattered by SALT outwards from the spatial centre in sufficient quantities to bias measurement of LOSVD, which can be corrected for, as shown in this thesis.

Results from fitting of stellar populations indicate that the central $R_e/8$ aperture of all target ETGs contain intermediate or old age stellar populations, with mass weighted average population ages $>\sim 4\times10^9$ yr. These results agree with results for ETGs from SAURON, except for GAMA 298980 and 569555 which have unexpectedly low metallicities for their masses, albeit within their somewhat wide uncertainties. From emission lines in their spectra or the pPXF age vs. metallicity grids, young stellar population components appear in GAMA85416, 272990, 298980 and 569555.

$\Delta\chi^2$ did not converge to desired $\Delta\chi^2$ for 11 of the target ETGs, possibly due to lower-than-expected S/N ratios. Profiles for age and metallicity were produced for four targets where $\Delta\chi^2$ did converge to desired $\Delta\chi^2$ i.e. GAMA227266, 422436, 546040 and 560238. These showed a relatively uniform, old stellar population within R_e and metallicity reducing with increasing radius.

Follow up investigation is recommended for GAMA85416, 272990, 298980 and 569555, based on the presence of a young age stellar population component and/or stellar kinematics sub-structures. Initially, this would involve developing a more rigorous process for estimating uncertainties in the age and metallicity results and an investigation

of the cause of non-convergence of $\Delta\chi^2$. If indicated by these investigations, additional spectra could be collected and combined with the existing spectra to improve S/N ratio.

REFERENCES AND BIBLIOGRAPHY

Agius, N. K. et al. (2013) 'GAMA/H-ATLAS: linking the properties of submm detected and undetected early-type galaxies – I. $z \leq 0.06$ sample', MNRAS, 431(2), pp. 1929–1946.

Agius, N.K. et al. (2015) 'H-ATLAS/GAMA and HeViCS – dusty early-type galaxies in different environments', MNRAS, 451(4), pp. 3815–3835.

Anderson, E. and Seaman, R. (1989) 'An Introductory User's Guide to IRAF Scripts'. NOAO. Available at: https://www.sns.ias.edu/sites/default/files/files/cluser.pdf (Accessed: 20 September 2019).

Angthopo, J., Ferreras, I. and Silk, J. (2019) 'Exploring a new definition of the green valley and its implications', MNRAS: Letters, 488(1), pp. L99–L103.

Angthopo, J., Ferreras, I. and Silk, J. (2020) 'A detailed look at the stellar populations in green valley galaxies', MNRAS, 495(3), pp. 2720–2737.

Appenzeller, I. (2013) Introduction to astronomical spectroscopy. Cambridge ; New York: Cambridge University Press (Cambridge observing handbooks for research astronomers, 9). (Accessed 2 August 2020)

Bacon, R. et al. (2001) 'The SAURON project - I. The panoramic integral-field spectrograph', MNRAS, 326(1), pp. 23–35.

Baldry, I. K. et al. (2018) 'Galaxy And Mass Assembly: the G02 field, Herschel–ATLAS target selection and data release 3', MNRAS, 474(3), pp. 3875–3888.

Baldwin, C. et al. (2018) 'Comparison of stellar population model predictions using optical and infrared spectroscopy', MNRAS, 473(4), pp. 4698–4721.

Bassett, R. et al. (2017) 'The SAMI Galaxy Survey: kinematics of dusty early-type galaxies', MNRAS, 470(2), pp. 1991–2006.

Bolte, M. (2006) Signal to Noise in Optical Astronomy, AY257 - Modern Observational Techniques. Available at: http://www.ucolick.org/~bolte/AY257/s_n.pdf (Accessed: 2 August 2020).

Bundy, K. et al. (2014) 'Overview of the SDSS-iv MaNGA Survey: Mapping Nearby Galaxies at Apache Point Observatory', ApJ, 798(1), pp. 7.

Burgh, E. B. and Nordsieck, K. (2009) 'Southern African Large Telescope RSS Observer's Guide'. SALT. Available at: http://www.sal.wisc.edu/PFIS/docs/rss-vis/archive/public/3170AM0007_Observer%27s_Guide.pdf. (Accessed: 20 September 2019).

Cappellari, M. et al. (2011) 'The ATLAS3D project - I. A volume-limited sample of 260 nearby early-type galaxies: science goals and selection criteria: The ATLAS^{3D} project - I. The sample', MNRAS, 413(2), pp. 813–836.

Cappellari, M. (2016) 'Structure and Kinematics of Early-Type Galaxies from Integral Field Spectroscopy', ARA&A, 54(1), pp. 597–665.

Cappellari, M. (2017) ‘Improving the full spectrum fitting method: accurate convolution with Gauss–Hermite functions’, MNRAS, 466(1), pp. 798–811.

Cappellari, M. (2020) ‘The pPXF Package v7.0’. Available at: http://www-astro.physics.ox.ac.uk/~mxc/software/ppxf_manual.pdf. (Accessed: 20 September 2020).

Cappellari, M. and Emsellem, E. (2004) ‘Parametric Recovery of Line-of-Sight Velocity Distributions from Absorption-Line Spectra of Galaxies via Penalized Likelihood’, Publ. Astron. Soc. Pac. 116(816), pp. 138–147.

Chabrier, G. (2003) ‘Galactic Stellar and Substellar Initial Mass Function’, Publ. Astron. Soc. Pac. 115(809), pp. 763–795.

Chilingarian, I. V. and Grishin, K. A. (2020) ‘Estimating Statistical Uncertainties of Internal Kinematics of Galaxies and Star Clusters Derived Using Full Spectrum Fitting’, Publ. Astron. Soc. Pac. 132:064503.

Cid Fernandes, R., Mateus, A., Sodré, L., Stasińska, G., Gomes, J.M. (2005) ‘Semi-empirical analysis of Sloan Digital Sky Survey galaxies – I. Spectral synthesis method’. MNRAS 358(2), pp. 363–378.

Conroy, C. (2013) ‘Modeling the Panchromatic Spectral Energy Distributions of Galaxies’, ARA&A, 51(1), pp. 393–455.

Crawford, S. (2010) ‘PySALT: the SALT science pipeline’, Proc. SPIE. 7737. DOI: 10.1117/12.857000.

Croom, S. M. et al. (2012) ‘The Sydney-AAO Multi-object Integral field spectrograph: The Sydney-AAO Multi-object IFS’, MNRAS, 421(1), pp. 872–893.

Das, A., Pandey, B. and Sarkar, S. (2021) ‘Green valley galaxies in the cosmic web: internal versus environmental quenching’, J. Cosmol. Astropart. Phys. 06:045.

Davies, R. (2011) ‘New views of old galaxies’, Astron. Geophys. 52(5), pp. 5.18–5.24.

Davis, T. A. et al. (2015) ‘Molecular and atomic gas in dust lane early-type galaxies – I. Low star formation efficiencies in minor merger remnants’, MNRAS, 449(4), pp. 3503–3516.

Driver, S. P. et al. (2009) ‘GAMA: towards a physical understanding of galaxy formation’, Astron. Geophys. 50(5) pp. 5.12–5.19.

Driver, S. P. et al. (2011) ‘Galaxy and Mass Assembly (GAMA): survey diagnostics and core data release: GAMA’, MNRAS, 413(2), pp. 971–995.

Eales, S. et al. (2015) ‘H-ATLAS/GAMA: quantifying the morphological evolution of the galaxy population using cosmic calorimetry’, MNRAS, 452(4), pp. 3489–3507.

Eales, S. A. et al. (2018) ‘The causes of the red sequence, the blue cloud, the green valley, and the green mountain’, MNRAS, 481(1), pp. 1183–1194.

Emsellem, E. et al. (2007) ‘The SAURON project - IX. A kinematic classification for early-type galaxies’, MNRAS, 379(2), pp. 401–417.

Emsellem, E. et al. (2011) ‘The ATLAS3D project - III. A census of the stellar angular momentum within the effective radius of early type galaxies: unveiling the distribution of fast and slow rotators’, MNRAS, 414(2), pp. 25.

Falcón-Barroso, J. et al. (2011) ‘An updated MILES stellar library and stellar population models’, A&A, 532, A95.

Farage, C. L. and Pimbblet, K. A. (2005) ‘Evaluation of cosmic ray rejection algorithms on single-shot exposures’, Publ. Astron. Soc. Aust. 22(3), pp. 249–256.

Ferreras, I. (2019) Fundamentals of Galaxy Dynamics, Formation and Evolution. UCL Press. DOI: 10.14324/111.9781911307617.

Galliano, F., Galametz, M. and Jones, A. P. (2018) ‘The Interstellar Dust Properties of Nearby Galaxies’, ARA&A, 56(1), pp. 673–713.

Ge, J. et al. (2018) ‘Recovering stellar population parameters via two full-spectrum fitting algorithms in the absence of model uncertainties’, MNRAS, 478(2), pp. 2633–2649.

Hainline, K. (2015) SALT RSS Long-slit Data Reduction. Available at: http://mips.as.arizona.edu/~khainline/salt_redux.html (Accessed: 19 August 2019).

Hamui, M. et al. (1994) ‘Southern Spectrophotometric Standards. II.’, Publ. Astron. Soc. Pac. 106, pp. 566–569.

HET Overview (2017). Available at: https://hydra.as.utexas.edu/?a=help&h=1 (Accessed: 30 October 2019).

Jian, H.-Y. et al. (2020) ‘Redshift Evolution of Green Valley Galaxies in Different Environments from the Hyper Suprime-Cam Survey’, ApJ, 894(2):125.

Joye, W. and Mandel, E. (2003) ‘New Features of SAOImage DS9’, ASP Conf. Ser. 295, pp. 489–492.

Katkov, I. Y. et al. (2019) ‘The imprint of the thick stellar disc in the mid-plane of three early-type edge-on galaxies in the Fornax cluster’, MNRAS, 483(2), pp. 2413–2423.

Katkov, I. Yu., Kniazev, A. Yu. and Sil’chenko, O. K. (2015) ‘Kinematics and Stellar Populations in Isolated Lenticular Galaxies’, AJ, 150(1):24.

Kaviraj, S. (2008) ‘The star formation histories of early-type galaxies: insights from the rest-frame ultra-violet’, Mod. Phys. Let. A. 23(03), pp. 153–167.

Kelvin, L. S. et al. (2018) ‘Galaxy and Mass Assembly (GAMA): variation in galaxy structure across the green valley’, MNRAS, 477(3), pp. 4116–4130.

Kniazev, A. (2008) ‘SALT Long-slit Data Reduction’. SALT. Available at: http://www.saao.ac.za/~brent/Kniazev_longslit.pdf (Accessed: 21 September 2019).

Kokusho, T. et al. (2017) ‘A star formation study of the ATLAS3D early-type galaxies with the AKARI all-sky survey’, A&A, 605, A74.

Kokusho, T. et al. (2019) ‘Dust properties in the cold and hot gas phases of the ATLAS3D early-type galaxies as revealed by AKARI’, A&A, 622, A87.

Kormendy, J. and Kennicutt Jr, R. C. (2004) 'Secular Evolution and the Formation of Pseudobulges in Disk Galaxies', ARA&A, 42(1), pp. 603–683.

Krajnović, D. et al. (2011) 'The ATLAS3D project - II. Morphologies, kinemetric features and alignment between photometric and kinematic axes of early-type galaxies: Morphologies, kinematics and alignment', MNRAS, 414(4), pp. 2923–2949.

Krajnović, D. et al. (2020) 'Formation channels of slowly rotating early-type galaxies', A&A, 635, A129.

Kuntschner, H. et al. (2010) 'The SAURON project XVII. Stellar population analysis of the absorption line strength maps of 48 early type galaxies', MNRAS, 408, pp. 97–132.

Kuntschner, H. (2014) 'ATLAS^{3D} Stellar Population Gradients', IAU Symp. 311, pp. 53–56. DOI: 10.1017/S1743921315003385

Lacerna, I. et al. (2016) 'Isolated elliptical galaxies in the local Universe', A&A, 588, A79.

Littlefair, S. (no date) University of Sheffield. Astronomical Techniques (PHY217), L14: Signal/Noise. Available at: http://slittlefair.staff.shef.ac.uk/teaching/phy217/lectures/instruments/L14/index.html (Accessed: 31 May 2020).

Martini, P., Dicken, D. and Storchi-Bergmann, T. (2013) 'The Origin of Dust in Early-Type Galaxies and Implications for Accretion onto Supermassive Black Holes', ApJ, 766(2):121.

Michałowski, M. J. et al. (2019) 'The fate of the interstellar medium in early-type galaxies: I. First direct measurement of the timescale of dust removal', A&A, 632, A43.

Osterbrock, D. E. et al. (1996) 'Night-Sky High-Resolution Spectral Atlas of OH and O2 Emission Lines for Echelle Spectrograph Wavelength Calibration', Publ. Astron. Soc. Pac. 108, 277.

Patil, M. K. et al. (2007) 'Properties of dust in early-type galaxies', A&A, 461(1), pp. 103–113.

Peletier, R. (2012) 'Stellar Populations', arXiv:1210.2127 [astro-ph]. Available at: http://arxiv.org/abs/1210.2127 (Accessed: 24 March 2020).

Phillipps, S. et al. (2019) 'Galaxy and Mass Assembly (GAMA): Timescales for galaxies crossing the green valley', MNRAS, 485(4), pp. 5559–5572.

Rizzo, F., Fraternali, F. and Iorio, G. (2018) 'S0 galaxies are faded spirals: clues from their angular momentum content', MNRAS, 476(2), pp. 2137–2167.

Rowlands, K. et al. (2018) 'Galaxy And Mass Assembly (GAMA): The mechanisms for quiescent galaxy formation at z < 1', MNRAS, 473(1), pp. 1168–1185.

Salim, S. (2014) 'Green valley galaxies', Serb. Astron. J. (189), pp. 1–14.

SALT (2017) RSS Simulator — SALT for Astronomers. Available at: https://astronomers.salt.ac.za/software/rss-simulator/ (Accessed: 14 November 2019).

SALT Ast Ops (2020) 'Proposal Information for SALT Call for Proposals: 2021 Semester 1'. Available at: http://pysalt.salt.ac.za/proposal_calls/current/ProposalCall.pdf (Accessed: 2 February 2021).

SALT Science Wiki (2014) Status of Flat Field commissioning. Available at: https://sciencewiki.salt.ac.za/index.php/Status_of_Flat_Field_commissioning (Accessed: 21 October 2019).

Sansom, A. (2019) 'Dust and Molecular Gas in Early-Type Galaxies'. East Asian Observatory, Hilo. Available at: https://www.eaobservatory.org//jcmt/wp-content/uploads/sites/2/2019/05/Dust_MolecularGas_ETGs_EAO_Hilo_May2019_toAlex.pdf (Accessed: 20 February 2020).

Sansom, A. E. et al. (2019) 'ALMA observations of massive molecular gas reservoirs in dusty early-type galaxies', MNRAS, 482(4), pp. 4617–4629.

Sansom, A. E. (2019) 'SALT Phase 1 Observing Time Application'.

Schawinski, K. et al. (2014) 'The green valley is a red herring: Galaxy Zoo reveals two evolutionary pathways towards quenching of star formation in early and late-type galaxies', MNRAS, 440(1), pp. 889–907.

Smith, M. W. L. et al. (2012) 'The Herschel Reference Survey: Dust in Early-Type Galaxies and Across the Hubble Sequence', ApJ, 748(2):123.

Tody, D. (1986) 'The IRAF Data Reduction and Analysis System'. Edited by D. L. Crawford. Available at: https://iraf-community.github.io/doc/iraf.pdf (Accessed: 20 September 2019).

Tody, D. (1993) 'IRAF in the Nineties', ASP Conf. Ser. 52, pp. 173–183.

Trussler, J. et al. (2021) 'The weak imprint of environment on the stellar populations of galaxies', MNRAS, 500(4), pp. 4469–4490.

Vaghmare, K. et al. (2018) 'A SALT Spectral Study of S0s Hosting Pseudobulges', MNRAS, 480(4), pp. 4931–4947.

Vazdekis, A. et al. (1996) 'A new chemo-evolutionary population synthesis model for early-type galaxies. I: Theoretical basis', ApJS, 106(2) p. 307.

Vazdekis, A. et al. (2010) 'Evolutionary stellar population synthesis with MILES - I. The base models and a new line index system', MNRAS, 404(4), pp. 1639–1671.

Vazdekis, A. et al. (2015) 'Evolutionary stellar population synthesis with MILES – II. Scaled-solar and α-enhanced models', MNRAS, 449(2), pp. 1177–1214.

Vudragović, A., Samurović, S. and Jovanović, M. (2016) 'Full stellar kinematical profiles of central parts of nearby galaxies', A&A, 593, A40.

Werle, A. et al. (2020) 'Clues on the history of early-type galaxies from SDSS spectra and GALEX photometry', MNRAS, 497(3), pp. 3251–3263.

Worthey, G. et al. (1994) 'Old Stellar Populations v Absorption Feature Indices for the Complete LICK IDS Sample of Stars', ApJS, 94, p. 687.

Yıldız, M. K. et al. (2020) ‘Cold gas and dust: Hunting spiral-like structures in early-type galaxies’, A&A, 636, A8.

APPENDICES

A. File Naming Convention

MEF FITS data files were delivered by the SALT Pipeline named as follows –

Component	Meaning	Example
Five letters	The SALT standard file header	mbxgp
One letter	P = RSS image, ie spectrum, flat or arc S = SALTICAM image	
Eight numbers	Date in YYYYMMDD format	20190511
Four numbers	Sequential file number	0048
.fits	File name extension	

An example of a SALT file name would be mbxgpP201905110048.fits.

During data reduction all files were renamed using the convention shown below –

Component	Meaning	Example
Leading digits	GAMA Catalogue identifier for the target	GAMA79849
Type identifier	sci = science spectrum arc = arc image flat = flat image img = SALTICAM image	
Three numbers	Sequential file number from the raw files	048
Process identifier	tmp = a temporary or interim working image trm = the image has been trimmed rsp = flat image normalised using IRAF *response* flt = image has been divided by a flat tra = image has been wavelength calibrated bkg = image is background subtracted zap = image had been cosmic ray cleaned ext = corrected for atmospheric extinction xmk = processed without using the crmask gdc = corrected for geometric distortion drd = corrected for galactic extinction flx = image has been flux calibrated scat = scattered light has been removed sig = a sigma image var = a variance image com = a combined image	
File name extension	.fits = a flexible image transport system file .ms = *apall* multispec format	

An example of a file name would be –

GAMA422436_sci_059_trm_flt_tra_bkg_ext_gdc_drd_flx.fits.

B. 1D Spectra Corrected to Rest Wavelength

GAMA65075

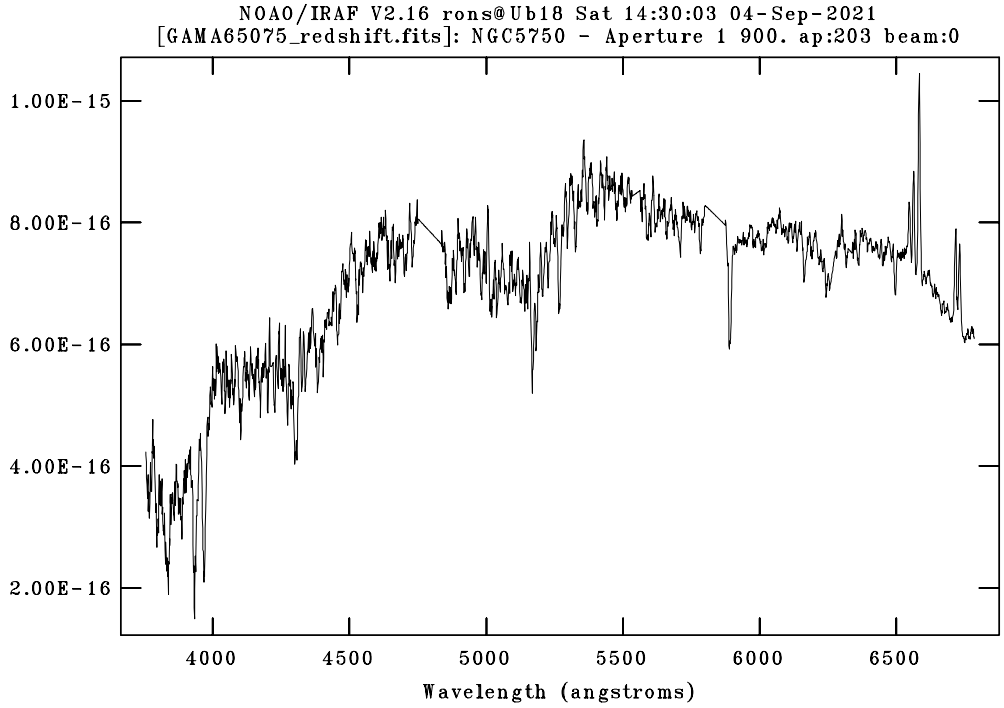

GAMA79849

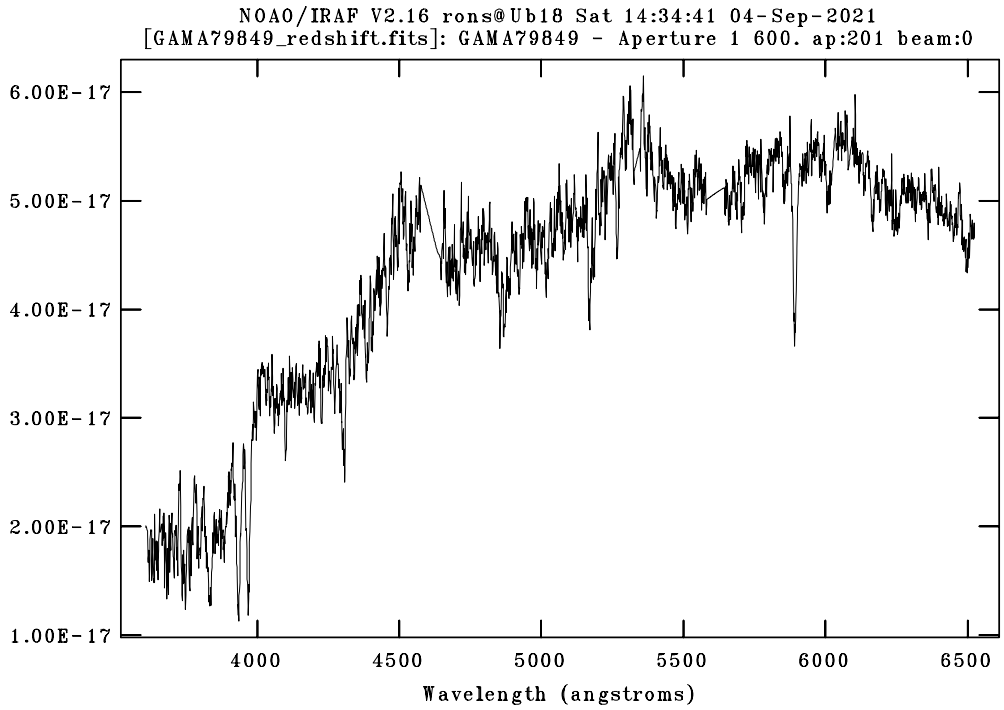

GAMA78425

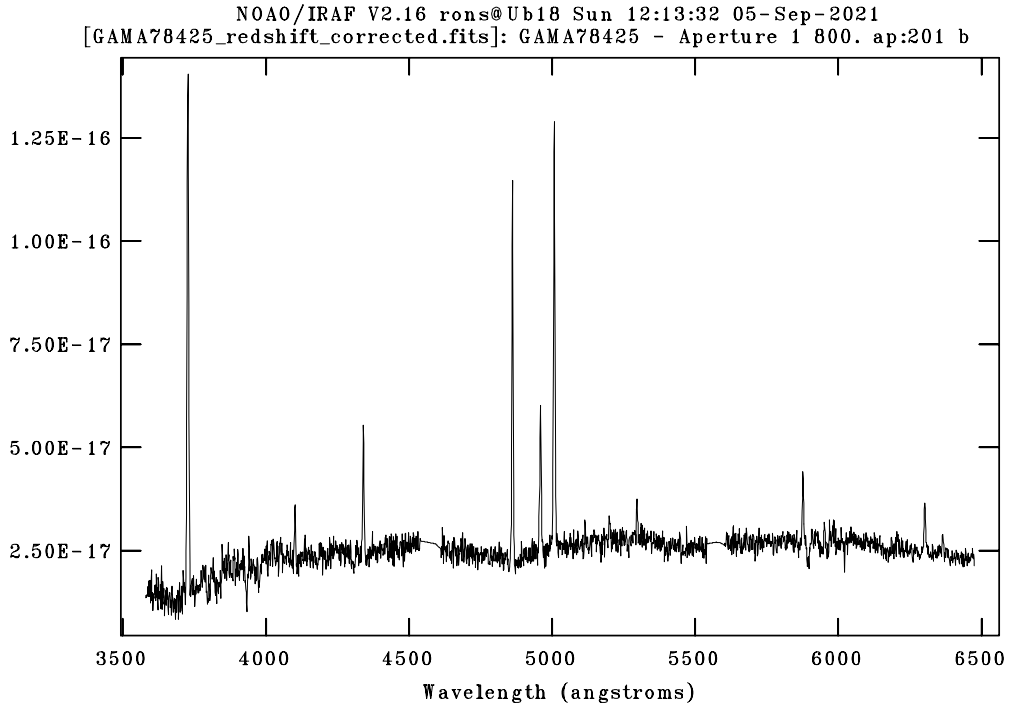
NOAO/IRAF V2.16 rons@Ub18 Sun 12:13:32 05-Sep-2021
[GAMA78425_redshift_corrected.fits]: GAMA78425 - Aperture 1 800. ap:201 b
1.25E-16
1.00E-16
7.50E-17
5.00E-17
2.50E-17
3500
4000
4500
5000
5500
6000
6500
Wavelength (angstroms)

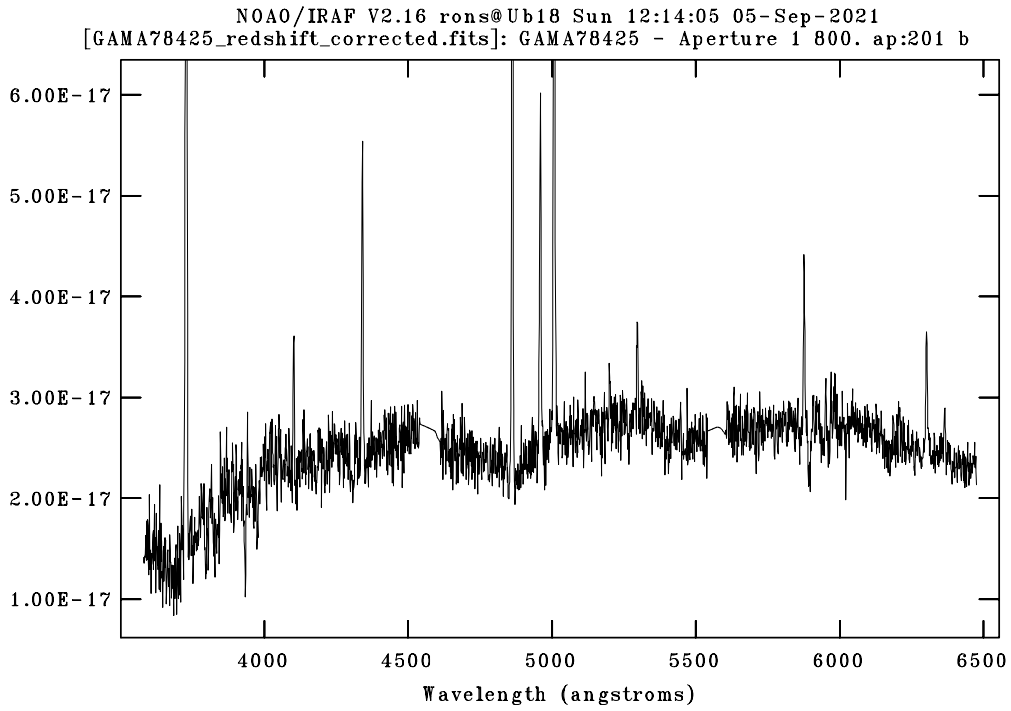
NOAO/IRAF V2.16 rons@Ub18 Sun 12:14:05 05-Sep-2021
[GAMA78425_redshift_corrected.fits]: GAMA78425 - Aperture 1 800. ap:201 b
6.00E-17
5.00E-17
4.00E-17
3.00E-17
2.00E-17
1.00E-17
4000
4500
5000
5500
6000
6500
Wavelength (angstroms)

GAMA85416

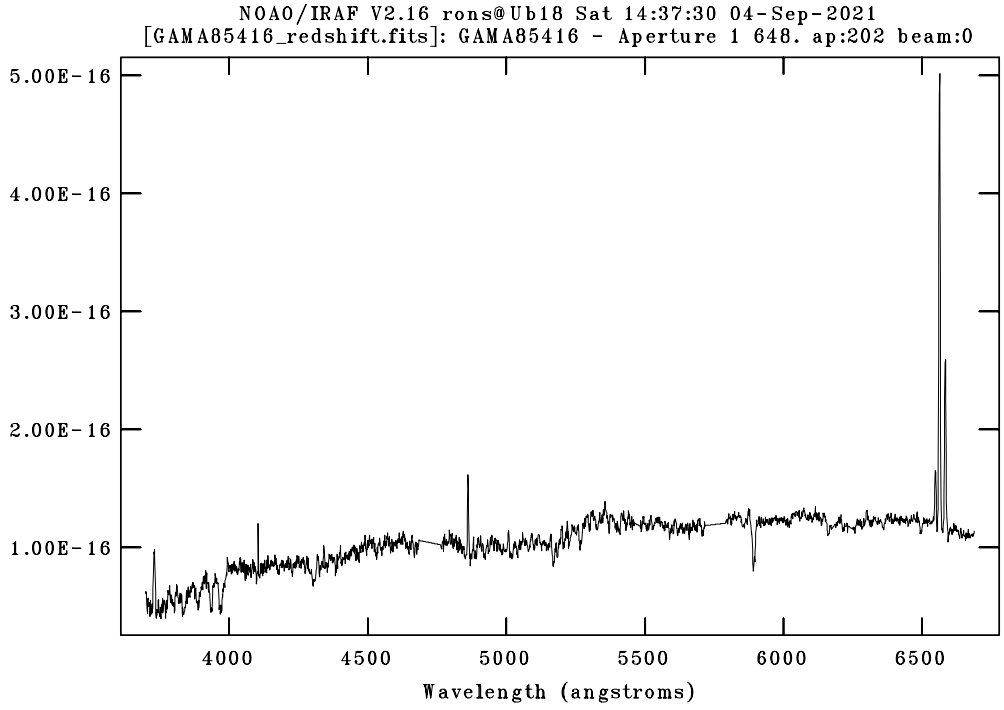
NOAO/IRAF V2.16 rons@Ub18 Sat 14:37:30 04-Sep-2021
[GAMA85416_redshift.fits]: GAMA85416 - Aperture 1 648. ap:202 beam:0
5.00E-16
4.00E-16
3.00E-16
2.00E-16
1.00E-16
4000
4500
5000
5500
6000
6500
Wavelength (angstroms)

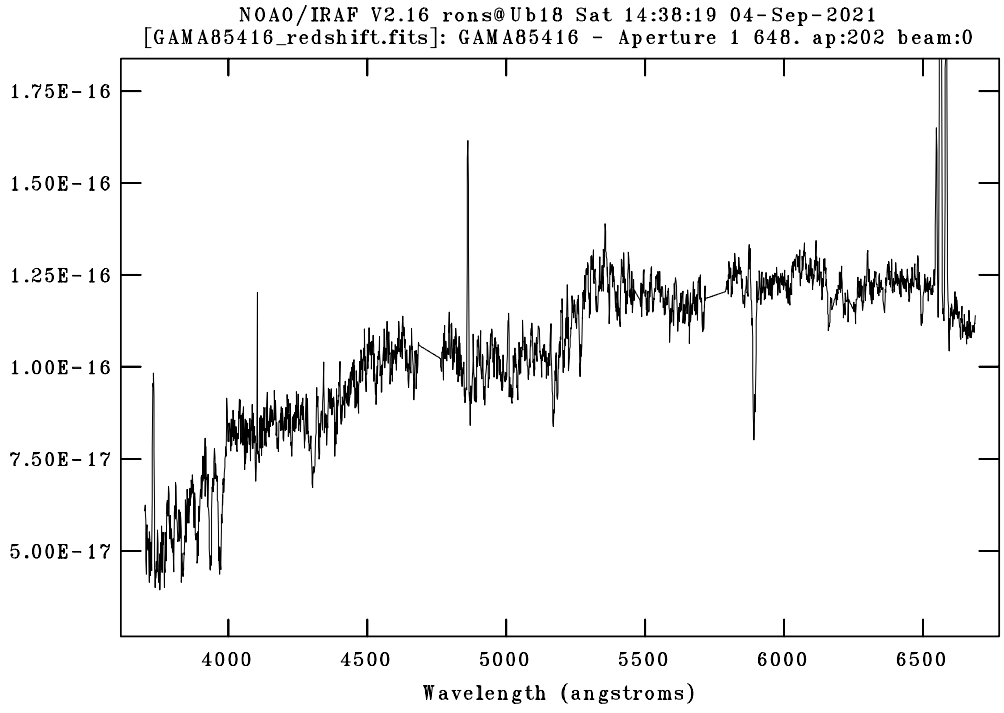
NOAO/IRAF V2.16 rons@Ub18 Sat 14:38:19 04-Sep-2021
[GAMA85416_redshift.fits]: GAMA85416 - Aperture 1 648. ap:202 beam:0
1.75E-16
1.50E-16
1.25E-16
1.00E-16
7.50E-17
5.00E-17
4000
4500
5000
5500
6000
6500
Wavelength (angstroms)

GAMA99687

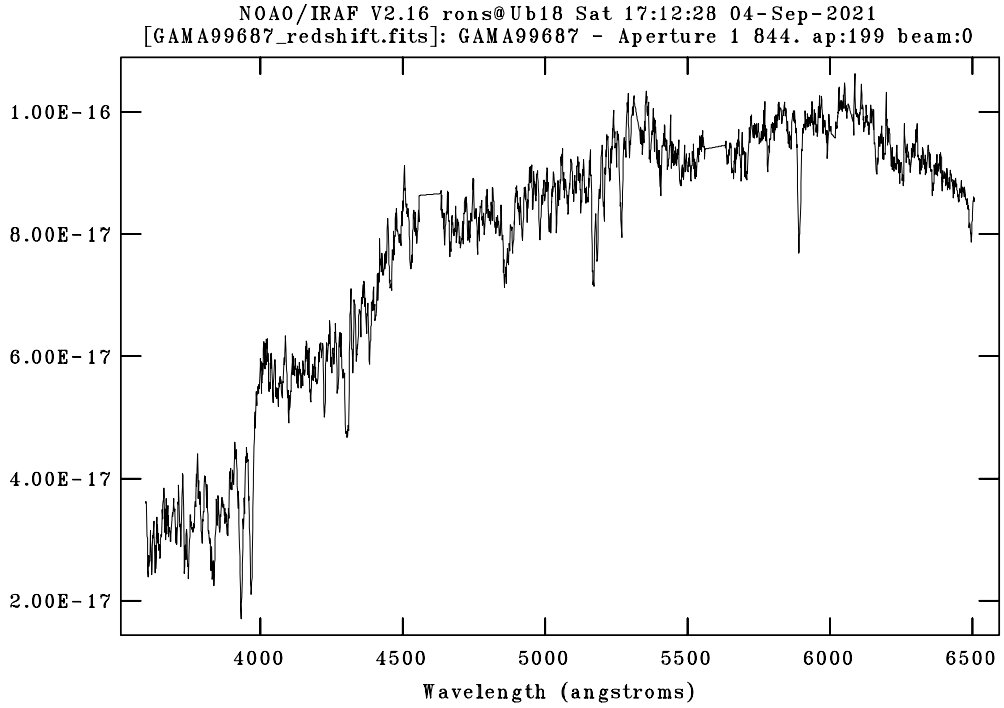

GAMA136847

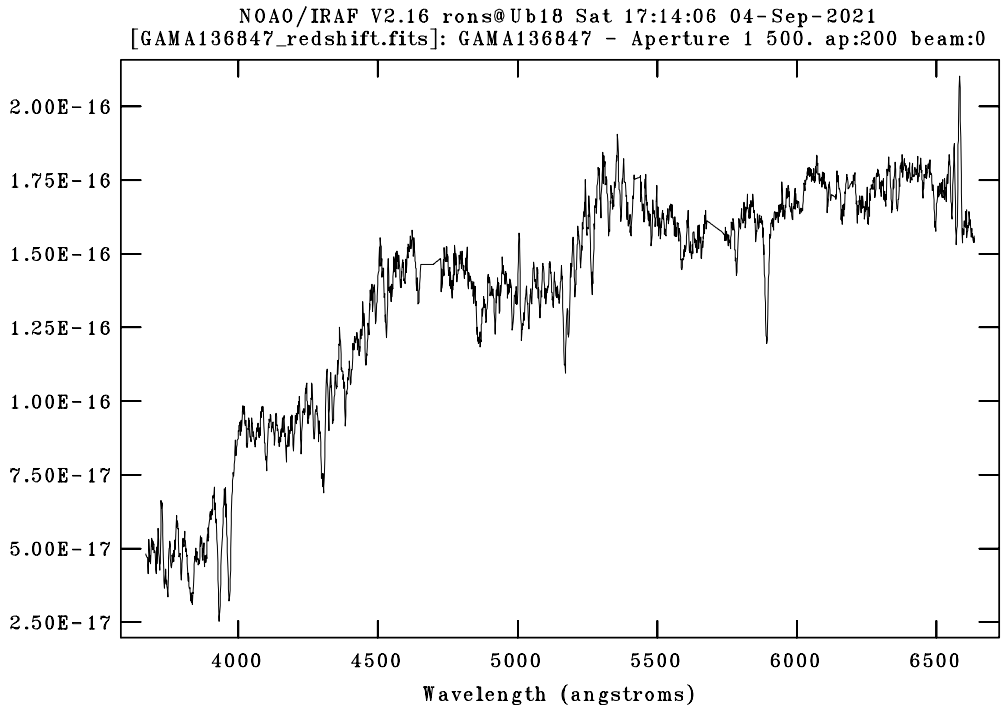

GAMA227264

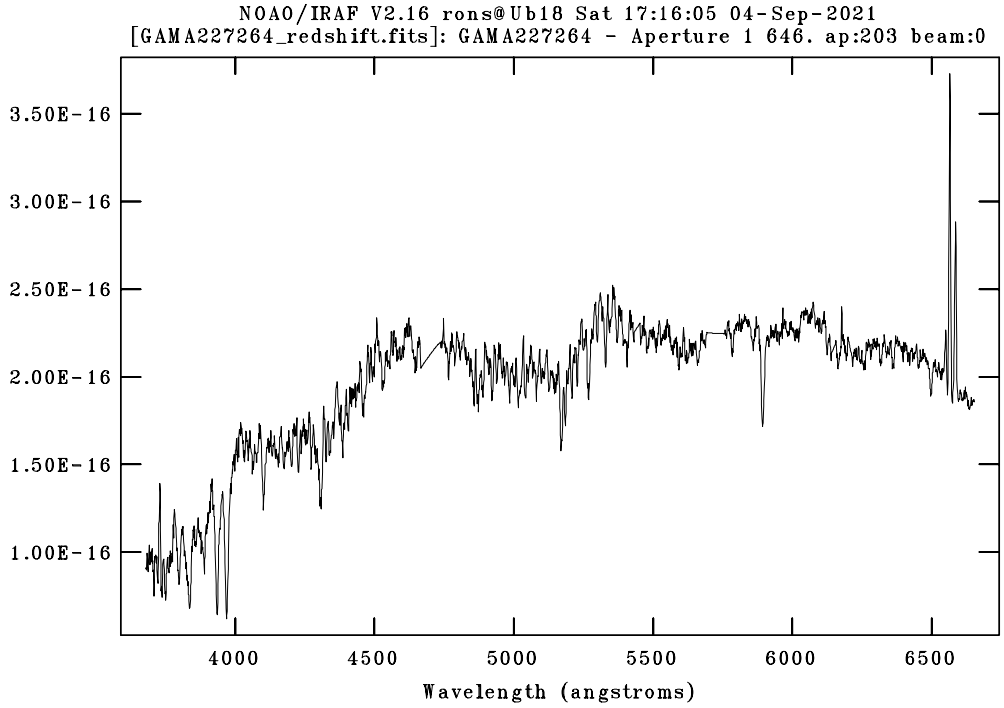

GAMA227266

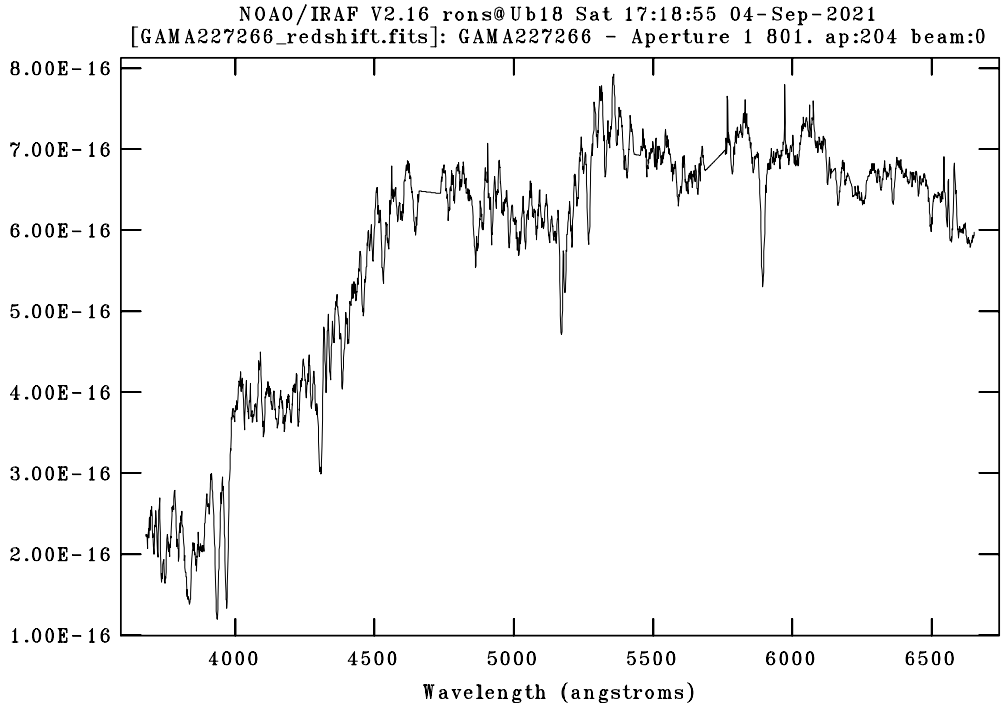

GAMA272990

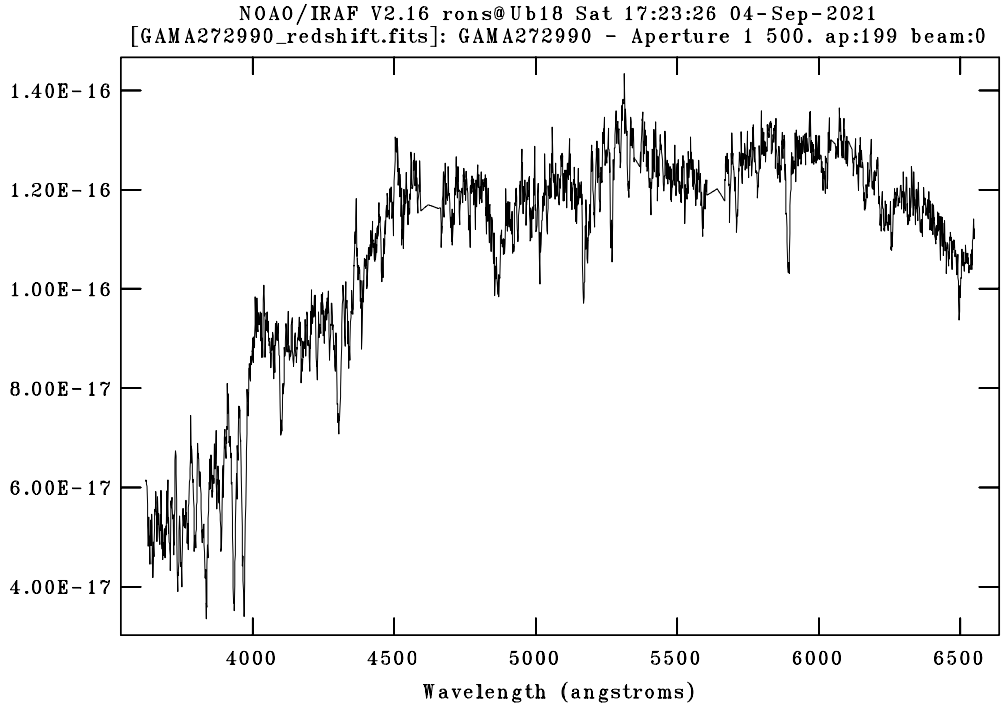

GAMA422436

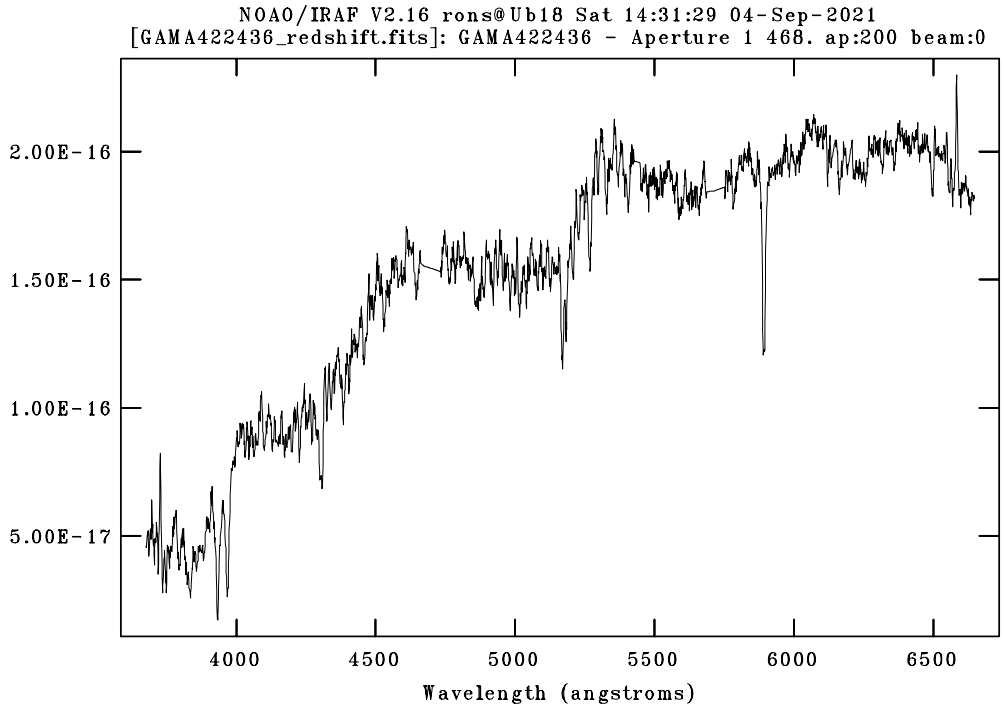

GAMA298980

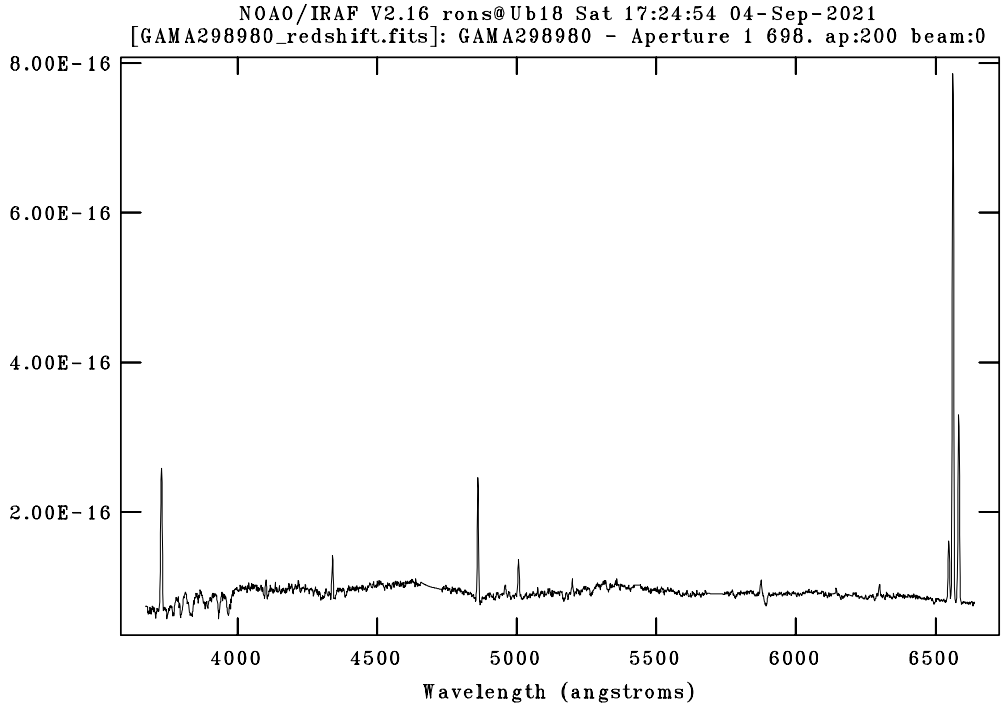
NOAO/IRAF V2.16 rons@Ub18 Sat 17:24:54 04-Sep-2021
[GAMA298980_redshift.fits]: GAMA298980 - Aperture 1 698. ap:200 beam:0
8.00E-16
6.00E-16
4.00E-16
2.00E-16
4000
4500
5000
5500
6000
6500
Wavelength (angstroms)

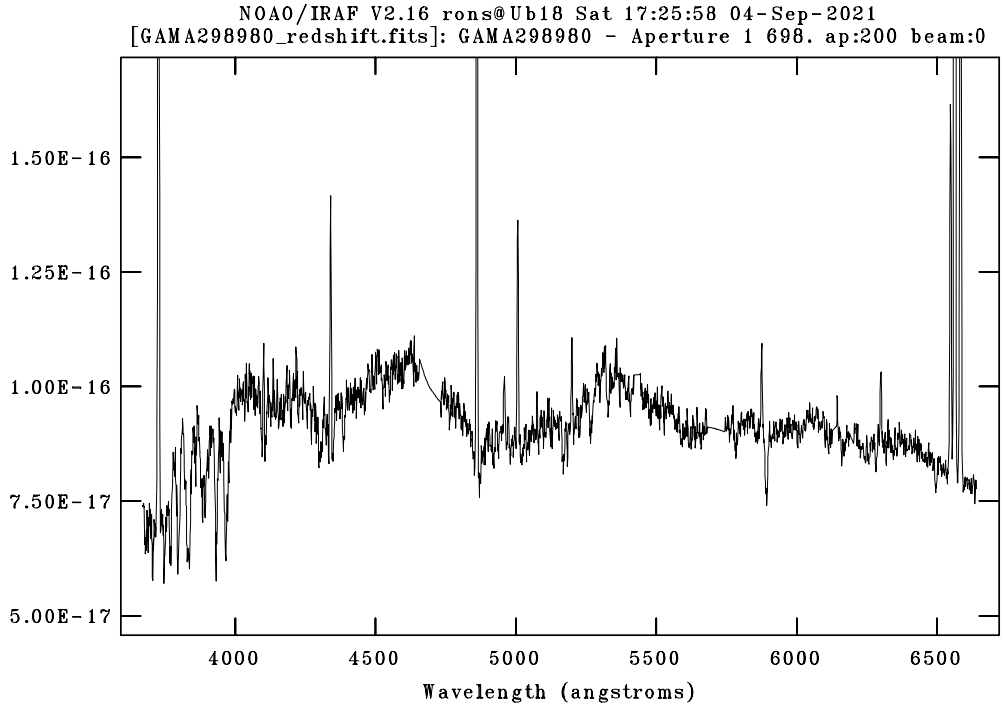
NOAO/IRAF V2.16 rons@Ub18 Sat 17:25:58 04-Sep-2021
[GAMA298980_redshift.fits]: GAMA298980 - Aperture 1 698. ap:200 beam:0
1.50E-16
1.25E-16
1.00E-16
7.50E-17
5.00E-17
4000
4500
5000
5500
6000
6500
Wavelength (angstroms)

GAMA546040

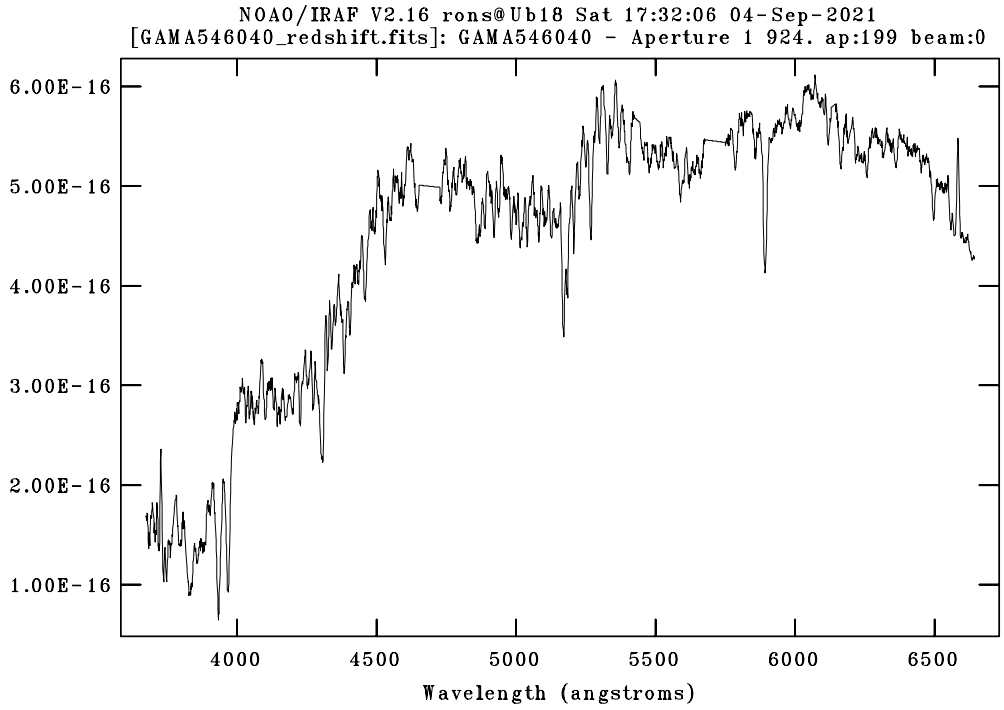

GAMA560238

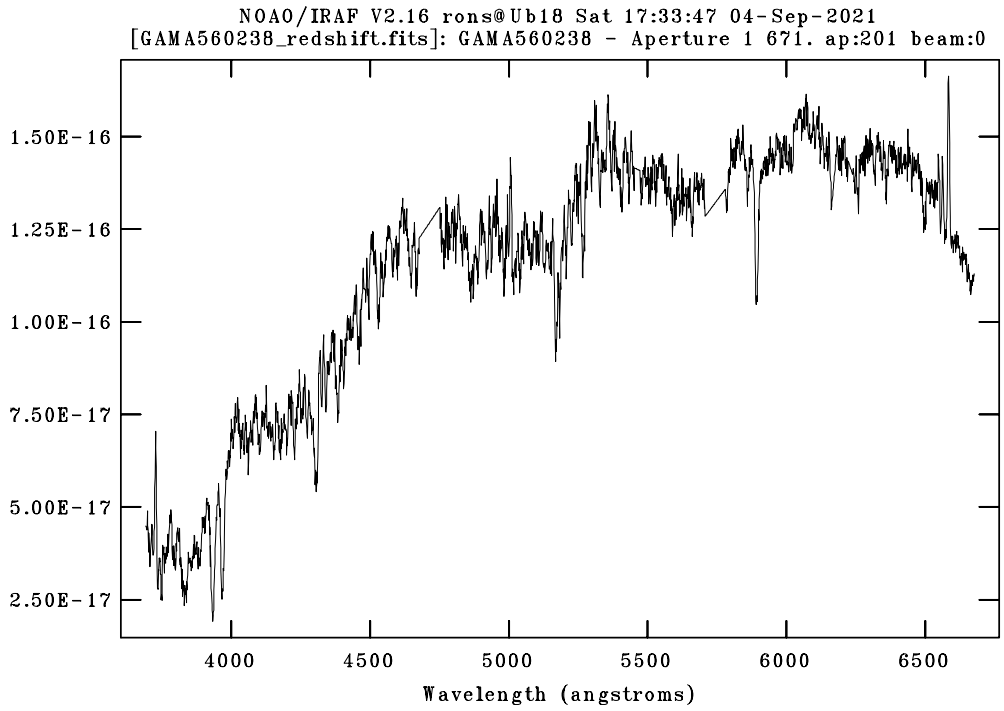

GAMA569555

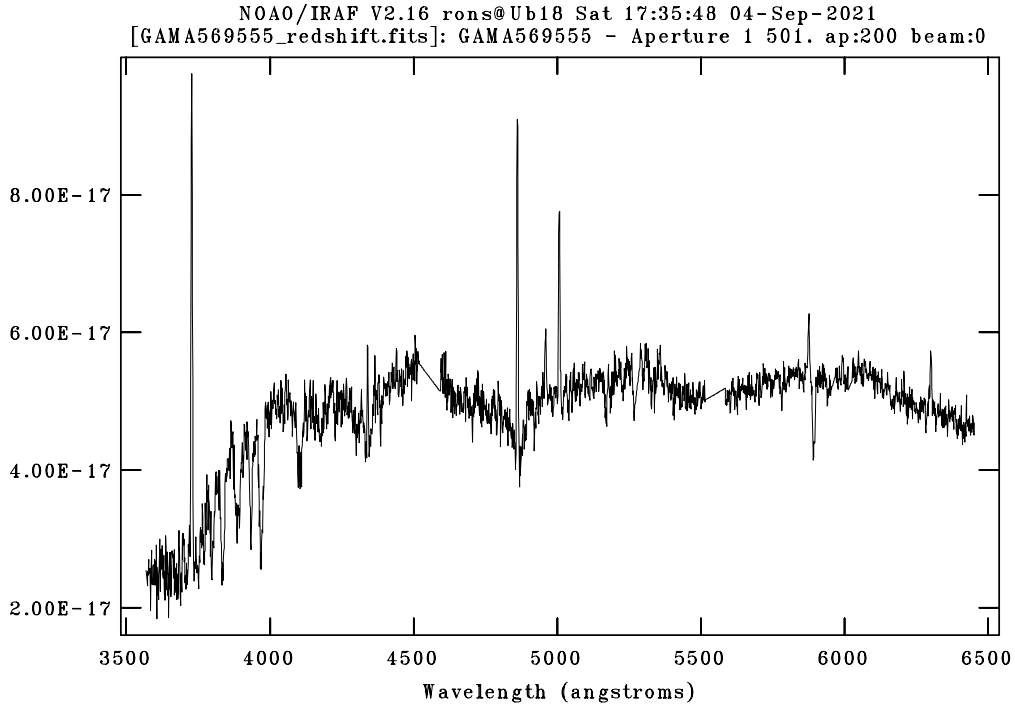
NOAO/IRAF V2.16 rons@Ub18 Sat 17:35:48 04-Sep-2021
[GAMA569555_redshift.fits]: GAMA569555 - Aperture 1 501. ap:200 beam:0
8.00E-17
6.00E-17
4.00E-17
2.00E-17
3500
4000
4500
5000
5500
6000
6500
Wavelength (angstroms)

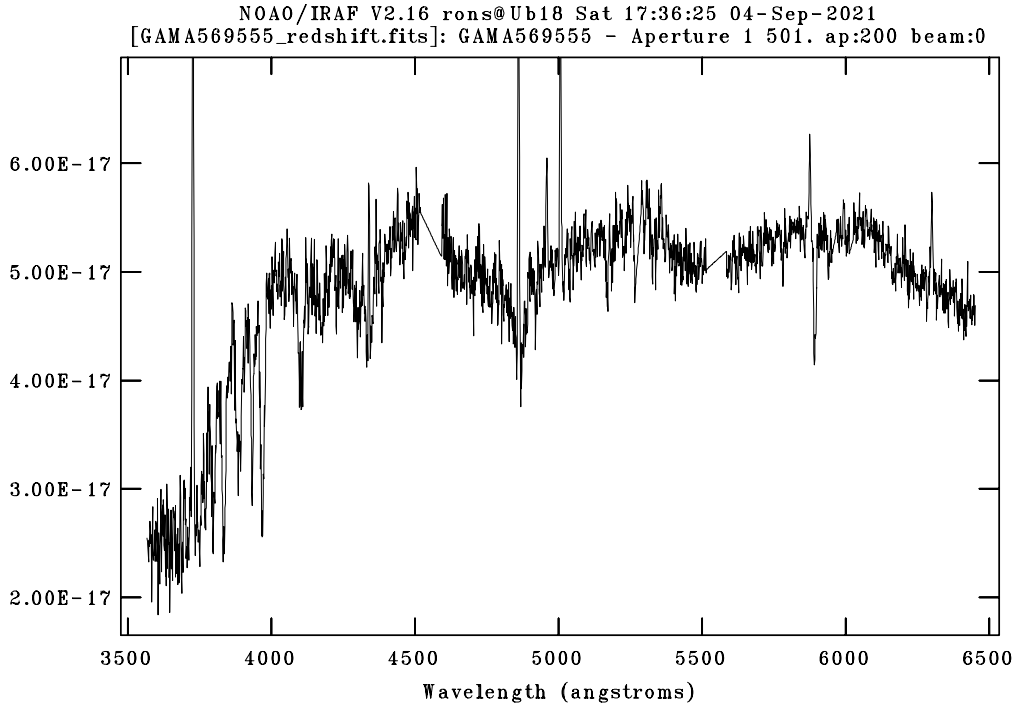
NOAO/IRAF V2.16 rons@Ub18 Sat 17:36:25 04-Sep-2021
[GAMA569555_redshift.fits]: GAMA569555 - Aperture 1 501. ap:200 beam:0
6.00E-17
5.00E-17
4.00E-17
3.00E-17
2.00E-17
3500
4000
4500
5000
5500
6000
6500
Wavelength (angstroms)

GAMA570227

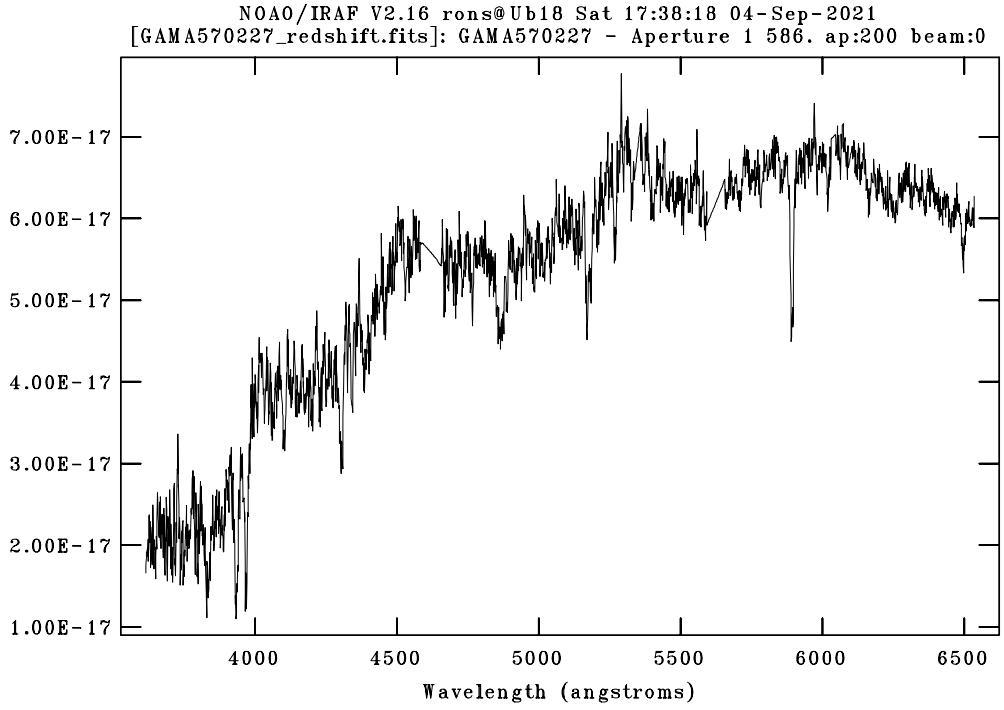

GAMA3576053